

# **Longterm variability of hail-related weather types in an ensemble of regional climate models**

**Langzeitliche Variabilität von hagel-relevanten Großwetterlagen in einem  
Ensemble regionaler Klimamodelle**

Diplomarbeit im Fach Meteorologie  
vorgelegt von

**Marie-Luise Kapsch**

15. März 2011

Referent:

Prof. Dr. Christoph Kottmeier

Korreferent:

Prof. Dr. Klaus Dieter Beheng



**INSTITUT FÜR METEOROLOGIE UND KLIMAFORSCHUNG  
KARLSRUHER INSTITUT FÜR TECHNOLOGIE**



## Zusammenfassung

Gewitterstürme zählen in Deutschland zu denjenigen Wetterereignissen mit einem erheblichen Schadenspotential. Besonders im Sommerhalbjahr können sich Gewitter zu großen Komplexen ausbilden, die von starkem Regen, Windböen, Tornados oder Hagel begleitet werden. Gewitter und deren Begleiterscheinungen ereignen sich mehrmals pro Jahr in Deutschland und verursachen Schäden an Autos, Gebäuden und anderen Besitztümern. In Baden-Württemberg können fast 40% aller witterungsbedingter Schäden an Gebäuden auf Hagel zurückgeführt werden (Puskeiler, 2009).

In den vergangenen Jahren konnte die SV Sparkassenversicherung AG eine Zunahme der Tage beobachten, an denen Hagelschäden auftraten. Eine solche Zunahme führt zu Problemen besonders für Versicherungen, das Baugewerbe und die Landwirtschaft. Laut des vierten Sachstandsberichtes des „Intergovernmental Panel on Climate Change“ (IPCC; IPCC, 2007) konnte im letzten Jahrhundert (1906-2005) auch eine Zunahme der globalen Mitteltemperatur um ca.  $0,74^{\circ}\text{C}$  ( $\pm 0,18^{\circ}\text{C}$ ) beobachtet werden. Dies wirft die Fragen auf, ob die Änderung der Temperatur mit den Änderungen der Häufigkeit von Hagelereignissen zusammenhängt und welche zukünftigen Entwicklungen zu erwarten sind.

Problematisch ist allerdings, dass Gewitter nur lokal begrenzt auftreten. Die typische horizontale Ausdehnung liegt häufig bei weniger als einigen Kilometern. Daher können Gewitter von meteorologischen Bodenstationen oft nicht erfasst werden. Auch Fernerkundungsmessgeräte, wie z. B. das Radar, sind noch nicht in der Lage Hagel zu registrieren, da bisher kein eindeutiger Zusammenhang zwischen Radarreflektivität und Hagel bzw. Regen gefunden werden konnte (Kunz and Puskeiler, 2010; Sauvageot, 1992). Zudem können Gewitter von Klimamodellen nicht abgebildet werden, da deren horizontale Auflösung meist geringer ist als die räumliche Ausdehnung der Gewitterzellen. Aufgrund der Problematik bei der Erfassung von Gewitterstürmen stehen daher keine ausreichend lange Zeitreihen zur Verfügung um mögliche Änderungen der Hageltage über einen langen Zeitraum zu untersuchen.

Um dieses Problem zu umgehen werden im Folgenden für die Auslösung von hochreichender Konvektion wichtige Parameter untersucht. Die Prozesse der Auslösung sind zum einen gut verstanden und zum anderen besser messbar. Parameter die die Auslösung beschreiben sind die thermische Schichtung der Atmosphäre, der Feuchtegehalt und die großräumige Hebung. Es wird angenommen, dass Änderungen dieser Parameter die Wahrscheinlichkeit, mit der Gewitter auftreten, beeinflussen. Unter Verwendung dieser Parameter lassen sich Großwetterlagen definieren, welche dann zu einer gewissen Wahrscheinlichkeit auch Informationen über das Hagelpotential liefern.

Arbeiten von Bissolli et al. (2007) haben gezeigt, dass Wetterlagen basierend auf den genannten Parametern in engem Zusammenhang mit dem Auftreten von Tornados in Deutschland stehen. Ähnliche Ergebnisse erzielten Bardossy and Filiz (2005) in Bezug auf Hochwasserereignisse und Ehmann (2009) bezüglich Hagelschäden. Diese Untersuchungen bilden die Grundlage dieser Diplomarbeit.

In der vorliegenden Arbeit wird die langzeitliche Variabilität der Wetterlagen analysiert, die häufig mit Hagelschäden in Verbindung stehen (hagelrelevant) und solcher die nur selten zusammen mit Hagel auftreten (hagelirrelevant). Um langzeitliche Trends und mögliche Periodizitäten zu detektieren, werden Daten verschiedener Klimamodelle verwendet. Der Fokus bei der Analyse liegt auf der Klärung zwei wichtiger Punkte: Zum einen muss die verwendete Methode der Wetterlagenklassifikation (oWLK) des Deutschen Wetterdienstes (DWD) auf ihre Anwendbarkeit auf unterschiedliche Modelldaten untersucht werden. Zum anderen muss sichergestellt werden, dass Klimamodelle in der Lage sind die Wetterlagen hinreichend gut wieder zu geben.

Zur Klärung stehen Reanalysedaten des ECMWF (ERA40 und ERA-Interim) sowie Daten des regionalen Klimamodells CCLM-ERA40 für den Kontrollzeitraum C20 (1971 bis 2000) zur Verfügung. Die CCLM-ERA40-Daten werden angetrieben von ERA40-Reanalysen, die als Anfangs- und Randbedingungen genutzt wurden. Für denselben Zeitraum sowie verschiedene Projektionszeiträume (2001-2048/2050 bzw. 2011-2050) liegen außerdem Daten acht verschiedener Realisationen des regionalen Klimamodells COSMO-CLM vor. Diese unterscheiden sich in der Version des Regionalmodells COSMO-CLM (3.1 und 4.8), den antreibenden Globalmodellen (ECHAM5-MPI/OM, CCCma3), den Anfangsbedingungen- und -zeiten der Globalmodelle (Lauf 1 bis 3) sowie den Emissionsszenarien (A1B und B1). Auf alle Daten wird die oWLK für das Untersuchungsgebiet Deutschland (ca. 4°E bis 16°E und 45°N bis 57°N) angewendet und die Wetterlagen bestimmt. Die oWLK berücksichtigt die drei Parameter Advektionsrichtung (Windindex) als indirektes Maß für die thermische Stabilität, Zyklonalität in zwei Höhenschichten (1000 hPa und 500 hPa) als Index für großräumige Hebung und Feuchte (niederschlagsfähiges Wasser).

Mittels Hagelschadensdaten der SV und kategorischer Verifikation werden anschließend Wetterlagen mit Hagelereignissen verknüpft. Damit kann zwischen Lagen hagelrelevanten und hagelirrelevanten Lagen unterschieden werden. Diese bilden die Grundlage für die Variabilitätsanalyse.

Die Anwendbarkeit der Methode wird durch einen Vergleich der absoluten Anzahl der einzelnen Wetterlagen aus ERA40, ERA-Interim und CLM-ERA40 für den Kontrollzeitraum C20 überprüft. Geringe Abweichungen zwischen den absoluten Anzahlen implizieren, dass die oWLK auf verschiedene Reanalysedaten anwendbar ist und dass eine unterschiedliche Modellauflösung von ERA40 ( $\approx 125$  km), ERA-Interim ( $\approx 80$  km) und CCLM-ERA40 ( $\approx 50$  km) nur einen geringen Einfluss auf die Klassifikationsergebnisse hat. Unterschiede der Häufigkeiten zwischen den Modellen ( $<8\%$ ) können auf Unterschiede in der Windrichtungsbestimmungen zurückgeführt werden. Außerdem stößt die oWLK vor allem bei indifferenten Wetterlagen an ihre Grenzen, wenn zum Beispiel die Zyklonalität Werte nahe Null annimmt.

Weiterführend werden hagelrelevante Lagen und hagelirrelevante Wetterlagen mittels Heidke Skill Score (HSS) unterteilt. Es können vier verschiedene hagelrelevante und fünf hagelirrelevante Lagen identifiziert werden. Drei dieser vier hagelrelevanten Wetterlagen sind auf denselben meteorologischen Prozess zurück zu führen („Spanish Plume“). Durch einen Trog über dem Nordatlantik und einem Rücken über Mitteleuropa kommt es zur Advektion feucht-warmer Luft aus dem Mittelmeerraum oder vom Atlantik. Die Advektion dieser energiereichen Luftmassen erhöht

das Potential für hochreichende Konvektion und erklärt, warum es bei den genannten Wetterlagen häufig zur Entwicklung kräftiger Gewitter und damit einhergehend Hagel kommt. Dies zeigt, dass die oWLK nicht zwischen einzelnen meteorologischen Prozessen unterscheiden kann bestätigt aber, dass die klassifizierten Wetterlagen durchaus realistisch sind. Die oWLK ist damit eine geeignete Methode für die Untersuchung hagelrelevanter Wetterlagen.

Um zu zeigen, dass auch die jährliche Variabilität der hagelrelevanten Wetterlagen unabhängig vom Modell und der Modellauflösung ist, wird die jährliche Anzahl der hagelrelevanten Wetterlagen aus Reanalysedaten und CCLM-ERA40-Daten verglichen. Die Abweichungen dieser Anzahl zwischen den Modellen für den Kontrollzeitraum sind - ausgenommen für einzelne Jahre - relativ klein (<5%). Für die hagelirrelevanten Lagen sind sie etwas größer (<10%). Dies zeigt, dass die Modellauflösung nur geringe Auswirkungen auf die Variabilität hat.

Im Folgenden wird die oWLK durch Anwendung auf ein Ensemble aus acht verschiedenen Realisationen des regionalen Klimamodells COSMO-CLM dazu benutzt um festzustellen ob die Klimamodelle in der Lage sind Wetterlagen hinreichend gut wieder zu geben. Zur Validierung der Modelle werden die aus den Klimamodellen errechneten Häufigkeitsverteilungen der Wetterlagen mit denen des Referenzmodells CCLM-ERA40 für den Kontrollzeitraum C20 verglichen. Die Ergebnisse sind überraschend: Obwohl keine Initialisierung der Klimamodelldaten mit Beobachtungen stattfindet, sind die Wetterlagenverteilungen zwischen Klimamodellrealisationen und CCLM-ERA40 fast identisch. Abweichungen werden hauptsächlich durch den Zyklonalitätsindex in 500 hPa verursacht, der wie oben erwähnt bei Werten um seinen Grenzwert häufig zu Unterschieden in den Modellergebnissen führt. Die geringen Unterschiede zwischen Referenzmodell und den Klimamodellen zeigen, dass die Klimamodelle in der Lage sind Wetterlagen hinreichend abzubilden. Dies ist eine wichtige Grundlage für die Untersuchung der langzeitlichen Variabilität der hagelrelevanten Wetterlagen.

Lineare Trends von Zeitreihen der hagelrelevanten Wetterlagen wurden mit Hilfe von Trendmatrizen analysiert, bei welchen Start- und Endzeiten der Zeitreihen sukzessiv verschoben wurden. Die Signifikanz (80% Signifikanzniveau) wird mit Hilfe des Mann-Kendall-Tests bestimmt. Signifikante positive Trends von ca. neun Tagen können während des Kontrollzeitraums für Zeitreihen der hagelrelevanten Wetterlagen von zwei Klimamodellen festgestellt werden. Für den Projektionszeitraum zeigen drei der acht Klimamodelle statistisch signifikante positive Trends von bis zu ca. 11 Tagen. Außerdem kann in fast allen Modellrealisationen durch Anwendung einer Fast-Fourier-Transformation eine Periodizität von 12-16 sowie 2-5 Jahren ermittelt werden. Dies deutet darauf hin, dass das Potential für Hagel harmonisch schwankt. Es ist zu bemerken, dass die ermittelten Trends sehr stark von Initialisierungszeit und -bedingungen des antreibenden Globalmodells abhängen, welche auch die größten Unterschiede in der absoluten Häufigkeit der Wetterlagen verursachen. Weiterhin werden Unterschiede vom antreibenden Globalmodell (ECHAM5, CCCma3) selbst hervorgerufen, wohingegen die Version des Regionalmodells (3.1 und 4.8) sowie die verschiedenen Emissionsszenarien (A1B und B1) nur wenig Einfluss auf die ermittelten Trends haben. Diese Unterschiede deuten auf große Unsicherheiten in den Klimaszenarien hin.

Aufgrunddessen sollten die acht verschiedenen Modellrealisationen nicht als Klimavorhersage, sondern eher als mögliche Entwicklung der hagelrelevanten Wetterlagen gedeutet werden.

Um die potentielle Entwicklung der hagelrelevanten Wetterlagen der verschiedenen Realisationen zusammenzufassen und die epistemischen Unsicherheiten (Unsicherheiten die bekannt, aber nicht Messbar sind) zu berücksichtigen, wurden die Zeitreihen der Wetterlagen zu einem Ensemble gebündelt (Mittelwert und Standardabweichung). Signifikante Langzeittrends sind sowohl für den Kontrollzeitraum (von 35 auf 47 Tage), als auch für den Projektionszeitraum (von 39 auf 46 Tage) zu erkennen. Die Zunahme der Tage mit hagelrelevanten Wetterlagen erklärt vermutlich zum Teil die Häufung der Hagelschäden, welche von der SV beobachtet werden konnten ( $\approx 15$  days). Dies impliziert, dass die Ergebnisse durchaus repräsentabel sind.

Um die Ergebnisse verifizieren zu können wird die Anzahl der Hagelschadentage mit Hilfe eines statistischen Modells modelliert, welches die Wetterlagen als Eingabegröße benutzt. Der Vorteil dieser Methode besteht darin, dass alle 40 möglichen Wetterlagen bei der Berechnung der Tage berücksichtigt werden und nicht, wie vorher erörtert, nur die vier hagelrelevanten Lagen. Die Ergebnisse auf Grundlage der Wetterlagen von CCLM-ERA40, ERA40 und ERA-Interim stimmen sehr gut mit der Anzahl der Schadenstage der SV überein. Für den Zeitraum 1986 bis 2000 wurden an durchschnittlich 15 Tagen pro Sommerhalbjahr Hagelschäden an die Versicherung gemeldet, welche vom Modell bestätigt werden. Die Wahrscheinlichkeitsverteilung des Modells zeigt, dass es auf Grundlage der Wetterlagen mit einer Wahrscheinlichkeit von über 90% mindestens 13 und höchstens 17 Hagelschadenstage gab.

Durch Anwendung des Modells auf die Klimamodelldaten kann auch die Anzahl der Hagelschadenstage für den Projektionszeitraum analysiert werden. Dazu werden die Klimamodelle für den Zeitraum 1986 bis 2000 mit der Verteilung der Hageltage von CCLM-ERA40 fehlerkorrigiert. Auch mit dieser Methode kann eine Zunahme der Tage mit Hagelschäden beobachtet werden. Für drei der Modellrealisationen liegt die Wahrscheinlichkeit für mehr als 15 Hageltage pro Sommerhalbjahr für die Jahre 2031-2045 über 90% und für drei weitere Modellrealisationen sind es mindestens 14 Tage. Es sollte bedacht werden, dass dies die minimale Anzahl der Hageltage darstellt und daher oft eine höhere Anzahl zu erwarten ist. Andererseits zeigen einige der Modellrealisationen trotz Fehlerkorrektur eine Abnahme der Hagelschadenstage zwischen 1986 bis 2000 und 2001 bis 2015, was auf mehrjährige Extrema in den Zeitreihen zurückzuführen ist. Diese haben einen starken Einfluss auf die Trends. Ob die Extrema auf Periodizitäten beruhen sollte weiter untersucht werden.

Es kann gezeigt werden, dass es möglich ist die oWLK auf verschiedene Datensätze anzuwenden. Auch die regionalen Klimamodelle sind in der Lage Wetterlagen hinreichend gut darzustellen, um sie für langzeitliche Analysen zu verwenden. Die Anwendung verschiedener statistischer Methoden macht es möglich die zukünftigen Entwicklungen von schadensträchtigen Gewitterstürmen abzuschätzen. Daher könnten diese Methoden benutzt werden, um weitere meteorologische Phänomene [wie z.B. Tornados (Bissolli et al., 2007) oder Hochwasser (Bardossy and Filiz, 2005)] mit Wetterlagen zu untersuchen und die Wahrscheinlichkeit dieser Extremereignisse für die Zu-

kunft abzuschätzen. Für solche Studien sollten weitere regionale Klimamodelle mit einbezogen werden um die epistemische Unsicherheit zu minimieren. Dies stellt sicher, dass die natürliche Variabilität untersucht wird und nicht nur die Modellphysik eines einzelnen regionalen Klimamodells. Ein Ensemble sollte daher eine große Anzahl von verschiedenen regionalen Klimamodellen und unterschiedliche antreibende Globalmodelle berücksichtigen.



# Contents

<b>1</b>	<b>Introduction</b>	<b>3</b>
<b>2</b>	<b>Theoretical Background</b>	<b>7</b>
2.1	Static Stability . . . . .	7
2.2	Condensation levels . . . . .	11
2.3	Stability and thunderstorm measures . . . . .	12
2.4	Development and characteristics of thunderstorms . . . . .	16
2.5	Development of hail . . . . .	19
<b>3</b>	<b>Data sets and methods</b>	<b>23</b>
3.1	Data sets . . . . .	23
3.1.1	Reanalysis data and regional climate models . . . . .	23
3.1.2	Objective weather type data for Germany . . . . .	26
3.1.3	Meteorological station data . . . . .	26
3.1.4	Insurance data . . . . .	27
3.2	Weather type classifications schemes . . . . .	27
3.2.1	Subjective weather type classification after Hess and Brezowsky . . . . .	27
3.2.2	Objective weather type classification (oWLK) - DWD . . . . .	28
3.3	Statistical methods . . . . .	32
3.3.1	Categorical verification . . . . .	32
3.3.2	Trend analysis and statistical significance . . . . .	35
3.3.3	Frequency analysis . . . . .	37
3.3.4	Probabilistic Forecast of hailstorm events . . . . .	38
<b>4</b>	<b>Validation and detection of hail-related weather types</b>	<b>41</b>
4.1	Validation of CLM-ERA40 derived weather types . . . . .	41
4.2	Validation of the regional climate model realizations . . . . .	53
4.3	Evaluation of a modified weather type classification . . . . .	58
<b>5</b>	<b>Temporal variability of hail-related weather types</b>	<b>67</b>
5.1	Temporal variability of hail-related weather types . . . . .	67
5.1.1	Detection of linear trends . . . . .	67
5.1.2	Detection of periodicities . . . . .	74

---

5.1.3	Variability of hail-related weather types in an ensemble of regional climate models . . . . .	74
5.2	Variability of hail-unrelated weather types . . . . .	76
5.2.1	Detection of linear trends . . . . .	76
5.2.2	Detection of periodicities . . . . .	79
5.2.3	Variability of hail-unrelated weather types in an ensemble of regional climate models . . . . .	80
<b>6</b>	<b>Statistical modeling of hail damage days</b>	<b>85</b>
6.1	Determination of hail damage day probabilities . . . . .	85
6.2	Prediction of hail damage days . . . . .	86
<b>7</b>	<b>Summary and conclusion</b>	<b>93</b>
<b>A</b>	<b>Weather types</b>	<b>97</b>
<b>B</b>	<b>Skill Scores</b>	<b>101</b>
<b>C</b>	<b>Modified weather type classification</b>	<b>103</b>
<b>D</b>	<b>Analysis of hail-related weather types</b>	<b>105</b>
D.1	Hail-related weather types . . . . .	105
D.2	Hail-unrelated weather types . . . . .	107
<b>E</b>	<b>Prediction of hail damage days</b>	<b>111</b>
	<b>Literature</b>	<b>113</b>

# 1. Introduction

Thunderstorms are one of the major natural hazards affecting Germany. Especially during the summer months, thunderstorms can develop to severe complexes that are associated with heavy rainfall, gusts, tornadoes or hail. These events, which occur several times each year in Germany, pose a significant threat to humans and their assets. In the federal state of Baden-Württemberg, almost 40% of all damage to buildings can be attributed to large hailstones (Kunz and Puskeiler, 2010).

In recent years, the number of days with hail damage occurrence determined by the number of settled claims of the SparkassenVersicherung AG insurance company has significantly increased (Fig. 1.1). This poses problems especially to insurance companies, the construction industry and agriculture.

According to the fourth assessment report conducted by the Intergovernmental Panel on Climate Change (IPCC; IPCC, 2007), the global mean temperature increased in the last century (1906-2005) by about  $0.74^{\circ}\text{C}$  ( $\pm 0.18^{\circ}\text{C}$ ). This raises the question whether there is a link between tem-

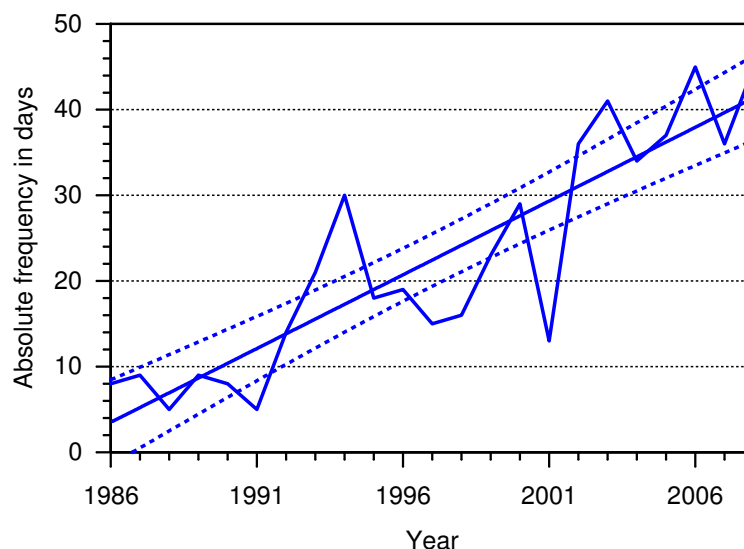


Figure 1.1: Number of hail damage days per year according to reports of the SV building insurance company in Baden-Württemberg. A hail damage day is defined as a day with more than 10 settled claims (Kunz et al., 2009). Indicated are the linear trend (solid) and the 95% confidence intervals (dashed).

perature and changes in the hail frequency, as well as what can be expected for the future.

However, estimating the hazard associated with hailstorms is very difficult. As thunderstorms and related hail streaks are often limited to a typical horizontal extent of only a few kilometers, they are regularly not captured by current surface observations systems. Additionally, remote sensing instruments, such as radars, are not yet able to detect hail, as no unique relationship between radar reflectivity and hail is established (Sauvageot, 1992; Kunz and Puskeiler, 2010). Furthermore, thunderstorms are mainly not captured in climate models because their horizontal extent is less than the spatial resolution of the model data. Hence, single- or multi-cells cannot be resolved by most models at all. Thus, there are basically no available time series of thunderstorm and hail observations that would allow to analyze their changes over an adequately long time period.

To overcome this problem, the parameters that are important for convective initiation, which are better understood and better measurable, can be used to determine the potential of thunderstorm development. These parameters describe thermal stratification of the atmosphere, moisture content and meso-scale uplift. Changes in these parameters are assumed to impact the probability of thunderstorm occurrence. Furthermore, these parameters can be linked to different large-scale weather patterns, which then favor to a certain extent the development of hailstorms.

Bissolli et al. (2007) found, for example, a strong relationship between some large-scale weather patterns, classified by the Deutscher Wetterdienst (DWD), and tornado occurrence in Germany. Furthermore, Bardossy and Filiz (2005) found similar relations to flooding and Ehmann (2009) to hail damage days in the recent decades. This diploma thesis builds up on those studies. The overall goal is to examine to what extent specific weather patterns can be related to damage-causing hailstorms as well as to study the natural long-term variability and periodicity of these specific patterns in the past and in future decades. Two different classification routines are used to categorize weather patterns determined by the relevant synoptic systems. The first one is invented by the DWD, while the second one is a modified version that is adjusted to hailstorm occurrence. Both routines are applied to reanalysis data and a small ensemble of eight different regional climate model realizations.

There are several questions to face in order to reach the objectives. One is the robustness of the classification method when applied to different data sets with a special focus on hailstorms. Reanalysis data (ERA40 and ERA-Interim) of the European Center for Medium-Range Weather Forecast (ECMWF) and data of a regional climate model CCLM-ERA40, initialized by ERA40 reanalyses, are used to investigate whether these similar data sets (all include observations) obtain similar distributions of the weather type frequency. The weather types are categorized into a subset that is frequently accompanied by hail damage (hail-related). For this examination, two different statistical methods were used. Likewise, it is possible to detect weather types that are only rarely accompanied by hail damage (hail-unrelated). The annual frequency of these weather-type groups derived from the three reanalysis data sets are compared to each other in order to determine if the method is applicable in terms of temporal variability. This kind of validation is fundamental as the indirect analysis regarding changes of damaging hailstorms is more prone to

errors with regard to the realistic number of hail damage. However, it might be a good approach since no hail observations are available for long time periods.

To investigate the temporal variability of the potential for hailstorm occurrence and to identify possible periodic behavior, data sets from different climate models are used. In doing so, the uncertainty of the results with regard to future reality is investigated. Data of eight different realizations of the regional climate model (RCM) COSMO-CLM for the time period 1971-2050 are used to account for uncertainty. On the one hand, there is an uncertainty due to processes or developments we cannot measure but know about (epistemic), for example, changes in human population or economy. On the other hand, there is uncertainty due to events that happen only randomly and cannot be quantified (aleatory). Thus, different realizations of CCLM are used, differing by the COSMO-CLM version (3.1 and 4.8), the driving global climate model (ECHAM5-MPI/OM, CCCma3), initialization times and initial conditions (Run 1 to 3) and the emission scenarios (A1B and B1). These data sets provide the basis for the analysis of natural variability, periodicity and trends of weather patterns that favor or inhibit thunderstorm occurrence.

This thesis is organized as follows: Chapter 2 focuses on the theory of thunderstorm development including the different organization forms and explains the development of hailstones. The following Chapter 3 gives an overview of the data sets and methods used. In Chapter 4, the classified weather types derived from results of different climate models are evaluated against reanalysis data and hail-relevant weather types are identified. Additionally, a modified classification method, which aims at finding a better relationship between weather types and damaging hailstorm occurrence, is introduced and applied. The analysis of temporal variability of hail-relevant and hail-irrelevant weather types is discussed in Chapter 5. Initially, the model realizations are analyzed separately to determine model related differences of temporal variability. Afterwards, the whole ensemble is considered. In Chapter 6, a statistical probabilistic model to identify the number of hail damage days from specific weather types is introduced and applied to verify results gained from previous chapters. Moreover, it is used to predict the number of hail damage days and to determine differences between various time periods. Finally, a summary with conclusions and a brief outlook is given in Chapter 7.



## 2. Theoretical Background

Thunderstorms develop in a convective atmosphere, where the motion is predominantly vertical and driven by buoyancy forces arising from static instability. This chapter is split into three sections. The first section of this chapter introduces the principal mechanisms and characteristics of the atmosphere that are relevant for vertical motions. The second section gives an overview about the different types of thunderstorms, while the third section explains how hail develops within a cumulus cloud.

### 2.1 Static Stability

Whether convection can develop is dependent upon the vertical stratification of the atmosphere. Distinction is made between three different types of stratification: stable, indifferent (neutral) or unstable. If the atmosphere is stable, an air parcel that gets vertically displaced will return to its initial position. If the atmosphere is neutral or indifferent, the air parcel stays in the position where it got moved to, while the atmosphere is called unstable when the displaced air parcel is further accelerated in the direction of the initial displacement and does not return to its initial position.

These three mechanisms can be explained by the first law of thermodynamics. Considering an homogeneous system without irreversible processes like friction or diffusion, the change of the internal energy  $du$  is given by:

$$du = \delta q + \delta a \quad (2.1)$$

with  $\delta q$  representing the rate of heat exchange and  $\delta a$  the rate of work on the system. These are incomplete differentials and are therefore written with  $\delta$  instead of a  $d$ . In the case of an air parcel, this work is directly related to volume changes ( $\delta a = -pd\alpha$  with  $\alpha = 1/\rho$  for the specific volume). Internal energy changes are proportional to changes in the temperature,  $du = c_v dT$ , with  $c_v$  as the specific heat capacity for a constant volume of air. With the enthalpy  $h = u + p\alpha$ , the first law can be converted to

$$\delta q = dh - \alpha dp. \quad (2.2)$$

Considering the change of the enthalpy  $dh = c_p dT$  with  $c_p$  as the specific heat capacity for constant pressure and an adiabatic system, where  $\delta q = 0$  (Eq. 2.2) gives:

$$dh = c_p dT = \alpha dp. \quad (2.3)$$

To quantify changes in the temperature associated with vertical motion in an heterogeneous system, that exhibits a vertical pressure gradient, the hydrostatic approximation

$$\frac{\partial p}{\partial z} = -\rho g \quad (2.4)$$

is inserted into Eq. (2.3). If an air parcel is lifted and experiences a lower pressure, it expands and, consequently, cools according to the dry adiabatic temperature gradient

$$\left. \frac{\partial T}{\partial z} \right|_{\text{dry}} = -\Gamma_d = -\frac{g}{c_p} = 0.0098 \text{ K m}^{-1}. \quad (2.5)$$

This gradient is valid for dry and also moist air with the specific heat capacity

$$c_{pm} = x_v c_{pv} + x_d c_{pd}, \quad (2.6)$$

with the indexes  $m$  for moist air,  $v$  for water vapor,  $d$  for dry air and  $x_v$  for the mass fraction of water vapor, if  $c_{pv} \approx c_{pd}$  and as long as condensation does not occur.

The relation between temperature gradient and upwards acceleration of an air parcel follows from the vertical component of the Eulerian equations of motion:

$$\frac{dw}{dt} = -g - \frac{1}{\rho} \frac{\partial p}{\partial z}. \quad (2.7)$$

$w$  is the vertical wind component,  $\rho$  the density of the air parcel and  $p$  the air pressure. With the equation of state

$$p = \rho R_L T \quad (2.8)$$

with  $R_L = 287 \text{ J kg}^{-1} \text{ K}^{-1}$  = gas constant for dry air, the hydrostatic approximation for the environment (index  $e$ ) and the quasi-static assumption that  $p = p_e$ , Eq. (2.7) yields

$$\frac{dw}{dt} = -g + \frac{1}{\rho} \rho_e g = g \left( \frac{\rho_e - \rho}{\rho} \right). \quad (2.9)$$

Insertion of the equation of state (Eq. 2.8) results in

$$\frac{dw}{dt} = g \left( \frac{T - T_e}{T_e} \right). \quad (2.10)$$

This equation shows that an air parcel is accelerated upwards if its temperature  $T$  is higher than the environment temperature ( $T > T_e$ ).

If the decrease in temperature of the environment is less than the dry adiabatic temperature gradient, the lifted parcel will be colder than the environment. Due to its' higher density, the parcel experiences a negative acceleration according to Eq. (2.9) and returns to the initial position, indicating that the atmosphere is stable. If the temperature gradient of the environment is equal to the

dry adiabatic gradient, the air parcel stays in the displaced position and the stratification is neutral. If the temperature of the environment decreases more than the dry adiabatic temperature gradient, the lifted air parcel will become warmer than the environment with a lower density. Consequently it becomes positively accelerated. The atmosphere is unstable and the ongoing lift can result into convective activity.

For saturated air masses the examination of static stability is equivalent, but the pseudo-adiabatic lapse rate has to be considered instead of the dry adiabatic one. If a saturated air parcel is lifted, the cooling rate is much lower compared to an unsaturated air parcel due to the release of latent heat through condensation. In this case the change in enthalpy is also controlled by the rate of the change in the saturation mixing ratio  $r_s$ :

$$dh = c_p dT + l dr_s \quad (2.11)$$

where  $l = 2.5 \times 10^6 \text{ J kg}^{-1}$  is the specific latent heat of vaporization. Hence, the temperature gradient is highly dependent on the humidity of the air volume and typically varies between 0.4 and 0.98 K per 100 meter. In general, the pseudo adiabatic lapse rate is lower than the dry adiabatic lapse rate, reaching

$$\left. \frac{\partial T}{\partial z} \right|_{ps} = -\Gamma_d \alpha_s \quad (2.12)$$

with  $\alpha_s =$  factor ranging between 0.3 and 1, if  $dr_s$  converges against zero at low temperatures (Kraus, 2004). The pseudo adiabatic lapse rate depends on the temperature of the air parcel and the prevailing air pressure because there is more condensation of water vapor in a warmer air parcel than it is in a colder one, according to the Clausius-Clapeyron equation. At very low temperature and pressure, the dry and pseudo adiabatic temperature gradient converge.

It is obvious that there is a thermal stratification which is stable without condensation and unstable with condensation. In this case the temperature gradient of the environment is between the dry adiabatic and pseudo adiabatic temperature gradient. This case is called conditional instability and stability/instability depends on whether condensation sets in. There is a high potential during these conditions that thunderstorms develop.

### Triggering mechanisms of vertical air motion

Vertical motion can be triggered by several different processes within the atmosphere. All these processes are a result of the differential heating of the ground or lowermost layers in the atmosphere (e.g. in the boundary layer), due to the terrestrial orbit and the declination of the axis of the earth (e.g. depending on the season). One region, where these differences are most pronounced, is the temperate zone between 50-60°N, where the polar air mass and the sub-tropical air mass converge. The resulting temperature and density gradients can lead to baroclinic instability and the formation of high- or low pressure systems.

The characteristics affecting vertical motion can be explained by the omega equation Eq. (2.13). It is a diagnostic equation, specifying the distribution of large-scale vertical motion. In a system with the pressure as vertical coordinate ( $p$ -system) it can be written as following (cf. quasigeostrophic theory):

$$\begin{aligned} \left( \sigma \nabla_p^2 + f_0^2 \frac{\partial^2}{\partial p^2} \right) \omega &= -f_0 \frac{\partial}{\partial p} [(\mathbf{v}_g \cdot \nabla_p) (\zeta_g + f)] + \nabla_p^2 \left[ (\mathbf{v}_g \cdot \nabla_p) \left( -\frac{\partial \phi}{\partial p} \right) \right] \\ &= \quad (1) \quad + \quad (2) \quad , \end{aligned} \quad (2.13)$$

where  $\omega$  is the vertical wind velocity in the  $p$ -system,  $\sigma$  is a stability parameter,  $f_0$  the Coriolis parameter assumed to be constant,  $p$  the pressure,  $\mathbf{v}_g$  the geostrophic wind vector,  $\zeta_g$  the geostrophic vorticity,  $f$  the planetary vorticity assumed to vary linearly along longitudes and  $\phi$  the geopotential. It is emphasized that diabatic effects are not depicted in Eq. (2.13) but are referred to in the text.

The omega equation (2.13) is a result of the difference between the vorticity equation, which was differentiated with respect to  $p$  ( $\frac{\partial}{\partial p}$ ) and the Laplace operator ( $\nabla^2$ ) of the geostrophic approximated heat equation. These assumptions are based on the experience that the geostrophic and hydrostatic balance are good approximations for both the averaged hydro- and thermodynamic conditions of the atmosphere (Beheng, 2007). According to Eq. (2.13) the large-scale uplift is controlled by two mechanisms, given by the two terms on the right side of the equation. The first term (1) controlling  $\omega$  is the differential vorticity advection and the second term (2) describes the advection of the thickness of the atmospheric layer, equivalent to the mean temperature advection.

Note that  $\omega$  can be put in relation to the vertical component of the velocity vector  $w$  in the  $z$ -system by:

$$\frac{dp}{dt} = \omega = \frac{\partial p}{\partial t} + \mathbf{v} \cdot \nabla p \approx \omega \frac{\partial p}{\partial z} = -\rho g w \quad (2.14)$$

This approximation is made on the basis of an order of magnitude suggestion. Hence, in case of lifting,  $\omega$  is negative, while  $w$  is positive.

According to Eq. (2.13) lifting can be expected in a region with positive vorticity advection increasing with height (or decreasing negative vorticity advection), which can occur downstream of a trough. Or in an area with a maximum layer thickness advection due to warm air advection, for example, in front of a warm front. Moreover, latent warming (Holton, 1972) can lead to lifting as well. Hence, lifting is highest in the vicinity of a short-wave pressure system because of the higher relative vorticity ( $\zeta_g$ ) advection compared to the planetary vorticity ( $f$ ) advection.

## 2.2 Condensation levels

If an air parcel is accelerating, as described in the previous section, it can reach a certain level where condensation sets in. The different condensation levels, dependent on the trigger mechanism, will be explained in this section and an overview of the detection of these levels on the thermodynamic diagram by Stüve will be given.

### Lifting condensation level

If an air parcel is lifted dry adiabatically, for example when flowing over an orographic obstacle or a front, the level where condensation starts is called the lifting condensation level (LCL). Since clouds can develop at this level, it is equivalent to the lowermost cloud level. On thermodynamic charts (e.g. tephigram, skewT-logp or Stüve) this level is located where the dry adiabatic curve, based on the near-surface temperature, and the line of constant saturation mixing ratio, based on the dew-point at the surface, intersect (see Stüve diagram in Fig. 2.1).

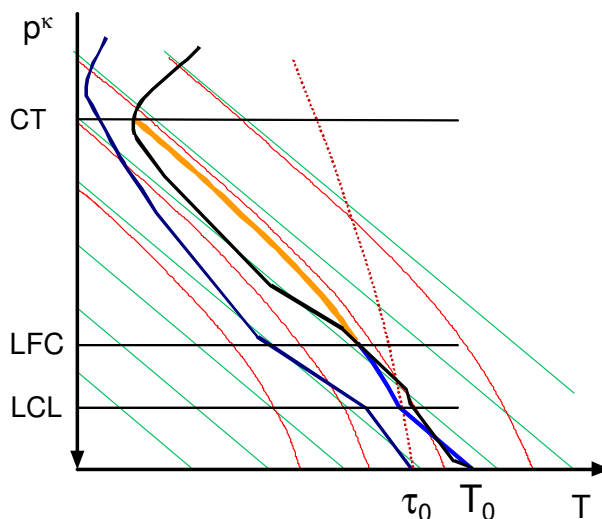


Figure 2.1: Schematic of the lifting condensation level (LCL), the level of free convection (LFC) and the cloud top (CT) on the Stüve diagram. Green: dry adiabats; Red: moist adiabats; Red dotted: saturation mixing ratio.  $T_0$  is the temperature and  $\tau_0$  the dew-point at the ground (Kunz et al., 2006).

### Convective condensation level

In contrast to the passive uplift, an air parcel can also actively become buoyant, by surface warming due to intensive solar irradiation or cooling aloft. This process can proceed as follows. In the morning, the atmosphere nearest to the surface is usually stably stratified due to long-wave emissions. If the stratification close to the ground becomes adiabatic or superadiabatic, air parcels can rise upwards resulting in vertical exchange of heat and humidity. The buoyancy of the air parcels will continue until the air parcel and the surrounding have the same temperature. This is the case when a slightly superadiabatic air parcel reaches a level where it has the same temperature as the environment. This level is termed convective condensation level (CCL) and indicates

the possibility of further ascent.

On the Stüve diagram this level is the point where the line of constant saturation mixing ratio (based on the dew-point temperature at the ground) intersects with the vertical temperature profile. Following this level dry adiabatically to the ground gives the convective temperature, which is the minimum temperature that has to be reached on the ground for triggering convection.

### Level of free convection

If the stratification of the atmosphere is conditional unstable and a volume of air is lifted by external forces, it may reach a certain height, where it is warmer than the environment and thus becomes positively accelerated. This height is called the level of free convection (LFC). It is the height where the moist adiabatic curve from the LCL and the vertical temperature profile intersect in the Stüve diagram (Fig. 2.1).

### Equilibrium level

The equilibrium level (EL) or cloud top (CT) is defined as the level where the temperature and density of the air parcel become identical and, thus, the upwards acceleration is zero.

The EL is located where the moist adiabatic curve, based on the CCL, LCL or LFC, intersects with the temp curve. For deep convection this level is usually near the tropopause. Because of the inertia of the air parcels, the actual CT can be a few hundred meters higher than the EL, for example when clouds overshoot into the tropopause. This is a characteristic feature of intense cumulonimbus clouds.

## 2.3 Stability and thunderstorm measures

The stability of the atmosphere can be described by various energy parameters and convective indices. They are calculated from temperature and moisture, sometimes complemented by kinetic parameters, and give an idea about the atmospheric potential for thunderstorm development according to the properties of the prevailing air mass. For example, Kunz (2007a) evaluated which of these indices and parameters are the best to predict isolated and severe thunderstorms. This chapter will introduce convective indices considered in this thesis (cf. Chapter 3).

### Potential temperature

The potential temperature is defined as the temperature of an air parcel that is moved dry adiabatically from the pressure level  $p$  to the level  $p_0 = 1000$  hPa. It is a conserved quantity for adiabatic processes and proportional to the entropy of an air parcel:

$$\theta = T \left( \frac{p_0}{p} \right)^\kappa \quad (2.15)$$

with  $p_0 = 1000$  hPa and  $\kappa = R/c_p = 0.286$ .

### Equivalent potential temperature

The equivalent potential temperature, defined by

$$\theta_e = \theta \exp\left(\frac{lr_s}{c_p T}\right), \quad (2.16)$$

is the temperature of an air parcel that is lifted dry adiabatically until it reaches the level of condensation and pseudo adiabatically afterwards, until the whole water vapor is condensed assuming that all water instantaneously leaves the volume. Thereafter it is moved dry adiabatically down to the level  $p_0 = 1000$  hPa. Consequently, this temperature reflects the latent energy of the condensation process. During a moist adiabatic process,  $\theta_e$  is constant with height.

### Convective Available Potential Energy

The convective available potential energy (CAPE; Moncrieff and Miller, 1976) is the potential energy a parcel would have, if lifted pseudo adiabatically from the LFC or CCL to the EL. It measures the energy that is available for convection and describes the ability of an air parcel to become buoyant. The CAPE can be calculated as:

$$CAPE = R_l \int_{LFC}^{EL} (T_v - T_{v_e}) d \ln p \quad (2.17)$$

with  $T_v$  for the virtual temperature of the air parcel and  $T_{v_e}$  for the virtual temperature of the environment.

If an air parcel is lifting CAPE values are high and indicate a higher potential for severe weather. As CAPE transforms to kinetic energy, the vertical wind velocity can be determined as

$$w = \sqrt{2CAPE}. \quad (2.18)$$

In the skewT-logp thermodynamic diagram the CAEP is proportional to the area between the moist adiabatic lifting curve of an air parcel and the temp curve above the LFC. In Table 2.1 characteristic values for the CAPE with respect to the thunderstorm development are presented.

Table 2.1: CAPE values and thunderstorm probabilities for southern Germany according to Kunz (2007a).

CAPE in $\text{J kg}^{-1}$	Thunderstorm probability
< 400	Thunderstorms unlikely
400 - 1500	Thunderstorms likely
> 1500	Severe thunderstorms with hail likely

### Lifted Index

The Lifted Index (LI; Galway, 1956) is the difference between the air temperature in 500 hPa and the temperature of an air parcel that was lifted dry adiabatically from the surface to the LCL and from there moist adiabatically to 500 hPa:

$$LI = T_{500hPa} - T_{surface \rightarrow 500hPa}. \quad (2.19)$$

If the equation yields a negative temperature, the air parcel in 500 hPa is warmer than the environment and the atmosphere is assumed to be unstable. If LI is positive, the atmosphere is stable and thunderstorms are unlikely (cf. Table 2.2).

Table 2.2: LI values and thunderstorm probabilities for southern Germany according to Kunz (2007a).

LI in K	Thunderstorm probability
> - 1	Thunderstorms unlikely
(-1) - (-4)	Thunderstorms likely
< -4	Severe thunderstorms with hail likely

### Showalter Index

The Showalter Index (SI; Showalter, 1953) is similar to the LI but refers to the temperature difference between 500 hPa and of an air parcel lifted from 850 hPa to 500 hPa:

$$SI = T_{500hPa} - T_{850hPa \rightarrow 500hPa}. \quad (2.20)$$

The advantage of this index is that it is less dependent on the surface properties, compared to the LI. Negative values indicate that the lifted air parcel is warmer than the environment and becomes positively accelerated (cf. Table 2.3).

Table 2.3: SI values and thunderstorm probabilities for southern Germany according to Kunz (2007a).

SI in K	Thunderstorm probability
> 2	Thunderstorms unlikely
2 - 0	Thunderstorms likely
< 0	Severe thunderstorms with hail likely

### Potential Instability Index

Van Delden (2001) introduced another thunderstorm index which is based on the fact that thunderstorm development is related to the potential instability of the atmosphere. If the atmosphere

is unstable,  $\theta_e$  decreases with increasing height. This characteristic is used to define the Potential Instability Index (PII)

$$PII = (\theta_{e925hPa} - \theta_{e500hPa}) / (Z_{500hPa} - Z_{925hPa}). \quad (2.21)$$

$Z$  is the height of the pressure levels, the unit of PII is  $K km^{-1}$ . The values of PII for southern Germany can be seen in Table 2.4 (Kunz, 2007a).

Table 2.4: PII values and thunderstorm probabilities for southern Germany according to Kunz (2007a).

PII in $K km^{-1}$	Thunderstorm probability
< 0	Thunderstorms unlikely
0 - 1	Thunderstorms likely
> 1	Severe thunderstorms with hail likely

### Deep convective Index

This convective parameter, introduced by Barlow (1993), is based on the LI and combines the properties of equivalent potential temperature at 850 hPa with the latent instability at the surface (Haklander and Delden, 2003). The Deep convective Index (DCI) designed to predict severe thunderstorms is defined by:

$$DCI = (T + \tau_0)_{850hPa} - LI \quad (2.22)$$

with  $\tau_0$  as dew-point temperature. The higher the values of DCI the higher is the probability for deep convection to occur (cf. Table 2.5).

Table 2.5: DCI values and thunderstorm probabilities for southern Germany according to Kunz (2007a).

DCI in K	Thunderstorm probability
< 21	Thunderstorms unlikely
22 - 24	Thunderstorms likely
> 24	Severe thunderstorms with hail likely

### Vertical Totals

The Vertical Totals (VT; Miller, 1972) is defined as the vertical temperature difference between 850 and 500 hPa

$$VT = T_{850hPa} - T_{500hPa}. \quad (2.23)$$

If the temperature difference is higher than 28 K, thunderstorms are likely. If the VT in southern Germany reaches values larger than 30 K, the potential for thunderstorm development is high (Kunz, 2007a).

## 2.4 Development and characteristics of thunderstorms

Severe thunderstorms occur above all during the summer months in Central Europe. They are often accompanied by weather phenomena such as wind gusts, heavy rainfall, lightning or even hail and tornadoes. They are a manifestation of deep convection and, thus, strongly rely on conditional instability, the moisture content (especially in the lowermost layers of the atmosphere) and a triggering mechanism that lifts an air parcel to the LFC or CCL (cf. Sec. 2.1). Triggering mechanisms may comprise buoyancy related to solar radiation at surface level, synoptic-scale uplift in front of a trough (cf. omega equation), forced uplift due to flow over mountains, uplift on frontal zones (cf. Eq. 2.13) or convergence zones developing in the context of thermal direct circulations like land sea circulations or mountain and valley winds. Furthermore, another important factor controlling the kind of storm organization is the vertical shear of the horizontal wind (Weisman and Klemp, 1986). Depending on the strength of the vertical wind shear in terms of speed and directional shear and the amount of convective energy, some types of thunderstorms may exist for several hours.

### Single-cell thunderstorms

Single-cells thunderstorms are the most frequent types of thunderstorms that occur in Central Europe during the summer months. They usually develop during calm conditions due to a weak pressure gradient and weak vertical wind shear. When solar radiation heats the ground and accordingly the adjacent atmospheric layers up to higher levels, the stratification may become unstable and single-cells may develop. In the mean, the horizontal extent of a cell ranges from one to ten kilometers and the lifetime is between 30 minutes and one hour. Because of their short lifetime they are usually not associated with considerable damage.

Conceptually, a single-cell thunderstorm passes through three stages of development. In the first stage, (cumulus or developing stage; Fig. 2.2) a bubble of moist and warm air is ascending until it reaches the CCL or LFC, where clouds of the cumulus type can develop. In this process, latent heat of condensation is released and the air parcel is able to ascend further. Hence, the cloud is growing vertically. If the air parcel crosses the 0°-isotherm, cloud droplets can freeze and effectively grow, for example due to collision with supercooled liquid water drops forming graupel and eventually hail particles.

During the mature stage (Fig. 2.2), ice particles and rain drops descend due to their mass and induce a downdraft through frictional forces. This downdraft gets further accelerated by additional cooling due to melting/evaporation processes during sedimentation of the hydrometeors.

After some time, the downdraft cuts off the cell from the warm and moist inflow of air at lower

levels. This is the stage of dissipation (Fig. 2.2) when the development of the cell is finished and the single-cell dissolves.

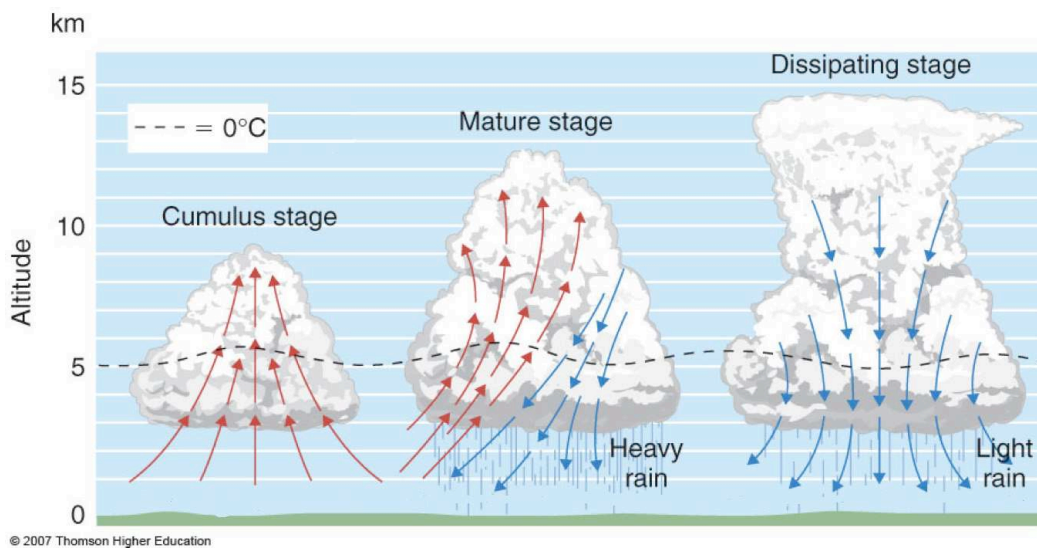


Figure 2.2: Life cycle of a single-cell including cumulus stage, mature stage and dissipating stage. Red arrows show the updraft areas, blue arrows the downdraft and the black dotted line the 0°-isotherm (<http://www.atmos.albany.edu>).

### Multi-cell thunderstorms

A multi-cell thunderstorm is a cluster of short-living single-cell thunderstorms that are in different stages of development. Multi-cells have a horizontal extent of more than ten kilometers and a lifetime of several hours. They develop in an environment with considerable vertical wind shear, in particular speed shear. The vertical shear of the horizontal wind velocity leads to a separation between the areas of up- and downdraft. Hence, the downdraft does not cut off the updraft and the cell complex can develop further. Due to this process, the downdraft induced on the rear side of the cell complex stretches underneath the warm and moist air on the ground (labeled as gust front) and, hence, triggers a new updraft in front of the multi-cell, where new single-cells can develop (Fig. 2.3). Because of these characteristics, multi-cells are usually accompanied by heavy rain, hail and gusts.

### Squall lines

Squall lines are lines of severe thunderstorms that usually form in connection with a cold front or convergence line. The mechanism maintaining this system is similar to that of the multi-cells with a strong gust front several kilometers ahead of the system. Squall lines have a high length-to-width ratio with a horizontal extent of more than 100 km; they may exist for several hours. They are characterized by a narrow region with heavy convective precipitation, maybe hail and a broad stratiform precipitation area in the rear.

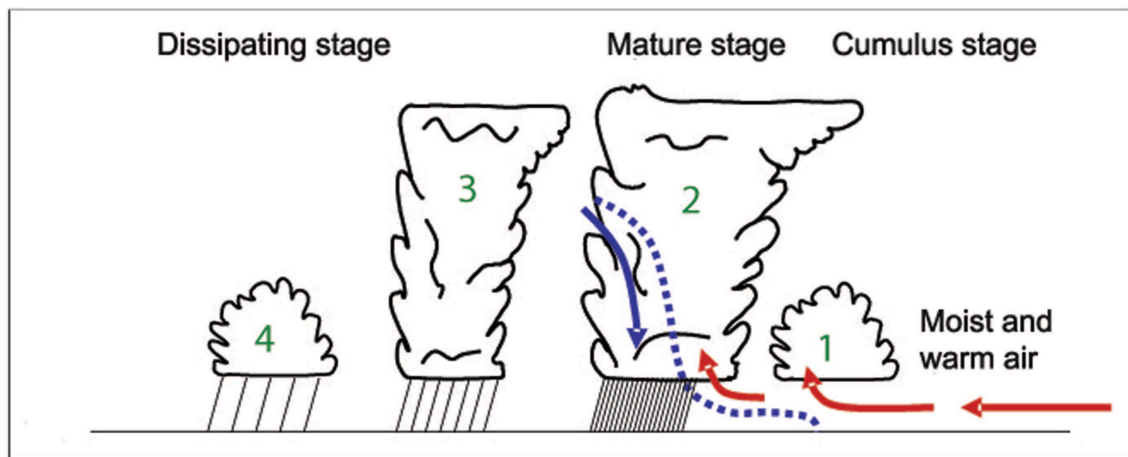


Figure 2.3: Life cycle of individual cells as part of a multi-cell complex. Cell one is in the cumulus stage, cell two and three are in the mature stage and cell four in the dissipating stage. The inflow of moist and warm air leads to an updraft (red arrow) while there is a separated downdraft in the back of the cell (blue arrow). The dotted line indicates the gust front at the ground (from Kunz et al., 2006).

### Mesoscale convective systems and complexes

A meso-scale convective system (MCS) usually develops in front of the warm sector of a low pressure system downstream of a mid-level trough, where synoptic-scale lifting prevails. Houze (1993) defined a mesoscale convective system as an ensemble of thunderstorms with a horizontal precipitation area of at least 100 km<sup>2</sup>, which also comprises squall lines. In contrast, a meso-scale convective complex (MCC) is defined after Maddox (1980) by a cloud shield with a horizontal extent of more than 100,000 km<sup>2</sup> on the  $\leq -32^{\circ}\text{C}$  temperature level. In addition, the interior cold cloud region with a temperature of  $\leq -52^{\circ}\text{C}$  must have an area larger than 50,000 km<sup>2</sup> and must persist for more than six hours. Both, MCS and MCC, are characterized by widespread precipitation areas with embedded convection cells and can exist for several hours.

### Super-cell thunderstorms

A super-cell thunderstorm develops in connection with meso-scale lifting downstream of an upper-air trough in an environment with strong vertical wind shear of both speed and directional shear. It can be interpreted as a very large and strong single-cell with two downdraft regions that additionally rotates (Fig. 2.4). The rotation is triggered by the directional shear of the horizontal wind that induces vorticity to the flow, such that air in the updraft is vertically tilted, with the consequence that the horizontal axis of the vorticity component related to the wind speed shear becomes vertically orientated (i.e. tilting). Due to the strong acceleration in the updraft, the air parcels are vertically stretched, further increasing the horizontal components of the vorticity (with a vertical axis) due to the conservation of angular momentum (i.e. stretching). According to the vorticity equation (e.g., Dutton, 1986), these two mechanisms lead to a significant increase of

horizontal vorticity on a local scale, a feature that may also lead to the formation of a tornado. The wind shear separates the regions of up- and downdraft allowing an permanent energy supply. Thus, super-cells may exist for several hours. A lifted inversion, for example, favors the development of super-cells, as it acts to block the triggering during lower temperatures initially. Only when the heating reaches its maximum triggering of convection sets in, leading to an ascent of very warm energetic air. The development is forced by a low level jet in the lower troposphere (up to 700 hPa) that transports moist and warm air into the thunderstorm cell.

Super-cells are the most dangerous thunderstorms and always occur with high wind gusts, large hail, heavy precipitation and sometimes a tornado (Weisman and Klemp, 1986).

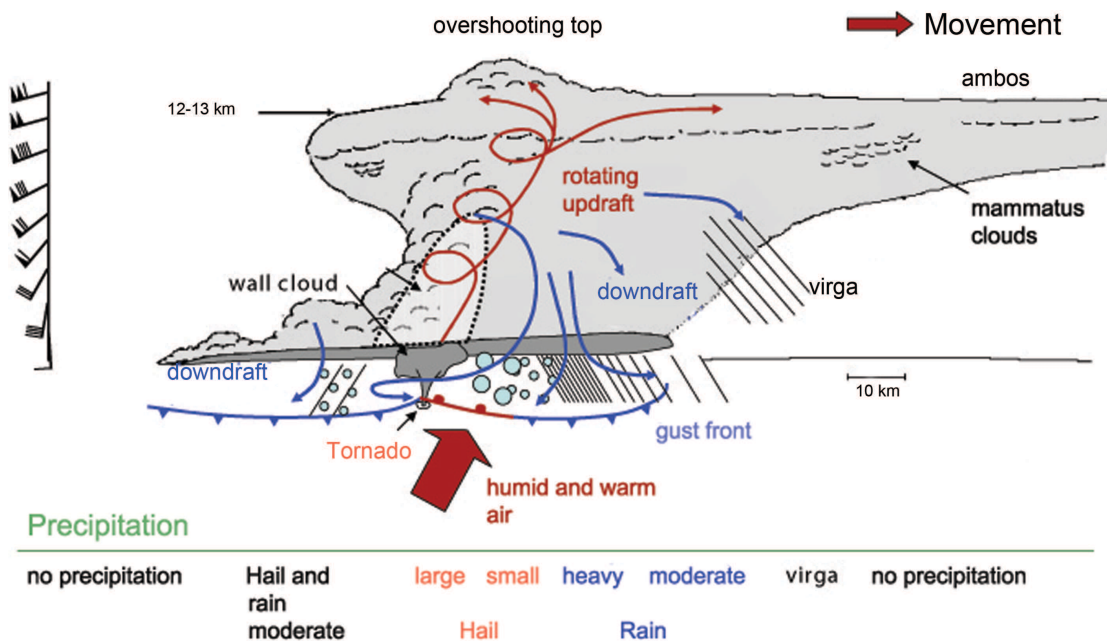


Figure 2.4: Vertical cross-section through a super-cell. The bold red arrows marks the rotating updraft and the inflow of moist and warm air to the super-cell, while the blue arrows show the separated downdrafts at the and in the rear of the cell (after Bluestein and Parks, 1983, modified by Kunz et al., 2006).

## 2.5 Development of hail

Hailstones are large ice hydrometeors with a bulk density of usually less than  $0.8 \text{ g cm}^{-3}$  and hence, less dense than pure ice ( $0.9 \text{ g cm}^{-3}$ ; List, 1958a and 1958b). A hailstone has per definition (Houze, 1993) a minimum dimension of 5 mm and is thus, larger than snow crystals, graupel (snow pellets) and ice pellets. The largest hailstone, for example, was found on July 23rd, 2010 in Vivian, South Dakota (US), and had a diameter of more than 20 cm (NCAR<sup>1</sup>). Due to their dimension and density, hailstones can cause major damage to buildings, cars and agriculture.

<sup>1</sup><http://www2.ucar.edu/magazine/features/all-hail>

For the evolution of hailstones a strong updraft in a thunderstorm is necessary. Updraft speeds of up to  $40 \text{ m s}^{-1}$  have been observed in deep convective storms (Crook, 1996; Xu and Randall, 2001). Within the updraft, cloud droplets and small raindrops are rapidly transported to regions with cold temperatures. However, these drops do not freeze at once, but remain liquid down to temperatures of less than  $-20^\circ\text{C}$ , due to the limited number of ice nuclei; these are known as supercooled droplets. Supercooled droplets may collide with ice particles that are moving from the rear downdraft region to the updraft region, causing them to freeze upon the ice surfaces. Through this process ice particles grow to sizes of one to five millimeters, which are by definition, graupel particles. This type of growth is called collection growth or riming and increases sharply with drop size (Pruppacher and Klett, 1997). These and irregular graupel particles are the basis for further development of hail and are therefore defined as hail embryos.

Because of the vertical wind shear in a thunderstorm cell, graupel particles may get into the updraft of the cloud. At the lateral sides of the rotating updraft of the thunderstorm (red line in Fig. 2.4) the updraft is only slightly larger than the gravitational force, making the vertical motion of the particles very slow. Accordingly, many ice crystals and supercooled water droplets can accumulate on a graupel particle allowing hailstones to grow very fast. This process is particularly effective in the region of the cloud where temperatures range between  $0^\circ\text{C}$  and  $\approx -15^\circ\text{C}$  and many of the supercooled droplets can be found. Sometimes, hailstones may grow to diameters of several centimeters. Thus, the size of a hailstone is dependent upon the vertical wind speed and the time span the hail embryos stay in the updraft region containing supercooled drops.

The properties of a hailstone are defined by two different kinds of collection growth (riming). During dry growth, the surface temperature of the hail embryos does not exceed the freezing/melting point, even if the water droplets release latent heat due to surface freezing on the graupel particles. Hence, the structure of the hailstone becomes opaque because of air pockets embedded within the growth layer.

If the surface temperature of the hailstone rises over the freezing/melting point due to the release of latent heat freezing of the supercooled droplets, the growth mechanism is called wet growth. Because of this process, the hailstone can evolve into a water-ice system, a so called spongy ice (Strangeways, 2007). The liquid water can flow into the air pockets and the structure of the hailstone becomes transparent. Remaining water splits off the surface of the hailstone in the form of liquid drops and may form a new hail embryo (shedding). Due to the change of the different types of growth and the permanent change between growth and melting in the cloud, hailstones often have a layered structure (Fig. 2.5).

When reaching the upper levels of a convective cloud, the hailstones may be transported by strong winds to the front side of the thunderstorm. While the thunderstorm is moving forward, the hailstones pass a region with a maximum updraft and are accelerated further. After leaving the updraft at the front of the thunderstorm, hailstones precipitate due to their large mass.



Figure 2.5: Profile of a hailstone, showing the layer structure caused by the change between growth and melt (<http://www.martin-wagner.org>).

The terminal fall velocity of hailstones depends on their diameter. Their speed ranges between 10 and 50 m s<sup>-1</sup> and can be described empirically by an equation of Pruppacher and Klett (1997), valid for an air pressure of 800 hPa, a temperature of 0°C and a diameter between 0.1 and 8 cm:

$$v \approx 9D^{0.8}, \quad (2.24)$$

with  $D$  for the diameter in cm and  $v$  in m s<sup>-1</sup>.



## 3. Data sets and methods

To categorize the relevant synoptic systems, the objective weather type classification of the German Weather Service (Deutscher Wetterdienst, DWD) is used and applied to reanalysis data from the European Center for Medium-Range Weather Forecast (ECMWF) and to an ensemble of eight different regional climate model (RCM) runs. The investigation area is Germany, but the methods applied are tested and adjusted for the German federal state of Baden-Württemberg only, where comprehensive loss data from a building insurance company is available.

In the first section, a short overview of the model and observational data is given, followed by an introduction of the weather type classification scheme of DWD and its application to model data. In the second part, methods to categorize the weather types into hailstorm-related types and hailstorm-unrelated types are outlined. Furthermore, the methods used to analyze the temporal variability of specific weather types are described.

### 3.1 Data sets

#### 3.1.1 Reanalysis data and regional climate models

For the determination of specific weather types, both reanalysis and climate model data are used. In the climate model data, the control runs include the years from 1971 to 2000, while the future projections are available for the years from 2001 or 2011 to 2050 for the IPCC emission-scenarios A1B and B1 (IPCC, 2007). The different scenarios estimate possible future developments of economy and population in the 21<sup>st</sup> century. The scenarios used for this thesis can be described as follows (IPCC, 2007):

- **A1B:** Future world with rapid economic growth and an increasing global population until the mid of the 21<sup>st</sup> century and a decreasing population afterwards. A quick spread of new and efficient technologies is assumed, as well as a balanced use of all energy sources. The income and way of life converges between regions and there are extensive social and cultural interactions worldwide.
- **B1:** Same population changes and growth of the economy as in A1B, but changes towards a service and information economy. The introduction of new clean and resource efficient technologies is expected and emphasis is put on global solutions to economic, social and environmental stability.

### **CCLM-KL**

The Consortium for Small-scale Modeling in Climate Mode (COSMO-CLM, abbreviated by CCLM), developed and applied by DWD, is a non-hydrostatic local climate model (Adrian and Frühwald, 2002). The CCLM consortial runs, hereinafter referred to as CCLM-KL, are based on the CCLM model version 3.1. Their horizontal spatial resolution is  $0.167^\circ$  ( $\approx 18$  km) and they are available for the control period C20 and the IPCC scenarios A1B and B1 for the time period from 2001 to 2048/50 (the A1B scenario is just available until 2048). The model is driven by the global coupled atmospheric-ocean model ECHAM5/MPI-OM (European Center/Hamburg Model Version 5/Max Planck Institute - Ocean Model) developed by the Max-Planck Institute for Meteorology, Hamburg (Germany). The ECHAM5 model is based on the weather forecast model of the ECMWF at T63 spectral resolution, while several parameterizations have been adjusted especially for the modeling of climate. Further details can be found, for example, in Roeckner et al. (2003). The calculations of the CCLM-KL were performed for the years 1950 to 2100 on a rotated grid and for two model runs. The thesis considers the period between 1971 and 2048/50. The two runs are driven by two different realizations of ECHAM5, which differ by about their starting point for 25 years.

### **CCLM-ECHAM5**

These CCLM runs are driven by the initial and boundary conditions of the global climate model ECHAM5. In comparison to the CCLM-KL runs the CCLM version 4.8 was used. This data set was calculated by the Institute for Meteorology and Climate Research (IMK-TRO) of the Karlsruhe Institute of Technology (KIT) within the project "Herausforderung Klimawandel", funded by the Ministry of the Environment, Nature Conservation and Transport Baden-Württemberg. The data sets of the first nesting step of two have a temporal resolution of six hours and a spatial horizontal resolution of  $0.44^\circ$  ( $\approx 50$  km). They are available for the European area from 1968 to 2000 and 2008 to 2050 and on four different pressure levels (1000 hPa, 850 hPa, 700 hPa and 500 hPa). The data of the first three years of each time period are not used due to the spin-up time of the model. Three different realizations of ECHAM5 for the A1B and B1 scenarios are used (cf. Table 3.1).

The values are available only on a rotated grid and the grid has to be rotated to a latitude/longitude grid, as in the following the wind direction needs to be calculated from the wind vectors. The re-rotation is performed by applying the Climate Data Operator (CDO<sup>1</sup>) software.

### **CCLM-CCCma3**

For the CCLM-CCCma3 model runs, the CCLM version 4.8 was initialized and driven by the third generation of coupled Global Climate Model (CGCM3) of the Canadian Center for Climate Modeling and Analysis (CCCma). The CGCM3 couples the third generation Atmospheric General Circulation Model (AGCM; McFarlane et al. 2005, Scinocca et al. 2008) of the CCCma and

<sup>1</sup><http://www.mpimet.mpg.de/fileadmin/software/cdo/cdo.pdf>

the three-dimensional Modular Ocean Model<sup>2</sup> (MOM) of the Geophysical Fluid Dynamics Laboratory (GFDL). The coupling between those models happened daily and included monthly flux adjustments for heat and fresh water as well as a monthly ocean surface temperature adjustment (Flato et al., 2000). The spatial horizontal resolution of the AGCM is 2.8°, while the resolution of the ocean model is approximately 1.4°, and thus, each atmospheric grid cell has 6 underlying ocean grids cells<sup>3</sup>.

The model runs of the CCLM-CCCma3 again were accomplished by IMK-TRO. The data sets have the same horizontal spatial and temporal resolution as the CCLM-ECHAM5 model runs and are available on a rotated grid. Likewise the IPCC scenario A1B was simulated.

Table 3.1: Overview of the regional climate models used in this thesis.

	CCLM-KL	CCLM-ECHAM5	CCLM-CCCma3
Model-version	COSMO-CLM 3.1	COSMO-CLM 4.8	COSMO-CLM 4.8
Forcing	ECHAM5 run 1, 2	ECHAM5 run 1, 2, 3	CCCma3
Emission-scenario	A1B, B1	A1B	A1B
Horizontal resolution	0.167° ≈ 18km	0.44° ≈ 50km	0.44 ≈ 50km
Simulation period	1971-2048/50	1971-2000 2011-2050	1971-2050
Referred to as	CKLC20R1 CKLA1BR1 CKLB1R1, ...	CE5C20R1 CE5A1BR1 CE5A1BR2, ...	CC3C20R1 CC3A1BR1

### ERA40/ERA-Interim

The ERA40 and ERA-Interim reanalysis, released by ECMWF, were calculated backdated with a current model version and include a large set of measurements, for example from radio soundings, satellites, buoys, airplanes and synoptic stations. The ERA40 reanalyses represents the climate of the period 1971 to 2001 and is available every six hours and with a spatial horizontal resolution of 1.25°, which is approximately 125 km, on a reduced Gaussian grid on 23 pressure levels (Uppala and coauthors, 2005).

ERA-Interim is an interim reanalyses from 1989 onwards and is developed by ECMWF in preparation to the next generation of reanalysis that is planned to replace the ERA40. Important improvements compared to ERA40 are, among others, a new and better humidity analysis, improved model physics and improvements due to observational systems. The corrected hydrological cycle leads to a better precipitation-evaporation ratio, which is globally closer to zero in comparison to the ERA40 reanalyses (Simmons et al., 2007). This makes this new generation of data more reliable than its preceding version.

<sup>2</sup><http://www.gfdl.noaa.gov/ocean-model>

<sup>3</sup><http://www.ec.gc.ca/ccmac-cccma/default.asp?lang=En&n=1299529F-1>

These data from these reanalysis are used for the determination of the different weather types and for the evaluation of the control runs of the different climate models. As they are incorporating observations, the two data sets are also used for evaluation purposes. The data sets were obtained at different pressure levels at 12 UTC from the Climate and Environmental Retrieving Archive (CERA<sup>4</sup>) data center. A problem, related to all model data downloaded from the CERA database, was negative values of humidity. Since these values almost exclusively occur at individual grid points at the uppermost pressure levels, they most likely result from the interpolation from model to pressure levels. To avoid any loss of data, the values are set close to zero in this study.

### **CCLM-ERA40**

For the CCLM-ERA40 model runs the CCLM version 4.8 was used and driven by initial and boundary condition of ERA40 (ECMWF; Par. 3.1.1) reanalyses. The data set was calculated on a rotated grid by IMK-TRO. The horizontal spatial resolution again of the first nesting step is 50 km and the data is available for 1968 to 2000. Again, the first three years are not considered. Due to the rotation of the grid, the same routine as for the CCLM-ECHAM5 data is applied to re-rotate the grid to a latitude/longitude grid.

### **3.1.2 Objective weather type data for Germany**

The DWD calculated objective weather types according to the classification method that will be presented in paragraph 3.2.2. The time series starts on July 1st, 1979 and is based on three different operational weather forecast models. Until the end of 1991, the weather types were calculated on the basis of the BKF (German for baroclinic-humid: 'baroklin-feucht') model which had a coarse spatial horizontal resolution of 254 km and a small number of vertical layers. Hence, the 1000 hPa level instead of the 950 and the 550 hPa instead of the 500 hPa had to be used. The BKF model was replaced in 1999 by the DWD European model (EM) with a horizontal resolution of approximately 55 km. Since 22 November 1999, the present operational global model GME is used, which is available on an icosahedral-hexagonal grid. Due to grid differences, the GME grid was interpolated to the grid of the EM (Bissolli and Dittmann, 2001). Weather types calculated by the DWD are available from their website<sup>5</sup>.

### **3.1.3 Meteorological station data**

To compare statistical distributions of stability indices derived from the model simulations for past decades with observations, data of the radiosonde station of Stuttgart in Baden-Württemberg are used. The station is operated by the DWD and located at an altitude of 314 m a.s.l. The values for temperature, mixing ratio and pressure at 12 UTC and the time period 1971 to 2000 are used to calculate the Lifted Index according to Eq. (2.19) in Section 2.3, starting from the surface. The values are merely used as estimates rather than to verify model results.

<sup>4</sup><http://cera-www.dkrz.de>

<sup>5</sup><http://www.dwd.de> - Klima und Umwelt; 29/03/2010

### 3.1.4 Insurance data

For the analysis of hailstorm-related weather types, loss data provided by the 'SV Sparkassen-Versicherung AG' building insurance company (hereafter referred to as SV) is used for the period from 1986 to 2008. The data is resolved in 5-digit postal code zones of Baden-Württemberg (Fig. 3.1) and includes the number of claims, value of reimbursement as well as the total number of contracts and the insured values per year, which are important for a correction of the data set. Even if the insurance data is strongly limited to settled regions that are affected by hailstorms and rely on the vulnerability of the buildings, they are currently the best available information about severe hailstorms.

In this thesis, a hail day is classified if more than 10 claims were settled on a day. This definition prevents non-severe hail days to enter the sample as well as failures due to a wrong assignment of the day.

From 1960 to 1994, an insurance for natural hazards was obligatory for any building (private and commercial) in Baden-Württemberg, exclusively offered by the "Gebäudeversicherung". But in 1994 this obligation was abolished. Nevertheless, approximately 70% of all buildings were still insured by the successor, the SV, until 2009. Due to the tempered change in the number of contracts, the loss data were annually normalized by mean value (Weber, 2006). In doing so, it is assumed that the portfolio remained constant over the entire time period.

### Damage to buildings caused by hailstones

The degree of damage and thus the amount of claims are controlled by the amount and the maximum size of the hailstones, the wind speed (hailstones get accelerated), but also by the exposure of the buildings. Newer buildings often feature a higher vulnerability due to roof windows or additional constructions such as solar panels, winter gardens or roller blinds. Other factors that influence the damage on buildings are shadowing effects by trees or other buildings and the used construction materials. Analyses by Stucki and Egli (2007), for example, showed that in the Switzerland 90% of all claimed damages are on residential buildings and a big fraction on roofs or claddings.

## 3.2 Weather type classifications schemes

### 3.2.1 Subjective weather type classification after Hess and Brezowsky

The subjective weather type classification is based on the calendar of large-scale weather types of Europe, created by Baur (1947). He defined large-scale weather types as the air-pressure distribution with at least the size of Central Europe that persists for several days. Baur analyzed surface weather charts and classified the prevailing cyclonic or anticyclonic weather types according to the geographical location of the pressure centers as well as the location and the extension of the frontal zones, yielding 21 different weather types.

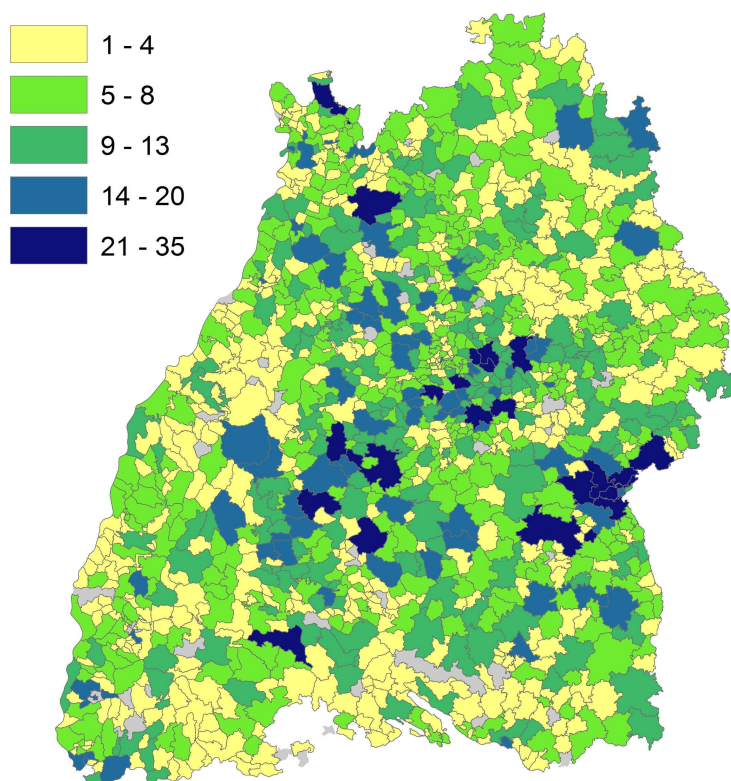


Figure 3.1: Number of days with hail damage claims in the corresponding postal code area between April and September of the years 1986 to 2000.

Due to improvements in meteorological observations, for example by additional aerological measurements, several changes in this classification method were conducted by Hess and Brezowsky (1952). They published the "Catalogue of larg-scale weather types of Europe" in 1952, which contains all weather types from 1881 to 1950. Important for the modified classification methods are the pressure distribution at sea level and the 500 hPa geopotential height charts, where troughs and ridges and the extension of the frontal zones are analyzed. Nowadays, 30 different weather types are distinguished (Appendix A.1) according to Gerstengarbe and Werner (2005). The weather types can be grouped into the three main categories of zonal, meridional and mixed-type circulations.

Since the subjective weather type classification is highly dependent on the analyst, this method is not used in this thesis. Nevertheless, it is the pioneer method in this area.

### 3.2.2 Objective weather type classification (oWLK) - DWD

The objective weather type classification (oWLK) by DWD considers three criteria that are combined into 40 different weather types. This includes the general flow direction in 700 hPa, which can give information about the potential stability of the atmosphere regarding the origin of the air mass, the vorticity in the lower and middle troposphere, which gives information about meso-

scale uplift, and the humidity in the entire troposphere. These properties are calculated on a selected grid of the DWD European model (EM) that covers Germany and a few adjacent regions. Since the target area is Germany, the grid points are weighted non-uniformly to avoid emphasis on grid points that are very close to the borders of the area, but already beyond the borders of Germany. Hence, the grid points in the center of the domain are weighted by a factor of three, the surroundings by a factor of two, whereas the ones that are close to the border of Germany are not weighted. The remaining grid points are not included in the calculation (Fig. 3.2; Bissolli and Dittmann, 2001). The resulting weather types are classified by a five digit identifier as follows:

$$AAC_{950}C_{500}H$$

with AA for the general flow direction (NE, SE, SW, NW, XX),  $C_{950}$  and  $C_{500}$  for vorticity in 950 and 500 hPa ( $C$  = cyclonal,  $A$  = anticyclonal) and  $H$  for the humidity ( $W$  = wet,  $D$  = dry).

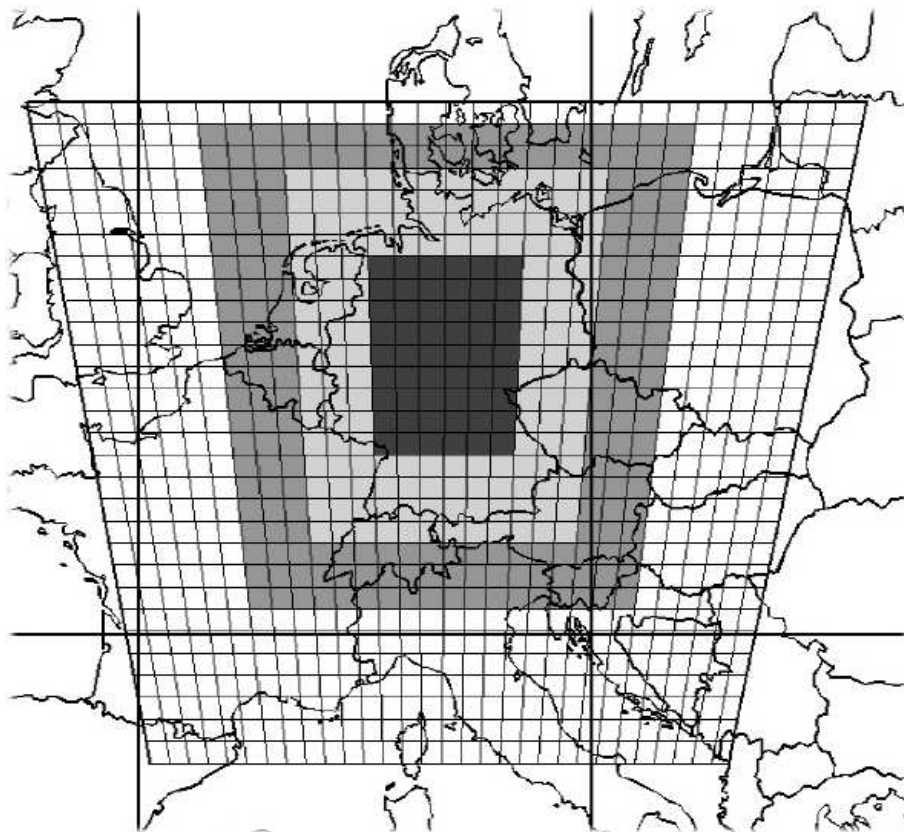


Figure 3.2: Classification area of the DWD objective weather type classification including three different weighted subareas. Within the central frame the grid point weight is three, within the surrounding frame it is two and the other gray shaded area has a grid weight of one. The grid area itself is based on the former DWD model EM (Bissolli and Dittmann, 2001).

### Advection type/ flow direction

The advection type (wind index) is derived from the  $u$ - and  $v$ -components of the wind vector at the 700 hPa level at each grid point considered by the weighting. To determine the wind direction, the wind rose (360°) is split into 36 direction sectors where each is 90° wide and shifted by 10° from each other (first sector is between 0° and 90°, second sector between 10° and 100°, last sector analogously between 350° and 80°). For each sector the number of grid points with a corresponding wind direction are counted and added up considering their grid weight. The sector with the maximum number of grid points is defined as wind index, if at least two thirds of the grid points are attributed to this sector. If these requirements are fulfilled, the sector with the maximum grid points is assigned to the main direction intervals:

- NE = northeast = [0°, 90°)
- SE = southeast = [90°, 180°)
- SW = southwest = [180°, 270°)
- NW = northwest = [270°, 360°)

If the threshold of 66.7% is not exceeded at any sector, the advection type cannot be clearly defined and is labelled by XX.

An example is the following: If the wind direction at a grid point with a grid point weight of three is 185°, it can be assigned to 9 different sectors ([180°, 270°) to [100°, 190°)) and shows up in these sectors for three times. In the case, the maximum wind sector is the sector [180°, 270°), including more than 2/3 of all grid points, the corresponding wind direction is defined as the center of this sector, thus 205° and accordingly SW.

### Cyclonality

The cyclonality index gives information about the bending of the geopotential areal at the 950 and 500 hPa levels. It is similar to the geostrophic vorticity in the p-system

$$\begin{aligned}\zeta_g &= \frac{1}{f} \nabla^2 \phi = \frac{1}{f} \left( \frac{\partial^2 \phi}{\partial x^2} + \frac{\partial^2 \phi}{\partial y^2} \right) \\ &\approx \frac{1}{f} \frac{\phi(i+1, j) + \phi(i-1, j) + \phi(i, j+1) + \phi(i, j-1) - 4\phi(i, j)}{(\Delta x)^2}\end{aligned}\quad (3.1)$$

calculated for every grid point  $(i, j)$  and averaged for each separate level, while  $\phi$  is the geopotential. Note that  $\Delta x \equiv \Delta y$  because of the equidistant grid so that  $(\Delta x)^2$  occurs in the denominator. The calculated values are indicators for the cyclonality index. A positive value is equivalent to cyclonality (C; positive vorticity), a negative one is equivalent to anticyclonality (A; negative vorticity).

### Humidity

The humidity index compares the precipitable water (PW) content of the troposphere on each day with a long-term mean. Therefore, the weighted areal mean of the PW is calculated as the integral of the mixing ratio from the lowermost (950 hPa) up to the uppermost pressure level (300 hPa):

$$PW = -\frac{1}{g} \int_{p_{950}}^{p_{300}} r dp = \frac{1}{g} \sum_{i=1}^5 \frac{1}{2} (r_{i+1} + r_i) (p_{i+1} - p_i) \quad (3.2)$$

where  $r$  is the mixing ratio

$$r = 0.622 \frac{R_H E}{p - R_H E}, \quad (3.3)$$

$R_H$  the relative humidity,  $E$  the saturation vapor pressure (in hPa) and  $i$  are the different pressure levels starting with the lowermost level. The PW values are calculated from temperature and relative humidity. Since the PW shows an inter-annual variation, corresponding to the temperature, the actual value is compared to an approximately 18 year daily average value (July 1979 to December 1996). If the value of PW is exceeding the average value, the atmosphere is denoted to as wet (W), if not, it is denoted to as dry (D). A list of all existing weather types can be found in Table A.2 in the Appendix.

### Adjustments of the oWLK software and its application to model data

For the classification of the different weather types, the geopotential, specific humidity and temperature at four pressure levels (1000, 850, 700 and 500 hPa) and wind on one pressure level (700 hPa) are used due to data availability. Hence, the cyclonality index for the lower troposphere is calculated at 1000 instead of 925 hPa. Accordingly, only the air-column between 1000 and 500 hPa is considered for computing PW. Furthermore, the specific humidity is used to calculate PW because the relative humidity downloaded from the CERA database was erroneous for ERA40 (cf. Sec. 3.1). Hence, the mixing ratio is computed from the specific humidity  $q_v$  as:

$$r = \frac{1}{\frac{1}{q_v} - 1}. \quad (3.4)$$

All model data considered are interpolated on a uniform grid since the models exhibit a different resolution and use different grids. The uniform grid has  $540 \times 270$  grid points, which corresponds to a horizontal spatial resolution of  $0.66^\circ$ . The used interpolation method is a bilinear interpolation conducted with the CDO routine "remapbil". After interpolation and re-rotation of the wind fields, an area including Germany and adjacent regions is cut out, using the CDO routine "selindexbox". The area includes 29 grid points in zonal direction and 21 grid points in meridional direction, starting in the lower left corner with the longitude  $44.333^\circ\text{N}$  and latitude  $0.667^\circ\text{E}$  (Fig. 3.3).

Since the interpolated grid of the data is cylindrical equidistant, the oWLK (Par. 3.2.2) requires an additional routine to calculate the geometrical distances between the grid points. This is necessary

to compute the cyclonality, which is derived by the horizontal Laplace operator of the geopotential (see Eq. 3.1) evaluated by the following numerical expression

$$\begin{aligned} \nabla^2 \phi &= \frac{\partial^2 \phi}{\partial x^2} + \frac{\partial^2 \phi}{\partial y^2} \\ &\approx \frac{\phi(i+1, j) + \phi(i-1, j) - 2\phi(i, j)}{(\Delta x)^2} + \frac{\phi(i, j+1) + \phi(i, j-1) - 2\phi(i, j)}{(\Delta y)^2}, \end{aligned} \quad (3.5)$$

where  $\phi(i, j)$  is the geopotential at the respective grid point,  $i-1$  or  $i+1$  are the neighboring grid points in zonal direction and  $j+1$  or  $j-1$  are the neighboring grid points in meridional direction. At the lateral sides, the values of the nearest calculated grid points are used.

The geometrical distances between the grid points are derived from the equation (Eq. 3.6) of distances on a circle:

$$x = r \arccos [\sin \varphi_1 \sin \varphi_2 + \cos \varphi_1 \cos \varphi_2 \cos(\lambda_1 - \lambda_2)] \quad (3.6)$$

where  $r = 6371$  km is the radius of the Earth,  $\varphi$  the latitude and  $\lambda$  the longitude.

During the evaluation it turned out that an error in the routine which calculates the flow direction in the original oWLK software, operationally applied by the DWD, slightly modified the results. Thus, all oWLK data provided by DWD may be affected by this error (this error was communicated and is now corrected in the DWD software). To avoid wrong values, the method has been modified. Instead of using the  $36 \times 90^\circ$  sections as described in Paragraph 3.2.2, the wind rose is split into four mean wind directions ( $[0^\circ-90^\circ)$ ,  $[90^\circ-180^\circ)$ ,  $[180^\circ-270^\circ)$  and  $[270^\circ-360^\circ)$ ). If at least 66% of the grid points exhibit a wind direction in one of these sectors, this wind direction is selected accordingly (NE, SE, SW or NW).

### 3.3 Statistical methods

#### 3.3.1 Categorical verification

To determine the prediction skill of the various weather type classifications with regard to their forecast skills of hailstorms, the methods of categorical verification are applied (Wilks, 1995). Table 3.2 shows the  $2 \times 2$  contingency table with the four elements  $a$  to  $d$  which are related to whether an event is observed (Yes/No) and/or predicted (Yes/No). The word "categorical" indicates that one and only one of these sets of possible events will occur. Hence, it does not contain expressions of uncertainties.

Assume, e.g., the weather type SWCAW (south-westerly flow direction, positive vorticity in 1000 hPa and negative vorticity in 500 hPa, wet in comparison to the climatological mean) prevailed for 20 days out of a total of 100 days and hailstorm occurred during 10 of these 20 days, then the correct event forecast is  $a = 10$ , while the false alarm forecast is  $b = 10$ . During the remaining days there are  $c = 5$  surprise events and the corresponding none events  $d = 75$  days.

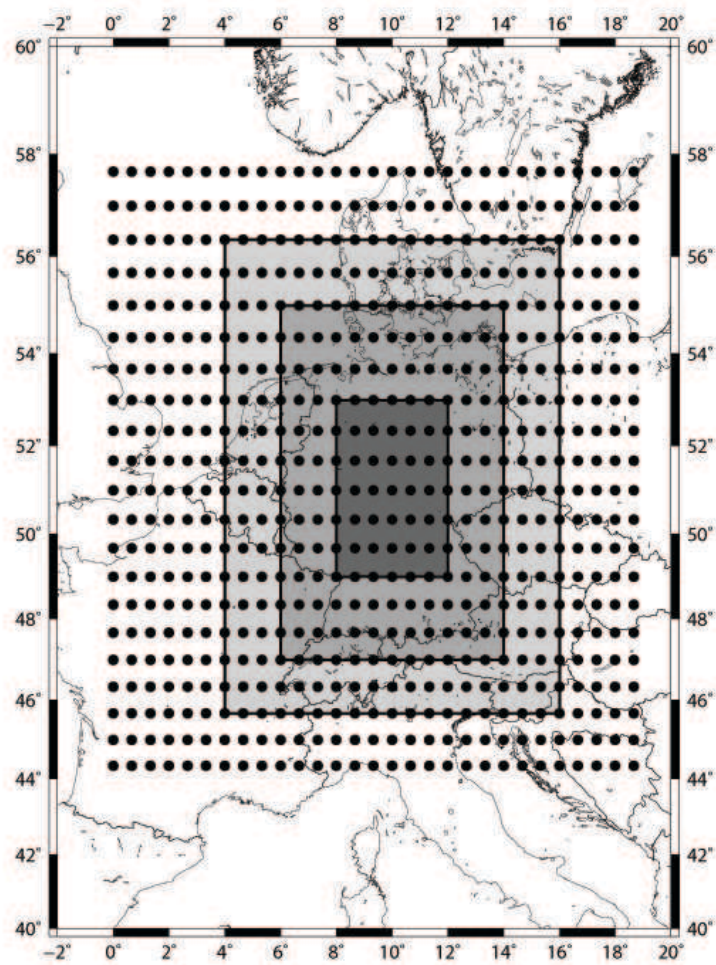


Figure 3.3: Interpolated and selected  $29 \times 21$  grid, used for the weather type classification. Shaded areas give information about the grid point weight as in Fig. 3.2.

Table 3.2: Contingency table for a dichotomous categorical verification of forecasts.

		Observation	
		<i>Yes</i>	<i>No</i>
Forecast	<i>Yes</i>	<i>a</i>	<i>b</i>
	<i>No</i>	<i>c</i>	<i>d</i>

Normalized by the total number of days  $n = a + b + c + d = 100$ , the relative frequency of the "Yes" or "No" forecasts or observation can be calculated.

According to the contingency table, a perfectly forecast goes along with zero false alarms as well as zero surprise events, i.e.  $b = c = 0$ . Besides this, several other accuracy measures of the forecast can be defined. A detailed description of these methods can be found, for example, in Wilks (1995). The most important skill scores are briefly discussed in the following and listed in Appendix B.

### Heidke Skill Score

When the fraction of hailstorm observations to no hailstorm observations is expected to be very small, the use of conventional accuracy measures does lead to high uncertainties. A combination of these skill scores, such as the Heidke skill score (HSS Heidke, 1926), gives more reliable estimates (Doswell et al., 1990), as it also considers random "Yes" and "No" forecasts.

$$HSS = \frac{(a + d)/n - [(a + b)(a + c) + (b + d)(c + d)]/n^2}{1 - [(a + b)(a + c) + (b + d)(c + d)]/n^2} \quad (3.7)$$

The reference accuracy measure used for the Heidke skill score is the Hit Rate (Appendix B.1). The HSS computes the relation between the true "Yes" and "No" forecasts and the randomly correct forecasts. The probability of a correct "Yes" forecast by chance is  $p_{yes} = [(a + b)/n][(a + c)/n] = (a + b)(a + c)/n^2$ , while the probability of a correct "No" forecast by chance is  $p_{no} = (b + d)(c + d)/n^2$  (Wilks, 1995). This simplifies Eq. (3.7) to:

$$HSS = \frac{a + d - R}{n - R}, \quad (3.8)$$

where  $R$  is the random chance that the forecast is correct:

$$R = \frac{(a + b)(a + c) + (c + d)(b + d)}{n}. \quad (3.9)$$

Thus, a perfect forecast has a HSS of one, while a forecast that is just randomly correct receives a negative HSS.

### Threshold detection

To improve the weather type classification method with regard to hailstorm prediction, categorical verification is used. A combination of skill scores (Appendix refapp:skillscores) is a common method to detect thresholds of, for example, thunderstorm indices (see Sec. 2.2) that relate higher (or lower) values of several indices with a higher thunderstorm potential (Kunz, 2007a; Haklander and Delden, 2003).

The aim is to find a value of an index, for which the correct forecasts ( $a$  and  $d$ ) are maximized, while the wrong forecasts are minimized ( $b$  and  $c$ ; Tab. 3.2). An example for such verification is shown in Fig. 3.4 for the Lifted Index. Note that the lower this index, the higher is the potential

for thunderstorm occurrence. The threshold is fixed for a value of LI, where the HSS reaches its maximum (here for  $LI = 1$ ), the Probability of Detection (POD; Appendix B) index has relatively high values and the False Alarm Rate (FAR) index is relatively low.

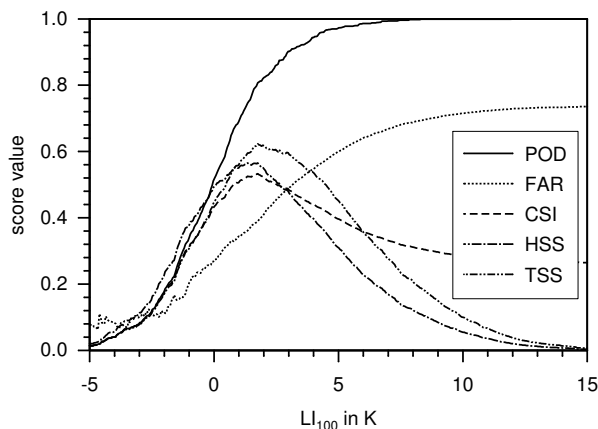


Figure 3.4: Skill scores as a function of the Lifted Index ( $LI_{100}$  = vertical profile averaged over the lowest 100 hPa) according to Kunz (2007a).

### Detection of hailstorm related weather types

Categorical verification is also used to detect weather types that are related to the most common occurrence of hail damage on buildings. It is assumed that a certain weather type was predicted and occurred in conjunction with hail damage (*a*) or without damage (*b*). Weather types with high HSS ( $HSS > 0.04$ ) are considered as hail-related weather types, while those with low HSS ( $HSS < 0.04$ ) are considered as hail-unrelated. Those are categorized into three groups, including a group of those with an HSS of approximately zero. This group is called 'remaining types' and indicates weather types that are only infrequently accompanied by hail.

### 3.3.2 Trend analysis and statistical significance

To detect linear, monotonic trends in the time series of the categorized weather types, the rank based non-parametric Mann-Kendall (MK) statistical test is applied. This test is widely used for the detection of linear trends in hydrological and meteorological time series (Mann, 1945; Kendall, 1975). It computes the probability that the null hypothesis (the sample is independent and identically distributed) can be rejected against the alternative hypothesis that a monotonic trend exists. Advantage of this test is the independence to any specific distribution, such as the normal distribution. In this thesis a trend is defined as significant if the null hypothesis can be rejected on the 80% significance level.

To detect trends in series, each data value is compared to each subsequent data value. The MK statistic  $S$  is computed as (Yue et al., 2002)

$$S = \sum_{i=1}^{n-1} \sum_{j=i+1}^n \text{sgn}(x_j - x_i), \quad (3.10)$$

where  $x_i$  are the sequential data values,  $x_j$  the subsequent values,  $n$  the length of the data set and

$$\text{sgn}(x_j - x_i) = \begin{cases} 1 & \text{if } (x_j - x_i) > 0 \\ 0 & \text{if } (x_j - x_i) = 0 \\ -1 & \text{if } (x_j - x_i) < 0 \end{cases} \quad (3.11)$$

Hence, negative values of  $S$  indicate a decreasing trend and positive ones an increasing trend.

Since  $S$  approximately follows a standard normal distribution for  $n \geq 8$  (Kendall, 1975), the significance is tested by using the mean ( $E(S) = 0$ ) and the variance ( $V(S)$ ):

$$V(S) = \frac{n(n-1)(2n+5) - \sum_{i=1}^n t_i i(i-1)(2i+5)}{18} \quad (3.12)$$

where  $t_i$  is number of tied group (set of sample data with same values),  $i$  the number of values in the corresponding tied group and  $n$  the length of the time series. If, for example, a data set contains the values [1, 2, 3, 2, 2, 3],  $t_i$  is equal two 2, because there are two groups of the same values.

The standardized MK statistic  $Z$ , which follows a standard normal distribution, is computed by:

$$Z = \begin{cases} \frac{S-1}{\sqrt{V(S)}} & \text{if } S > 0 \\ 0 & \text{if } S = 0 \\ \frac{S+1}{\sqrt{V(S)}} & \text{if } S < 0 \end{cases} \quad (3.13)$$

To compute the probability that the null-hypothesis is rejected, a standard normal cumulative distribution function is used

$$P = \frac{1}{\sqrt{2\pi}} \int_{-\infty}^z e^{-t^2/2} dt. \quad (3.14)$$

The probability  $P$  assumes a value of 1 if the time series exhibits a positive trend, a value of 0.0 if a negative trend exists and 0.5 if the sample is without any trend.

### Prewhitening

Any auto-correlation in time series increases the variance of the Mann-Kendall statistic and, consequently, increases the probability of the detection of a significant trend, as shown, for example, by Von Storch and Navarra (1995) and Yue et al. (2002). A positive serial correlation leads to an overestimation of the probability of significant trends, while negative serial correlation (autocorrelation) tends to underestimate the probability of detecting trends. Furthermore, the trend itself has an impact on the Mann-Kendall statistics. If the time series has no trend, there is an incorrect rejection of the null hypothesis, meaning an overestimation of a trend (Type I error). If a trend

exists, there is an incorrect acceptance of the null hypothesis (Type II error; Bayazit and Önöz, 2007). Hence, a data correction method referred to as prewhitening should be applied to the time series prior applying the MK test.

Corresponding to the method introduced by Yue et al. (2002) and improved by Bayazit and Önöz (2007), the time series of the weather types are prewhitened if the number of years is less than 50, if the slope of the trend is less than 0.01 and if the coefficient of variation ( $C_v$ ) is more than 0.1 ( $C_v$  is the relative standard deviation of the time series).

For the prewhitening procedure, the linear trend  $b$

$$b = \text{Median} \left( \frac{x_j - x_l}{j - l} \right) \quad \forall \quad l < j, \quad (3.15)$$

which is a robust estimate for the magnitude of a trend (Theil, 1950; Sen, 1968) is removed and the lag-1 ( $\tau = 0 =$  time shift) correlation coefficient of the detrended series is computed as

$$r(\tau) = \frac{\frac{1}{n-1} \sum_{i=1}^{n-1} (x_i - \bar{x}_i)(x_{i+1} - \bar{x}_i)}{\sqrt{\frac{1}{n} \sum_{i=1}^n (x_i - \bar{x}_i)^2 \sum_{i=1}^{n-\tau} (x_i - \bar{x}_i)^2}}, \quad (3.16)$$

where  $r$  is the rank correlation coefficient,  $x_i$  the detrended time series,  $\bar{x}_i$  the mean of the detrended time series and  $n$  the number of values. This term (3.16) is used to reduce the detrended time series  $x_i$  by the auto regression function, if an autocorrelation exists,

$$y_i = x_i - r_i x_{i-1} \quad (3.17)$$

where  $y_i$  is the resulting, independent time series. The fourth and last step before applying the MK test is to add the identified trend, which was removed at the beginning. The resulting time series is not longer influenced by the effects of autocorrelation, and the significance of the MK test is less erroneous.

### 3.3.3 Frequency analysis

A common method to detect periodicity in time series is spectral analysis. Using a Fourier Transformation (FT), the signal is broken down into its harmonic parts by

$$F(f) = \sum_{n=0}^{N-1} x_n e^{-2\pi i f t} \quad (3.18)$$

with

$$e^{2\pi i f t} = \cos 2\pi f t + i \sin 2\pi f t, \quad (3.19)$$

$N$  for the length of the time series,  $f$  for the sampling frequency and  $t$  for the sampling time. The FT is applicable to any continuous, infinite and periodic time series and able to breakdown the

time series into its harmonic parts up to the Nyquist frequency of

$$f_{Nyquist} = \frac{f}{2}. \quad (3.20)$$

Due to the remarkable computing time for the FT, a Fast Fourier Transformation (FFT) algorithm according to Cooley and Tukey (1965) is applied. The FFT is based on the condition that the FT of each finite time series is, under certain conditions, computable as two consecutive FTs of shorter sequences with the lengths of  $N = M \times K = 2^n$ , where  $M$  and  $K$  are the lengths of the shorter sequences (Von Storch and Zwiers, 2003) and  $n$  a random number. Applying this leads to a significantly shorter computing time.

As the used time series for this thesis are discrete, finite and not harmonic, a spectrum can only be estimated. To minimize the uncertainty of estimation, several steps are applied to the time series prior to the FFT analysis. To avoid the effect of a linear trend on the spectral analysis, each time series is detrended as described in the previous section. Furthermore, the effects of 'spectral leakage'<sup>6</sup> and discontinuities (e.g., phase shifts), are reduced by application of the FFT to the autocorrelation function (ACF) of the time series (Eq. 3.16) instead of the time series itself. Additionally, the ACF is filtered with a 'hamming-window'  $h(i)$  to avoid spectral leakage (Schönwiese, 2000)

$$h(i) = 0.54 - 0.46 \cos\left(\frac{2\pi i}{M}\right) \quad (3.21)$$

for  $0 < i < M$ , with  $M$  for the maximal shift of the ACF (Oppenheim and Schaffer, 1989). The maximum time shift of the ACF is chosen to be the half of the length of each time series to ensure a sufficient long period of examination, but also to avoid the spectrum to become unstable for high  $M$ -values (Schönwiese, 2000). Another effect that can be reduced by applying a window function is 'aliasing'. The finite spacing of the measurements may lead to a misinterpretation of the frequencies, as shown in Fig. 3.5, where the sampled signal indicates a signal with a lower frequency than the original one. To avoid aliasing, a low pass filter needs to be applied, which is also achieved by use of the hamming-window.

### 3.3.4 Probabilistic Forecast of hailstorm events

Application of categorical verification to the classified weather types yields specific weather types that occur most frequently on days with damaging hail events. However, this method cannot give an appropriate estimate about the uncertainty, with which hailstorms occur during a certain weather pattern. Hence, a statistical model is used to quantify uncertainty and to predict the future number of hail days.

The requirements of the model are:

---

<sup>6</sup>Due to the finiteness of the time series and the corresponding cutting off of harmonic periods, the discrete time spectrum appears as a smeared version of a continuous spectrum, since energy of the cutoff signal 'leaks' into neighboring frequencies (Schönwiese, 2000).

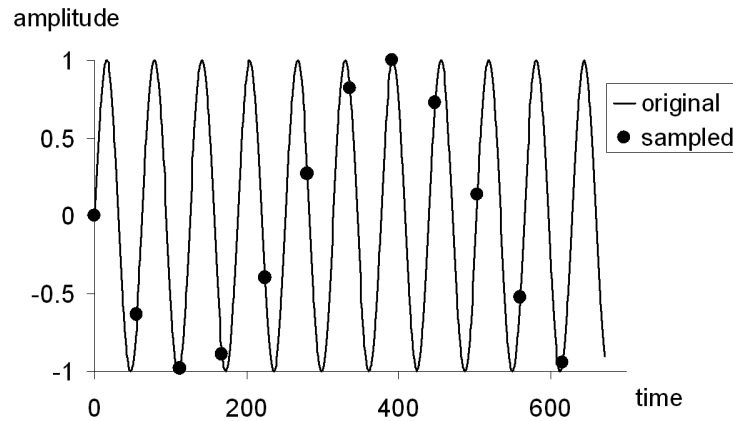


Figure 3.5: Amplitude of a signal vs. time. The black line shows the original signal, while the back circles indicate the sampled data. Aliasing occurs when the sampling frequency is too low with respect to the frequency content in the original time series (<http://www.cbi.dongnocchi.it/glossary/Aliasing.html>).

- the model must be able to deal with a small sample size since hailstorms are rare events (222 hail days out of 2745 days in this study);
- it needs to take weather types into account that never occurred along with a hailstorm in the past;
- it must be able to dismiss weather types that never occurred at all.

### Model description

The chosen model is a binomial distribution (Vitolo and Economou, 2011, not published) defined by

$$Prob(H_i|p_i) = Bin(N_i, p_i) = \binom{N_i}{H_i} p_i^{H_i} (1 - p_i)^{N_i - H_i} \quad i = 1, \dots, 38 \quad (3.22)$$

$$p_i \sim Beta(\alpha, \beta) = \left[ \frac{\Gamma(\alpha + \beta)}{\Gamma(\alpha)\Gamma(\beta)} \right] p^{\alpha-1} (1 - p)^{\beta-1} \quad \alpha, \beta > 0 \quad (3.23)$$

with  $N_i$  for the total number of days where weather type  $i$  occurred,  $H_i$  as the number of hail damage days that occurred during the weather type  $i$  and  $p_i$  as the probability with which hail damage does occur during the weather type  $i$ .  $\Gamma$  is the gamma function (Wilks, 1995). Thus, the  $Prob(H_i|p_i)$  is the statistical distribution of the number of hail damage days according to the statistical probability  $p_i$ . While  $N_i$  is known for every weather type, the probability  $p_i$  with which hail damage days occurred during a certain weather types is unknown. Hence, statistical methods are used to estimate a value for  $p_i$  for each weather type and, thus, to use the model to predict the number of hail damage days in the climate models.

The method used to fit the model is Bayesian: A Beta-distribution (Eq. 3.23) is used to model the probabilities with which hail damage days occurred during the different weather patterns. The Beta-distribution has the advantage that it ranges between  $[0,1]$ . The method of Markov chain Monte Carlo (MCMC; Wilks, 1938) is used to estimate the distribution of the parameters  $\alpha$  and  $\beta$  and hence each  $p_i$ . The Monte Carlo technique allows to approximate properties of a probability distribution by drawing independently identically distributed samples  $X_1, X_2, \dots, X_n$ . The sample mean is an approximation for the original expectation (here  $p_i$ ). The used MCMC method is similar, with the only difference that the samples are not independent. They are dependent and generated by a Markov chain.

## 4. Validation and detection of hail-related weather types

To identify specific weather types (WTs) that are associated with a higher frequency of hailstorm damage, the simulation results of the CCLM-ERA40 model were used. Because these model runs were initialized by ERA40 reanalysis data, the results can be evaluated with the original ERA40 and ERA-Interim and with the WTs operationally determined by DWD. After evaluating the weather patterns derived from the CCLM-ERA40 data hail-related WTs will be identified and discussed. Subsequently, differences between the WTs derived by the different climate models will be discussed. Furthermore, a modified WT classification scheme that gives a better correlation between hailstorm occurrence and WTs is introduced and evaluated.

### 4.1 Validation of CLM-ERA40 derived weather types

First, to what extent the spatial resolution of the models modifies the weather patterns determined by the oWLK method is evaluated. For this purpose, the WTs derived from the CCLM-ERA40 with a horizontal resolution of  $0.44^\circ$  are compared with those obtained from the ERA40 reanalysis with a resolution of approximately  $2.5^\circ$  (Fig. 4.1). The total number of days at which the corresponding WT prevailed in the years 1971 to 2000 (April to September) is shown (red: ERA40; blue: CLM-ERA40) in Fig. 4.1. It is evident that the distributions are very similar, showing that WTs with general flow directions from NW and SW or indifferent direction (XX) occur more often than WTs with NE or SE flow directions. Of course, this fact can be related to the main flow direction in the west-wind zone of Central Europe with prevailing westerly winds. Additionally, WTs with negative vorticity in the lower troposphere (in 1000 hPa) prevail more often than others.

Both data sets show similar overall distributions, even if large relative deviations between them are found (right panel of Fig. 4.1). The bars indicate the relative deviation of the number of days of each particular WT derived from CCLM-ERA40 and normalized by that obtained from ERA40. Apparently, WTs with northerly advection types are overestimated by CCLM-ERA40, while southerly types are underestimated. Nevertheless, the over-/underestimation is mostly less than 50%, or even less than 25% in most of the cases. Higher differences occurred only in cases of rare WTs (e.g., NWCAW, NWCCD, NWCCW, SWCCD).

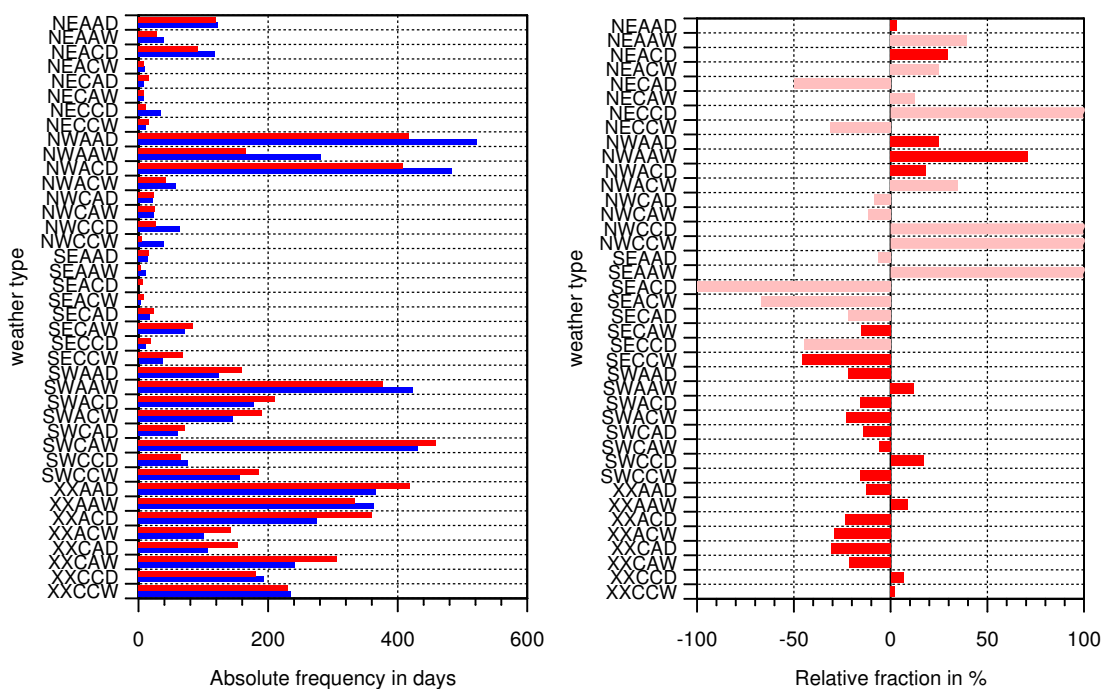


Figure 4.1: Left: Number of days WTs prevailed during the summer months from April to September between 1971 and 2000 derived from ERA40 reanalysis (red) and from CCLM-ERA40 (blue). Right: deviation of WTs derived from CCLM-ERA40 and ERA40; light red bars indicate weather patterns that occurred less than 50 days in the whole period.

The reasons behind that differences are further investigated by deriving histograms of the particular parameters considered in the classification method (Fig. 4.2). NW and NE advection types occur more often in the data of the CCLM-ERA40 model, but are still within an accuracy level of 8% compared to the ERA40. Accordingly, other advection types occur less frequently in both models. As evident from Fig. 4.1, all WTs with positive vorticity in 1000 hPa are overestimated by the CCLM-ERA40 model. This cannot be explained by the distribution of the cyclonality. However, within scope of this thesis, it will be shown that the differences in cyclonality and also in other parameters can often be explained by specific cases, where the accumulated parameter is very sensitive to a slight shift, for example, when the vorticity is near zero. In this case, the spatial resolution of the models may modify the results due to the matching in a dichotomous scheme.

The distribution of the humidity in terms of precipitable water (PW) shows major differences particularly at higher values between the two data sets. In general, CCLM-ERA40 has a higher PW content than ERA40. This effect, however, is mitigated to a large extent because the actual PW values are normalized by the model climatology in the oWLK scheme. On the other hand, the annual cycle of PW agrees well with both models.

According to these analysis, the differences in the classification of the flow direction are largest. Hence, these cause the main deviations in the frequency of the WTs between the RCM realizations, as shown in Fig. 4.1.

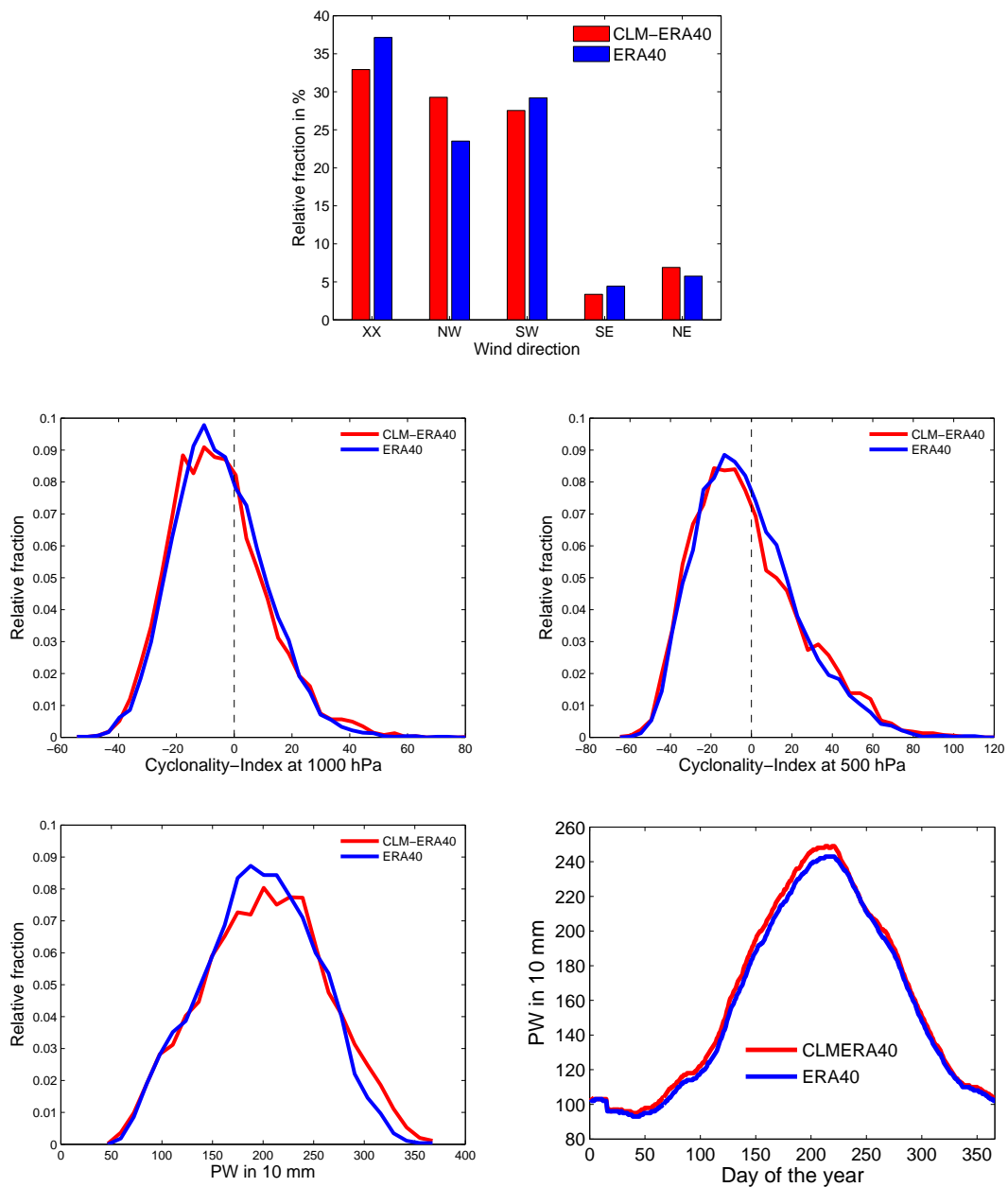


Figure 4.2: Relative distribution of the parameters used for weather type classification as derived from CCLM-ERA40 (red) and ERA40 (blue) in the same period as Fig. 4.1. Top: wind direction, middle: vorticity in 1000 (left) and in 500 hPa (right), bottom: precipitable water content (PW; left) and daily mean of precipitable water content vs. the day of the year (right).

### Identification of hail-related weather types

As the overall distribution of WT<sub>s</sub> determined from CCLM-ERA40 data shows a good agreement to that derived from ERA40 reanalyses, only the WT<sub>s</sub> derived from CCLM-ERA40 were used to relate them to hailstorm occurrence. This is done by comparing them with hail days as determined from the SV data for the federal state of Baden-Württemberg.

First, the fractional occurrence of hailstorms per WT is discussed, as this analysis identifies the

strength and weaknesses related to the application of the oWLK to different data sets. It also gives information on the validation of the CCLM-ERA40 data set. Additionally, it explains why categorical verification is applied.

According to the fraction of hail-days on each WT and the number of days this WT occurred during the whole observational period of the SV (referring to the months April to September from 1986 to 2000), five of the 40 WTs can be considered as the most hail-related WTs (Fig. 4.3). With a frequency of over 15%, the types SWCCW, SWCAW, SECAD, SWAAW and XXCAW are related to hail (Fig. 4.3, right). This conforms well with findings of Bissolli et al. (2007), who found a relationship between three of those WTs and tornadoes in Germany. This is not surprising since tornadoes often accompany thunderstorms, as does hail. Likewise WTs that are only very infrequent accompanied by hail can be detected. For example, the WTs NWAAW, XXAAD, NWAAD and NWACD all prevail more than 150 days within the whole period but are only 2% of the days accompanied by hail damage.

The reasons the five mentioned WTs are forcing the development of hailstorms can be explained by the general atmospheric conditions necessary for thunderstorm development. As discussed in Section 2.4 the triggering mechanisms for thunderstorm development are insolation, synoptic scale ascent in front of a trough, forced ascent due to overflow over mountains, uplift on frontal zones or convergence zones. With the oWLK just the meso-scale mechanisms can be captured.

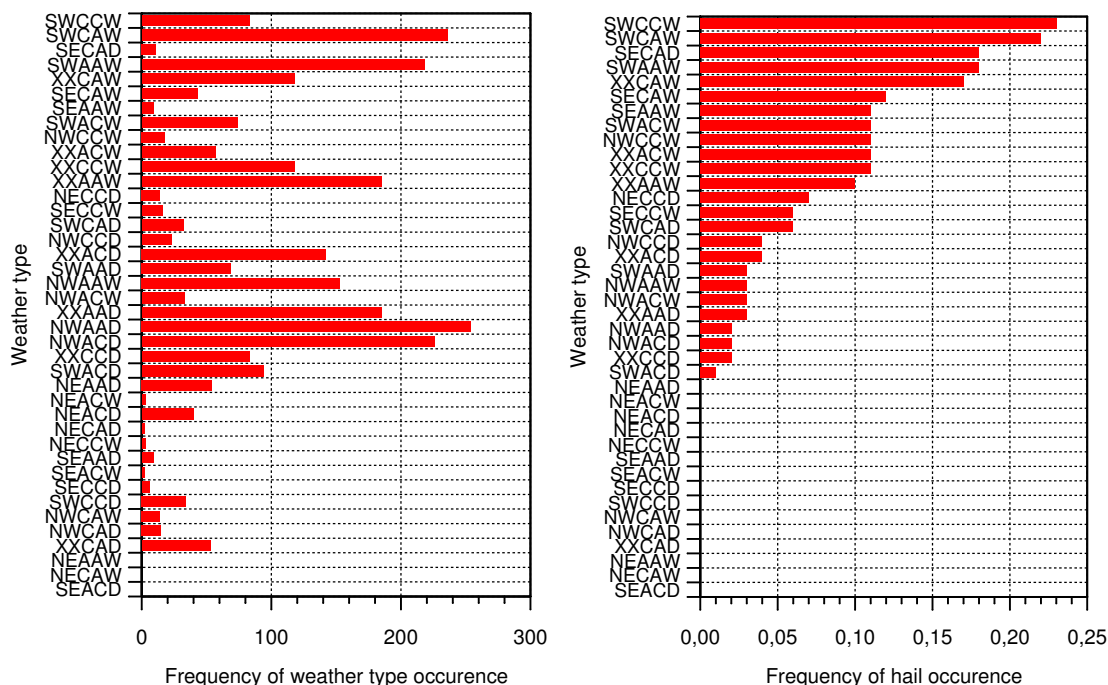


Figure 4.3: Number of days each WT occurred (left) and the probability of damage causing hailstorms to occur during each WT (right) according to the CCLM-ERA40 data.

Of additional importance and indirectly coupled with those properties, is the stability of the atmosphere and the amount of water in the lower troposphere. Hence, all the WTs are most likely linked to those properties.

Three of the five WTs that have a high fraction of occurrence along with hailstorms feature SW advection, and one of them an indifferent advection type, which could possibly include southwesterly features as well. However, advection of an air-mass from SW mainly implies the transport of moist and warm air from the Mediterranean or, through France from the Atlantic. High temperatures increase the probability of the surface temperature to overcome the convective temperature necessary for thermal convection. Furthermore, the high moisture content of the air-mass allows the formation of heavy rain and hail.

The general flow direction is mainly determined by large-scale pressure systems. Those are already captured by the cyclonality index in the oWLK. Three of the five patterns are characterized by cyclonality at the 1000 hPa level and anticyclonality at 500 hPa, which indicates that those conditions favor thunderstorm development. A typical condition favoring thunderstorms in summer is a slow eastwards moving upper air ridge, followed by a low pressure system from the west. First the pressure drops close to the surface, inducing convergence leading to large-scale lifting and, hence, thunderstorm development. This constellation is also known as 'Spanish Plume', introduced by Morris (1986).

On the other hand, the frequent occurrence of the patterns SWAAW and SWCCW on hail damage days indicates that the cyclonality is not as important as the general flow direction and the humidity. For example, the WT SWAAW prevailed on 218 days (out of 2,745 days in total) and with 18% of those days came damage causing hailstorms. To answer the question of whether the cyclonality has an influence on hail damage occurrence and to identify typical hailstorm conditions with regard to the cyclonality, the geopotential fields (cyclonality) of WTs that are related to hailstorms are shown in Figures 4.4 - 4.6.

For the mean patterns of SWCAW (Fig. 4.4) and SWAAW (Fig. 4.5) the averaged geopotential fields in 500 hPa are almost similar, differing by a geopotential difference of about 4 gpdm. The standard deviation indicates that there is just a slight change in the location of the high pressure ridge southwest of Germany. For the SWCCW (Fig. 4.6) pattern, the upper-air trough is closer to Germany (lower values of the geopotential) and affects the largest part of the area, leading into a positive cyclonality index. It is remarkable that for this case the standard deviation west of the area is highest with 10 gpdm. This is most likely due to the meridional extension of the trough. For the patterns SWCAW and SWCCW it is evident that the upper air ridge, located southwest of Germany, is followed by a low pressure system in the lower layers. This confirms the hypothesis of the 'Spanish Plume' and explains why thunderstorms tend to occur during these conditions. This is also valid for the WT XXCAW (Fig. 4.7), where the upper air ridge is still located with its center over Germany and the 1000 hPa trough has a location west of the area. This is an indication that these three WTs, even if classified as different WTs, are a result of the same setting of the synoptic systems just at different points in time. However, the theory of the 'Spanish Plume' is

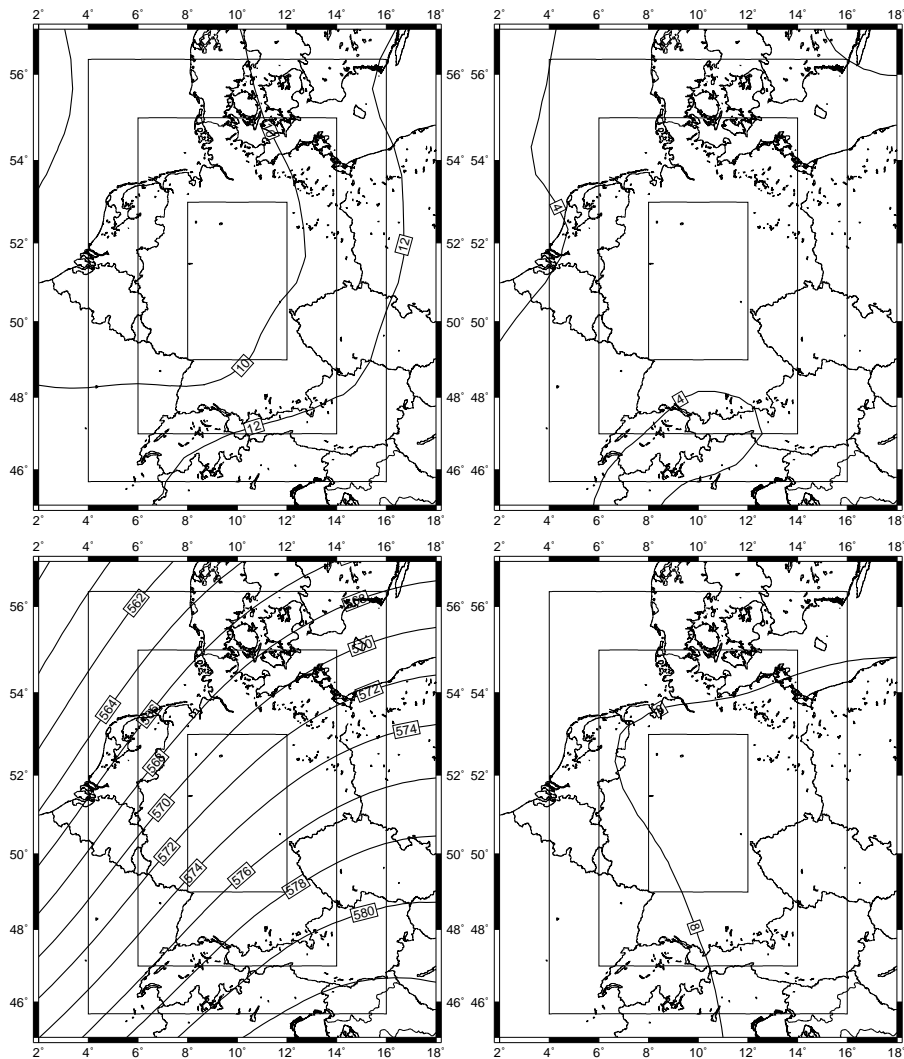


Figure 4.4: Mean geopotential fields in gpm (left) in 1000 (top) and 500 hPa (bottom) with standard deviation (right) on all days the WT SWCAW prevailed and hail occurred.

not valid for the SWAAW condition. Here, a high pressure system at 1000 hPa is located over the European Alps as shown in the mean fields in Fig. 4.5. Hail damage occurred on 39 days when this WT prevailed ( $\approx 17\%$ ).

### Case study - SECAD

The last hailstorm favoring WT according to Fig. 4.3 is the WT SECAD. For this WT hail damage has a probability of 18% to occur together with this WT. Physically, with a dry atmosphere and advection of south-easterly air masses (continental, not extraordinary warm or moist) hailstorm development would not be forced by this WT. However, the high probability is limited by the total number of occurrence for this type. It prevailed for just eleven days in total and for just two days together with hail damage claims. Furthermore, those two days occurred within a time period of three days and were forced by a long-lasting high pressure system over Iceland (Fig. 4.8). The

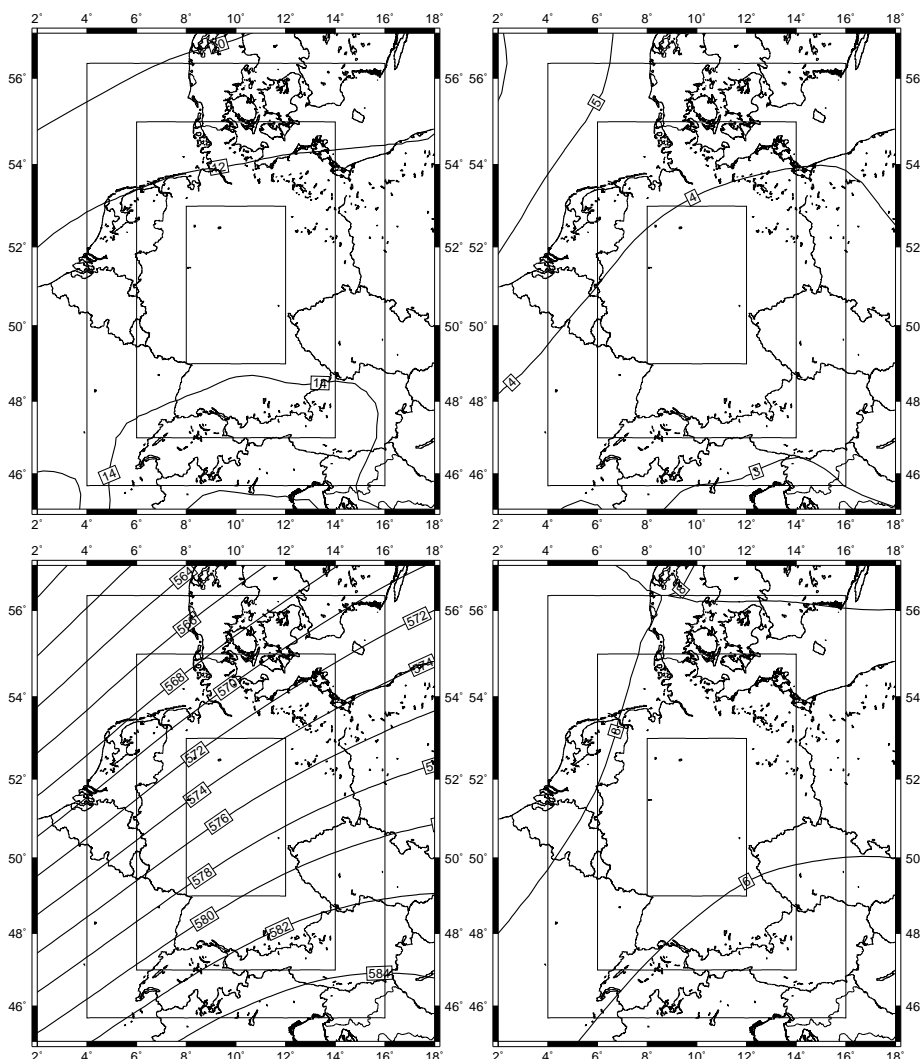


Figure 4.5: Same as Fig. 4.4 but for the SWAAW pattern.

weather on May 10 1993 was dominated by high pressure, with its center southeast of Iceland and low pressure over the Azores. The high pressure predominant in various vertical layers extended over the south and middle of Scandinavia through the west of Russia. Germany was located between those two pressure systems with easterly to southeasterly flow directions. According to CCLM-ERA40, the vorticity at 1000 hPa (12 UTC) indicated a cyclonic behaviour (Table 4.1), while at the 500 hPa height indifferent conditions prevailed. Slightly different values of the vorticity between ERA40 and CLM-ERA40 lead to different values for the cyclonality index, which is important for the WT classification. Hence, the reanalysis data show a cyclonic rotation, while the CCLM-ERA40 data result in anticyclonic behavior. The magnitude of the values, however, indicate (ERA-Interim: 0.9 at 500 hPa) that during this day a slightly different constellation on the location would lead to another WT. This indicates that the WT classification may lead to differences between data sets. Similarly, consideration of humidity may lead to similar results. For example, on May 10, PW in the CLM-ERA40 was 16.4 mm and only marginally lower compared to the 10-day running climatological average (16.6 mm).

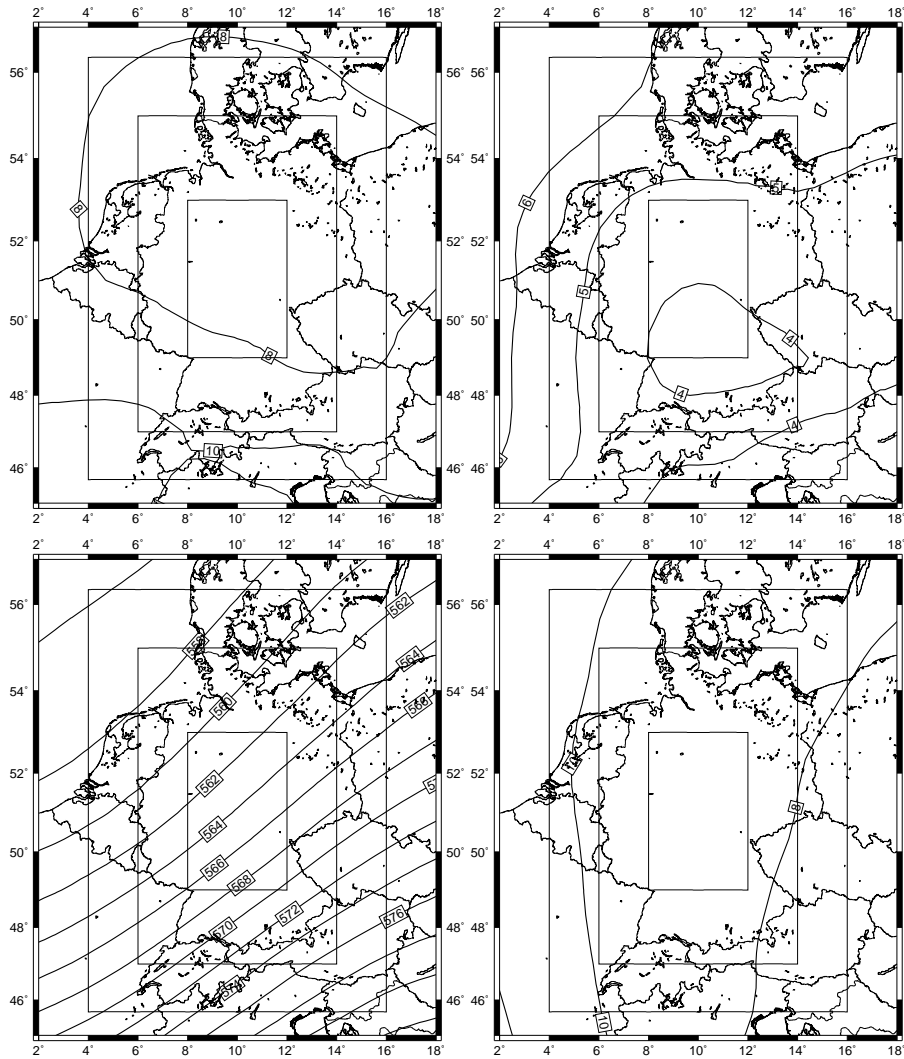


Figure 4.6: Same as Fig. 4.4 but for the SWCCW pattern.

Table 4.1: Parameters of the oWLK on May 10 (upper part) and May 12, 1993 (12 UTC) according to the ECMWF reanalysis and CLM-ERA40 model data. PW (mean) is the climatological mean of the precipitable water on that day of the year.

Day of year	Model	oWLK	Cyc. Ind. 1000 hPa	Cyc. Ind. 500 hPa	PW in mm	PW (mean) in mm
May 10	CLM-ERA40	SECAD	9.6	-5.0	16.4	16.6
	ERA40	SECCW	20.0	3.1	18.3	16.0
	ERA-Interim	SECCW	19.3	0.9	19.0	16.4
May 12	CLM-ERA40	SECAD	10.5	-7.9	14.2	16.9
	ERA40	SECCW	24.6	1.8	18.6	16.3
	ERA-Interim	SECCW	26.6	0.7	19.0	16.6

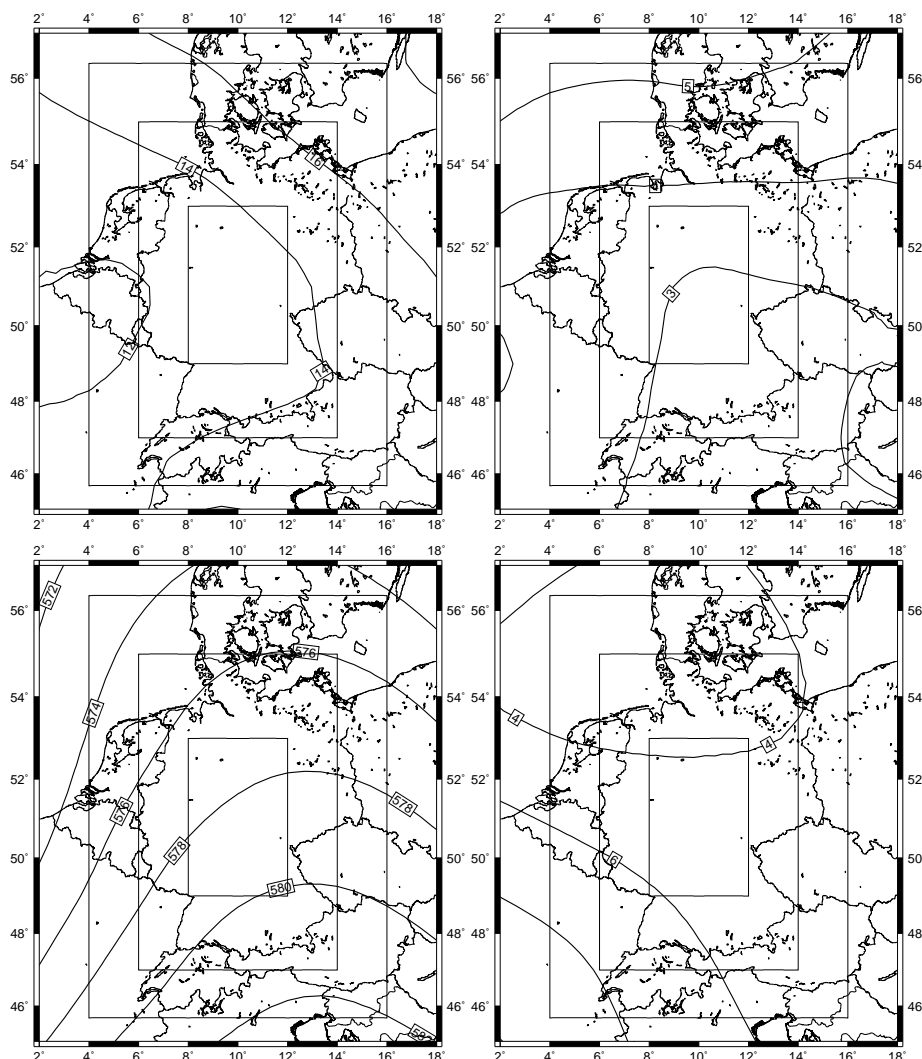


Figure 4.7: Same as Fig. 4.4 but for the XXCAW pattern.

### Categorical verification

These examples illustrate the strength, but also the limits of the WT classification scheme with regard to the predictability of hail days, especially at indifferent weather conditions. It also explains the differences in the distribution of the WTs (Fig. 4.1), but does not allow an assessment about which of the data sets is more reliable.

Hence, categorical verification is used, as this method considers the number of days where each weather pattern occurred during the whole time period. In the following analysis, the weather patterns with the highest skill to detect/predict the occurrence of damage causing hailstorms according to the SV data are identified over a reference period from 1986 to 2000 according to the HSS introduced in Paragraph 3.3.1. The highest HSS ( $HSS \geq 0.04$ ) with values up to 0.162 is found for the weather types SWCAW, SWAAW, SWCCW and XXCAW, which are referred to as hail-related WTs in the following discussion. Based on the same approach, 'non-events' in terms of

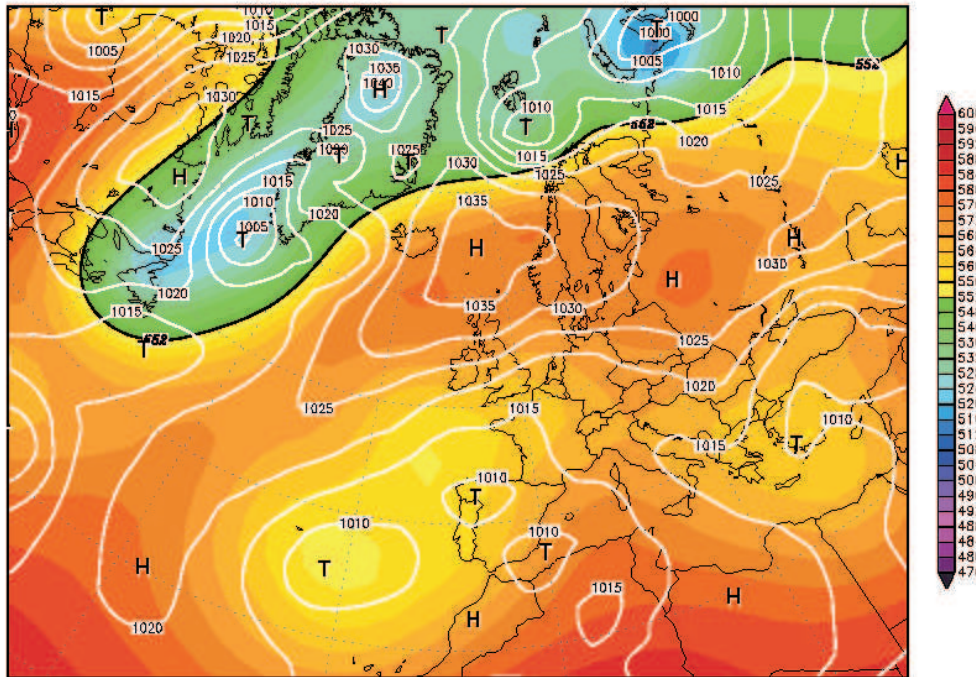


Figure 4.8: NCEP reanalysis of the geopotential at 500 hPa in gpm and surface pressure in hPa for May 15, 1993 (<http://www.wetterzentrale.de>).

Table 4.2: Skill scores of hailstorm-related and hailstorm-unrelated weather types, determined from the CLM-ERA40 and SV data between 1986 and 2000.

	Weather type	POD	FAR	CSI	HSS	a	b	c	d
Hailstorm-related	SWCAW	0.239	0.775	0.131	0.162	53	183	169	2340
	SWAAW	0.176	0.821	0.097	0.106	39	179	183	2344
	SWCCW	0.086	0.771	0.066	0.084	19	64	203	2459
	XXCAW	0.090	0.831	0.062	0.065	20	98	202	2425
Hailstorm-unrelated	SWACD	0.005	0.989	0.003	-0.044	1	93	221	2430
	NWAAW	0.018	0.974	0.011	-0.048	4	149	218	2374
	NWAAD	0.023	0.980	0.011	-0.071	5	249	217	2274
	NWACD	0.023	0.978	0.011	-0.065	5	221	217	2302
	XXAAD	0.023	0.973	0.012	-0.053	5	180	217	2343

specific weather patterns with no hail damage are determined. Lowest skill scores ( $HSS \leq -0.04$ ) are found for the weather types SWACD, NWAAW, NWAAD, NWACD and XXAAD, referred to hereinafter as hail-unrelated WTs (HIWT; see Table 4.2).

In order to determine to what extent the long-term variability of hailstorm-related WTs of the reference model CCLM-ERA40 corresponds with the ECMWF reanalysis data, the relative fraction of hailstorm-related weather patterns of each year are compared (Fig. 4.9). Deviations between the relative fraction of WTs derived by CCLM-ERA40 and ERA40 amount to values between 0%

(e.g., in 1994 and 1997) and 19% (1983), but mostly remain in the range of less than 5%. For some exceptions, the overall variability is reproduced well by the different data sets. Even the low number of hail-related WTs in 1984 is reproduced by all models. To account for the uncertainty of ERA40, which is known to have uncertainties in some of the atmospheric parameters (precipitation and humidity according to Simmons et al., 2007), WTs operationally determined by the DWD (GME) and by ERA-Interim reanalyses are additionally displayed. The data sets confirm that the CCLM-ERA40 model can be considered a reliable reference model with regard to the analysis of long-term variability of the WTs.

Similar statements can be deduced for hailstorm-unrelated WTs (Fig. 4.10), even if the deviation between the different data sets is larger. In some years, the difference of the relative fraction of hailstorm-unrelated WTs amounts to up to 10%, and is therefore higher than for hail-related WTs. This is due to the more frequent occurrence of those WTs (on average, 61 days of the summer half-year according to CCLM-ERA40) compared to the hail-related types (on average, 42 days of the summer half-year). Hence, even higher deviations are found for the remaining WTs, which occurred during the remaining days (80 days per summer half-year). Nevertheless, a good correlation between ERA40 and CCLM-ERA40 was found (Fig. 4.11). Noticeable are the greater deviations between the DWD data and the others between 1980 and 1988. This might result from the use of the BKF model in these years until 1991, which had a coarse spatial horizontal resolution of 254 km. Furthermore, the erroneous classification of the advection type and the consideration of different pressure levels, which were discussed in Paragraph 3.2.2, might lead to those differences.

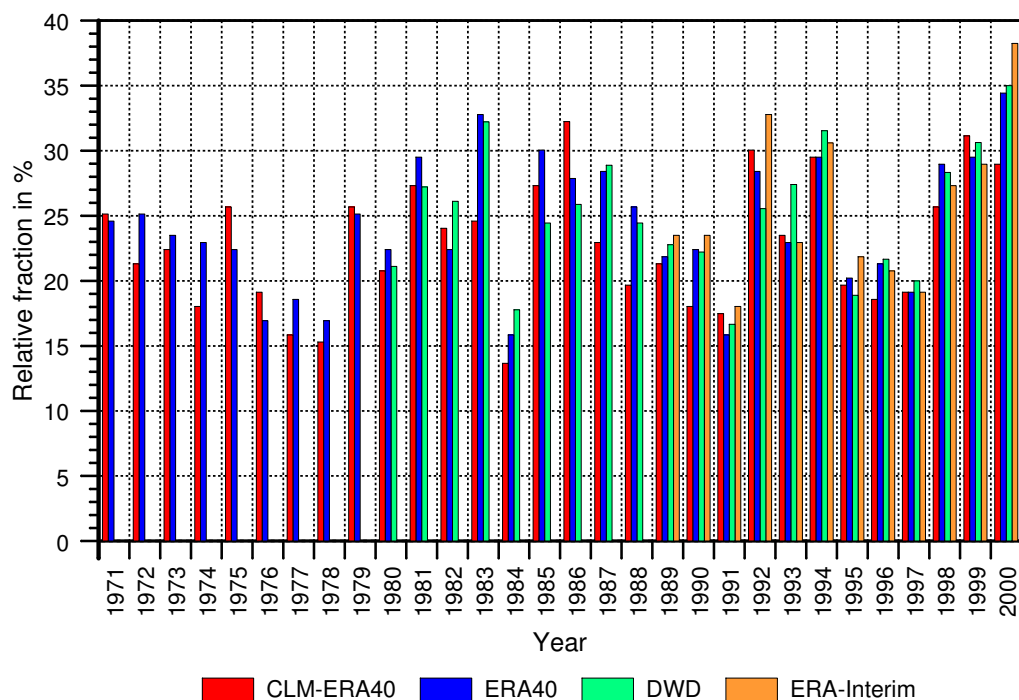


Figure 4.9: Relative fraction of hailstorm-related WTs per year determined from the CCLM-ERA40 data (red), ERA40 reanalysis (blue), ERA-Interim reanalysis (orange) and DWD (green).

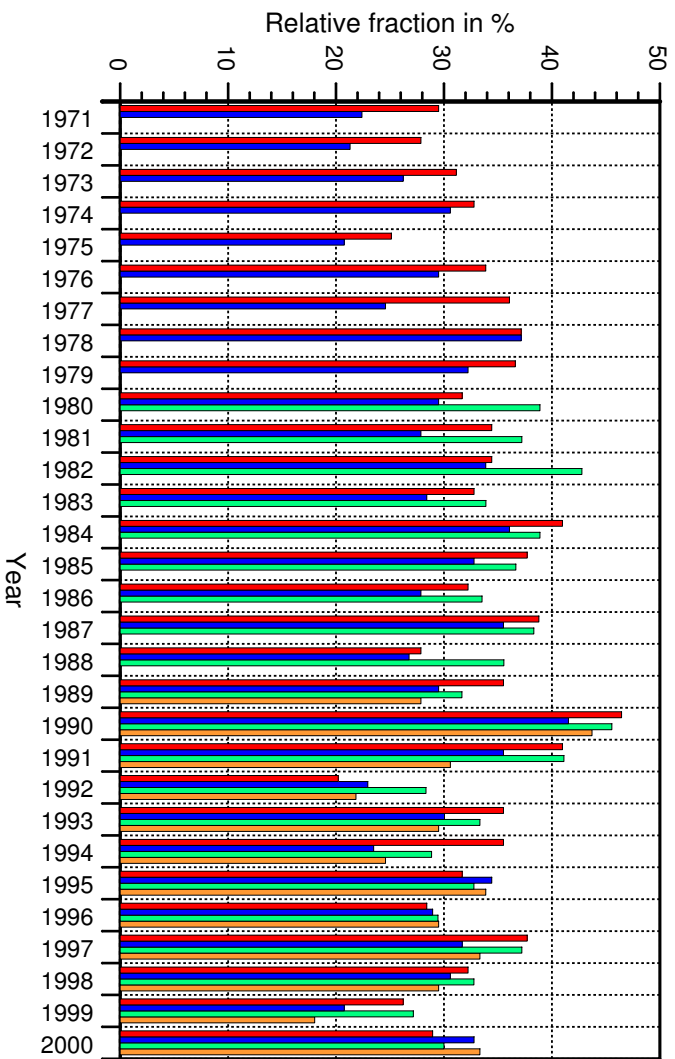


Figure 4.10: Same as Fig. 4.9, but for hailstorm-unrelated weather types.

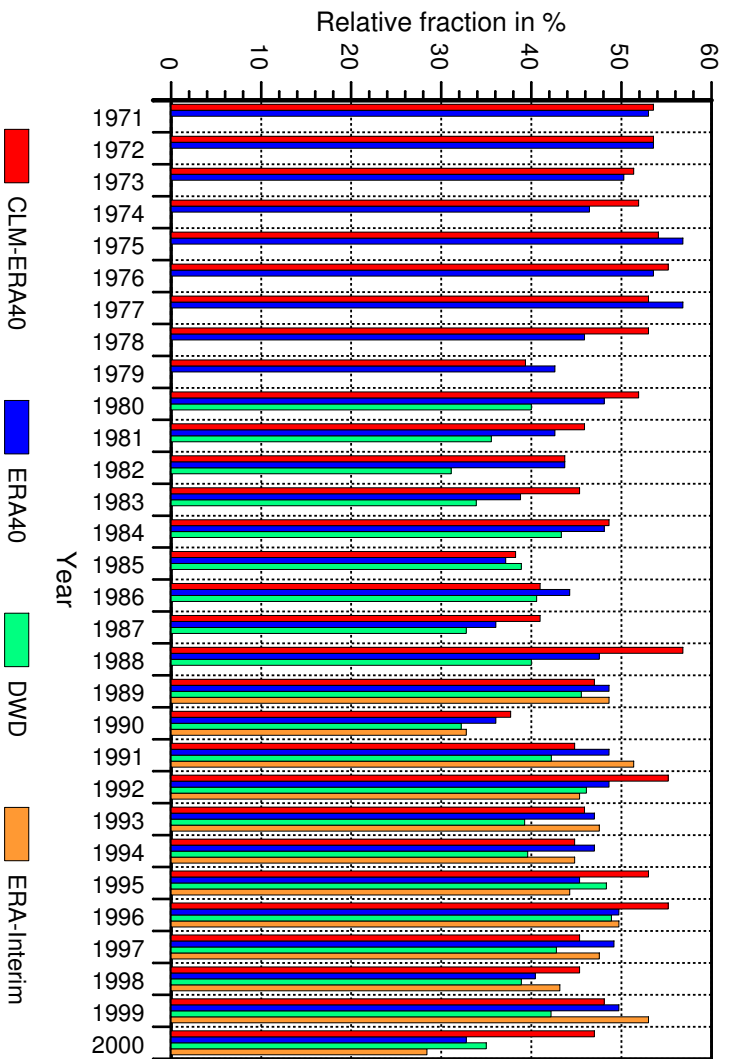


Figure 4.11: Same as Fig. 4.9 and Fig. 4.9, but for the remaining weather types.

## 4.2 Validation of the regional climate model realizations

Reliable reproduction of synoptic weather patterns by climate models is limited, since they are not driven by real weather data. Most climate models are able to reproduce the statistical distribution of various meteorological variables over an adequate long time-period, but cannot reproduce the temporal course of the synoptic fields, for example, on an annual basis. Hence, the validation of the WTs determined from the different climate models is limited to the comparison of the distributions of the weather patterns and their occurrence during the entire control period C20 (1971-2000).

Comparing the three CCLM runs driven by ECHAM5 and calculated by KIT (CE5C20 run 1-3; cf. Table 3.1) with the CCLM-ERA40 (Fig. 4.12) shows very good agreement between the modeled distributions of the WTs. The distributions show minor differences, even if the relative deviations for WTs that occur more than 50 times in the summer months range between 0% and approximately 100%. The 100% deviation is valid only for the weather type NWCCD, which seems to be an exception. While WTs with flow directions from NE or no clearly defined direction seem to be underestimated by all three runs, the other flow direction cannot be clearly considered as over- or underestimated (Fig. 4.13). By evaluating the distributions of the vorticity at both levels and the PW index (Fig. 4.16), the vorticity in 500 hPa might be overestimated by all three RCM runs, which would lead to less cyclonal WTs. This could be the case for the WTs NWACD, NWCCD and SWCCW, where the three CE5C20 runs overestimate the types. Accordingly, the type NWAAD is underestimated, while there is no evidence of an underestimation of the types NWCAD or SWCAW. The distributions for the PW index are conform and show just minor differences.

Same comparison were performed for the CCLM consortium runs (CKLC20R1-R3; cf. Table 3.1) and the CCLM run driven by the GCM of the Canadian Center for Climate Modeling and Analysis (CC3C20R1; Fig. 4.14). These climate model scenarios achieve a similar good correspondence to the CCLM-ERA40, but the CC3C20R1 shows the largest deviations. For WTs occurring more than 50 times, the CC3C20R1 run clearly overestimates the northerly WTs up to 110%, for WTs occurring more than 50 times, but underestimate the southerly types. The CKLC20R1 run shows reverse patterns, but less deviations. For the second run of the CCLM-KL model, the variations are less distinct and within a range of 25%. Additionally, the CCLM-KL runs underestimate the humidity of the south-westerly WTs (especially Run 1). Considering the distributions of the WTs parameters, larger deviations between CCLM-ERA40 and the CCLM-KL runs can be recognized (Fig. 4.17). The vorticity in 500 hPa shows larger deviations between the different model runs, especially in the range between anticyclonic and cyclonic. This indicates that a higher potential for differences of the determined WTs exists. Furthermore, the humidity distributions substantially differ as well. CKLC20R2 and CC3C20R1 are dryer than the other models. But as the PW is normalized by the long-term mean, this parameter is less sensitive against model characteristics.

In summary, all climate models reflect the overall distribution of the WTs well, while CC3C20R1 shows the largest differences compared to CCLM-ERA40. This implicates that deviations are mainly caused by the different forcing GCMs (ECHAM5, CCCma3). However, the distribution of WTs that occur rarely and those occurring frequently is especially reproduced well by all models. Nevertheless, the under- or overestimation of certain WTs of different model runs has to be considered with regard to the interpretation of the long-term variability. A summary is given in Table 4.3.

Table 4.3: Summary of the validation for the WTs derived from different RCM realizations. Over- or underestimations are considered due to the comparison with the WTs derived by CCLM-ERA40.

Model realization	Advection type	Cyclonality 1000 hPa	Cyclonality 500 hPa
CCLM-ECHAM5 (Run 1, 2 and 3)	NE, XX underestimated	-	slightly overestimated
CCLM-KL (Run 1 and Run 2)	NW, SW overestimated	-	slightly overestimated
CCLM-CCma3	SE, SW underestimated	-	overestimated

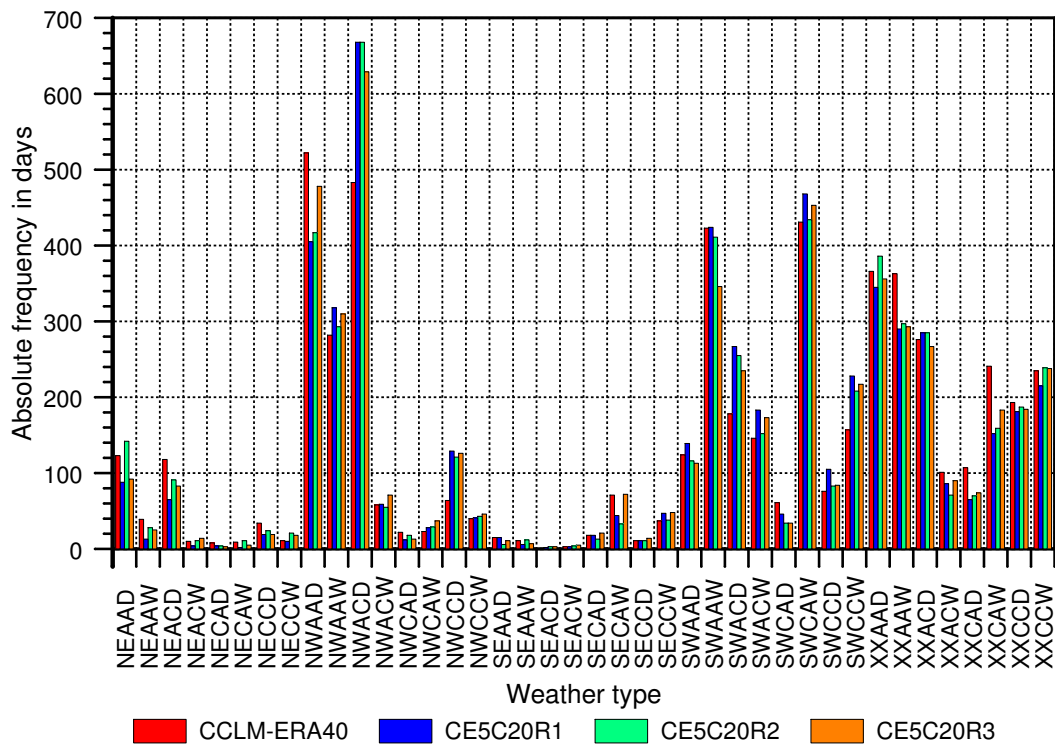


Figure 4.12: WT distribution derived from CCLM-ERA40 and CE5C20R1 (blue), CE520CR2 (green) and CE5C20R3 (orange) during the hailstorm season (April to September).

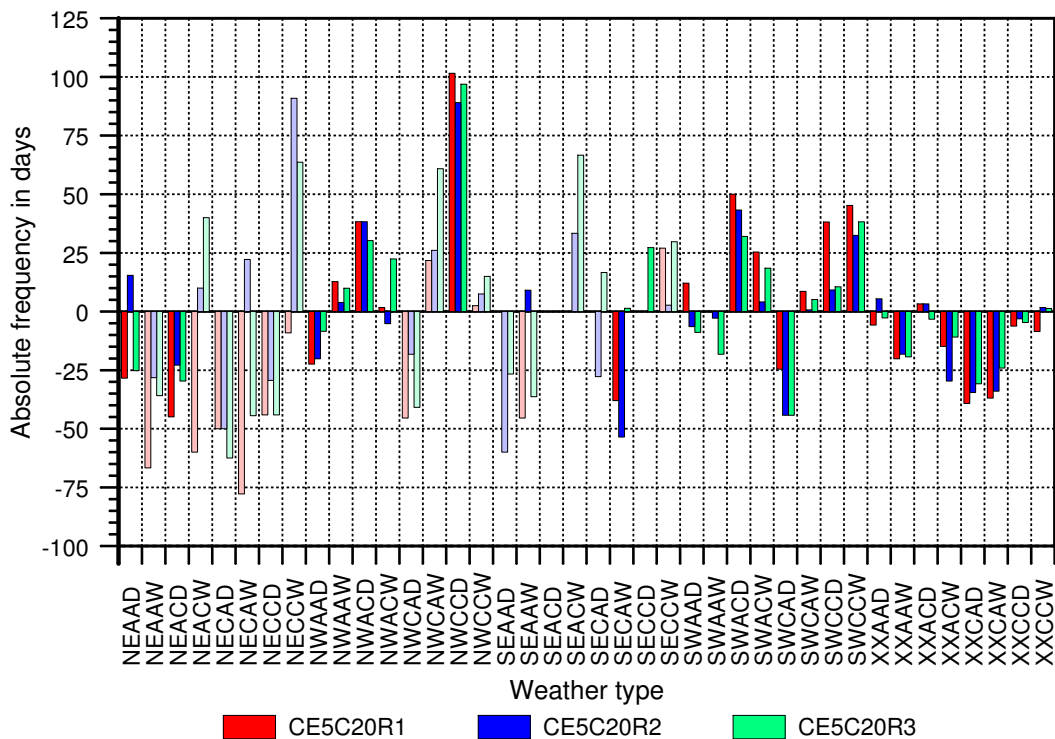


Figure 4.13: Deviation of the WTs determined from CE5C20 model runs R1, R2 and R3 in relation to the reference model CCLM-ERA40. Light colors indicate WTs that occurred less than 50 times during the observation period.

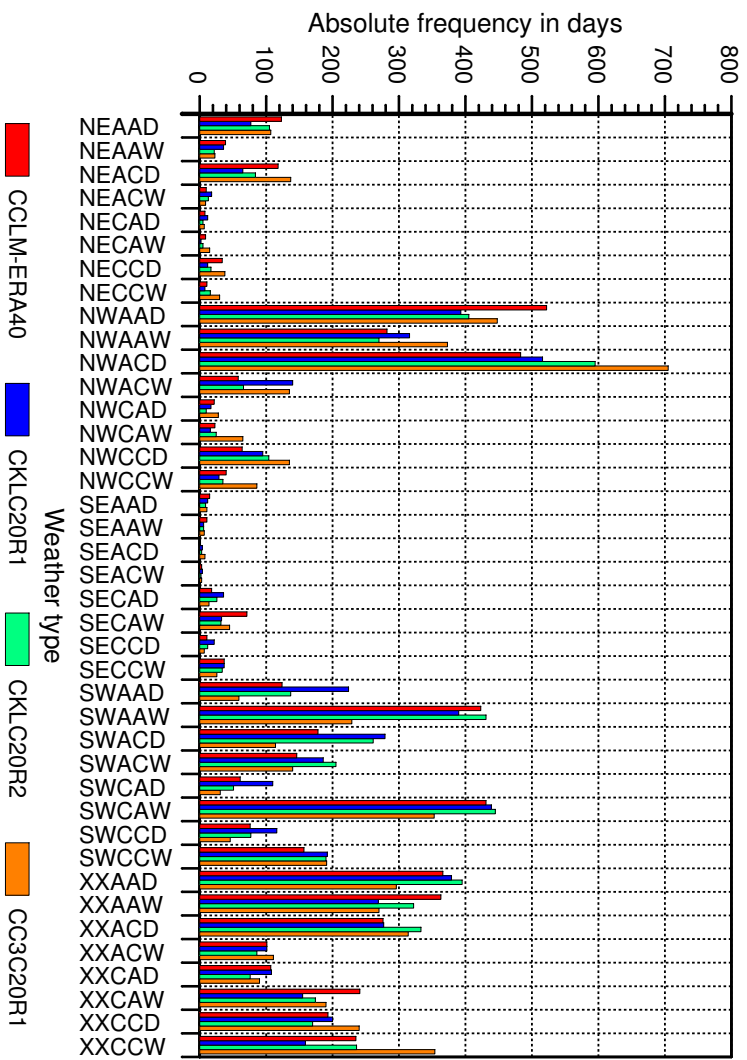


Figure 4.14: Same as Fig. 4.12 but for the CCLM-ERA40 (red), CKLC20R1 (blue), CKLC20R2 (green) and CC3C20R1 (orange) model runs.

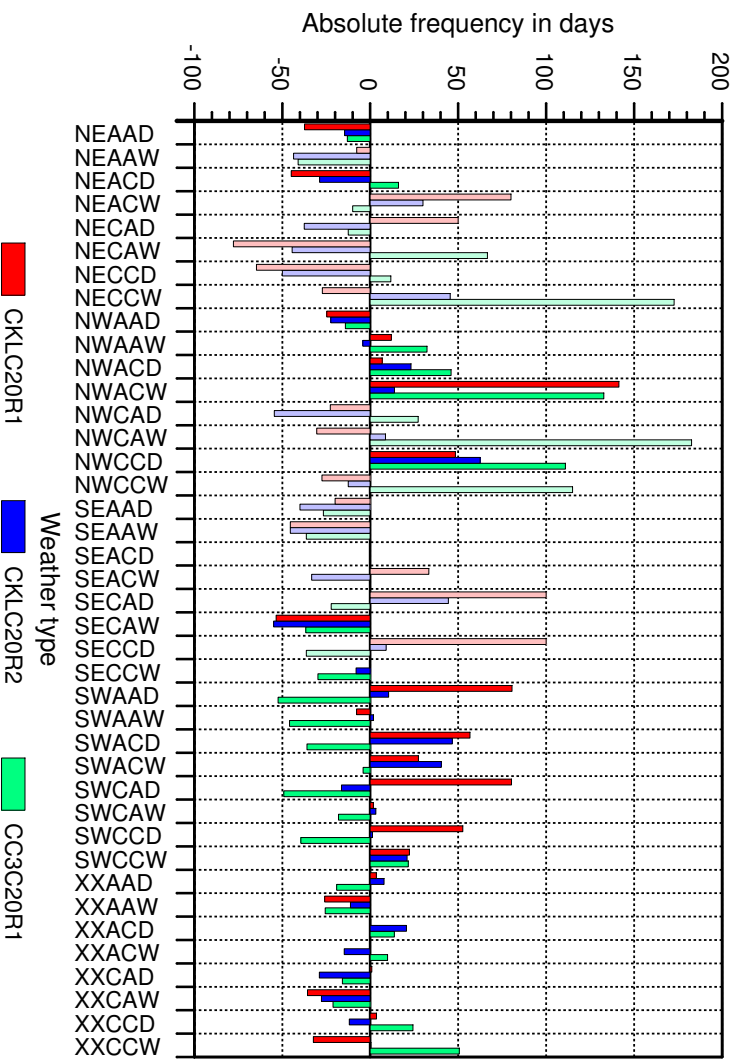


Figure 4.15: Same as Fig. 4.13 but for the CKLC20R1 (blue), CKLC20R2 (green) and CC3C20R1 (orange) model runs.

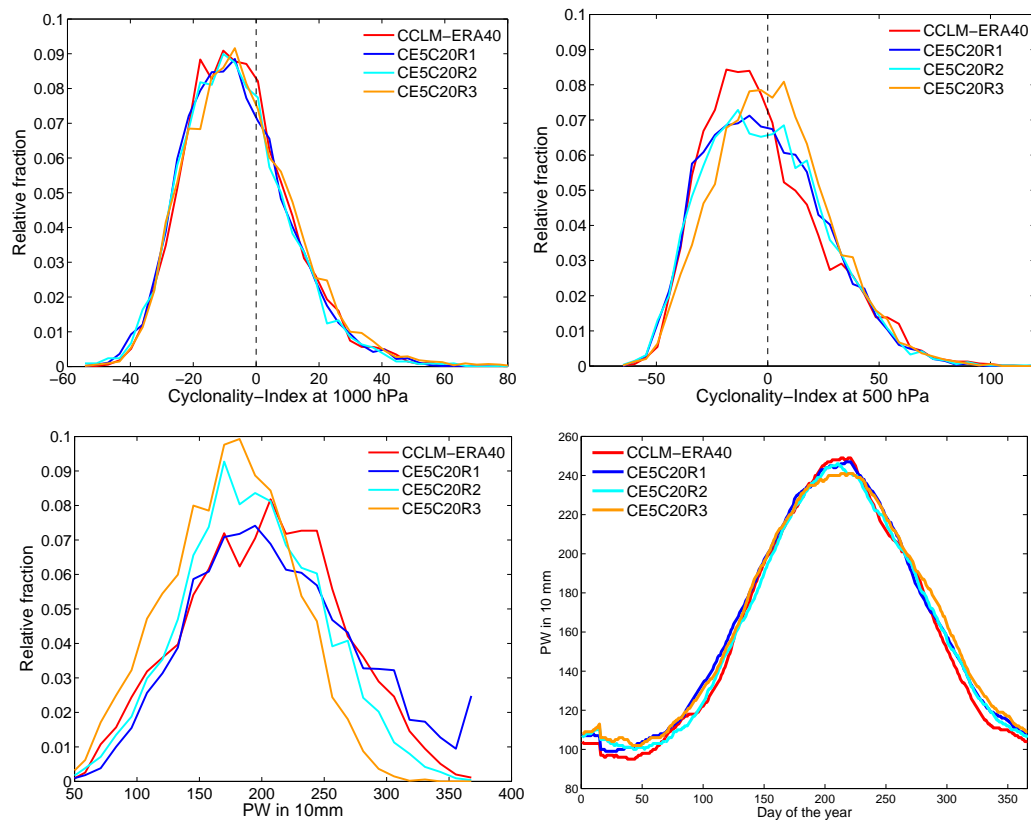


Figure 4.16: Same as Fig. 4.2 but for CCLM-ERA40 (red), CE5C20R1 (blue), CE5C20R2 (light blue) and CE5C20R3 (orange).

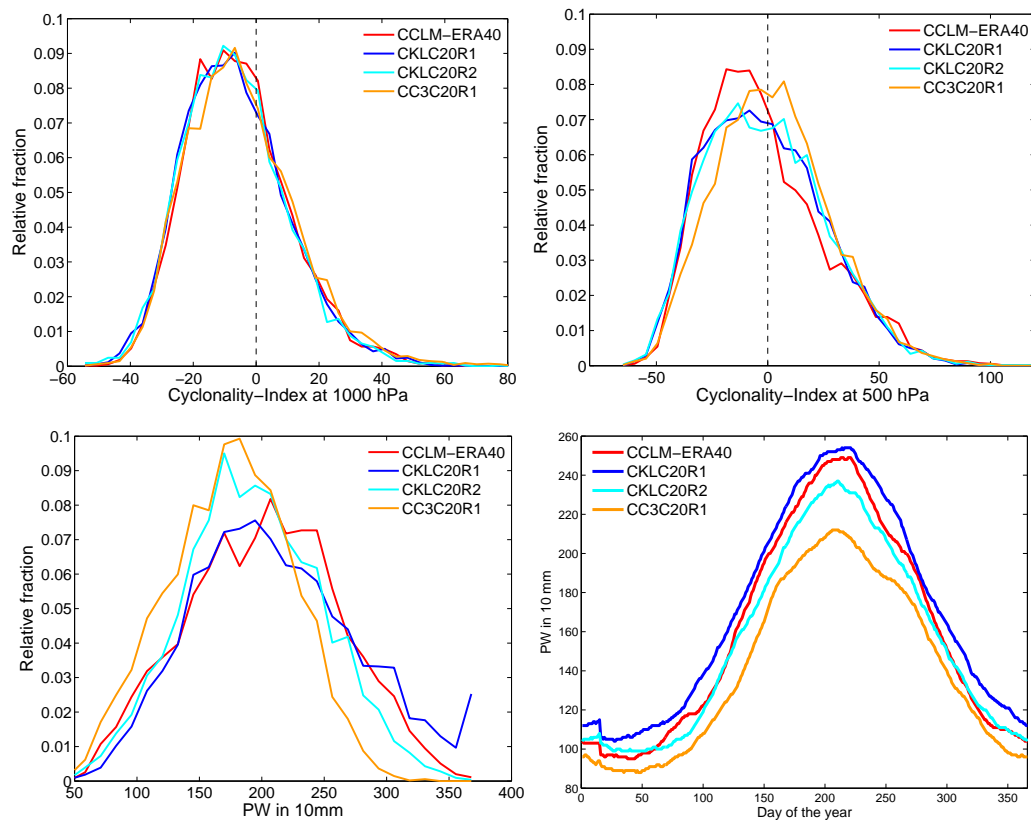


Figure 4.17: Same as Fig. 4.2 but for CCLM-ERA40 (red), CKLC20R1 (blue), CKLC20R2 (light blue) and CC3C20R1 (orange).

### 4.3 Evaluation of a modified weather type classification

In addition to the operational oWLK of DWD, an own classification scheme was developed that considers the mechanisms decisive for thunderstorm development. This routine considers weather types (WT) that are specifically adjusted to predict damaging hailstorms. The parameters and methods used to design the weather types are introduced and explained in the following.

#### Stability index

Kunz (2007a) identified several convective indices that allow to assess the potential for severe thunderstorms. Based on this study, convective and stability indices that are computable on the basis of model data on pressure levels are analyzed to determine the prediction skill of WTs derived from a modified weather type classification scheme. The indices LI, SI, PII, DCI and VT (introduced in Chapter 2) are calculated for the federal state of Baden-Württemberg, for which hail damage data (SV) are available.

#### Dynamic parameter

The second parameter that is used in the new classification scheme of WTs is chosen to describe large-scale lifting related to a mid-tropospheric trough or front. The equivalent-potential temperature (EPT) at 1000 and 850 hPa, the dew point difference (DD) at 850 hPa, the wind shear (WS) and the vorticity advection (VA) were examined with regard to the best prediction skills.

While EPT displays the latent energy of the condensation process that an air parcel stores, the DD gives an estimate about undersaturation of the atmosphere and the VA about changes in the bending of the geopotential and uplift. Vertical wind shear (directional shear) is important for the organization of the convective cells or systems (single cells, multicells, supercells) and consequently the severity of the convection (Sec. 2.1).

#### Determination of a MoWLK with the best prediction skill for hail

To derive the modified classification scheme (MoWLK) with the best prediction skill for damage causing hailstorms, the original parameters used for the oWLK are combined with the two additional parameters. This new classification scheme considers the three triggering mechanisms necessary for thunderstorm development: conditional instability, moisture content and large-scale lifting. Hence, the modified WT includes at least three parameters that describe all these processes. One example of a MoWLK classification is the combination of the cyclonality at two layers as lifting parameter, the precipitable water (PW) as measure for the water content and the LI as indicator for the static stability. To use the additional parameters as part of the classification method, appropriate thresholds need to be defined in order to separate thunderstorm forcing from thunderstorm inhibition conditions. For the stability index, for example, such a separation defines stable and unstable atmospheric conditions. To adjust these thresholds with regard to the

prediction skill for damage causing hailstorms, thresholds are chosen according to the modified WT that has the highest value of the HSS (Par. 3.3.1).

Table 4.4 gives examples for MoWLKs and shows the WT, derived by different MoWLKs, that receives the best prediction skill according to the HSS. Picking up on the example for the MoWLK from above (cyclonality, humidity, stability), the highest HSS is received for the weather type CAWL, indicating cyclonic rotation in 1000 hPa, anticyclonic rotation in 500 hPa, a relatively high water content in the atmosphere compared to the climatological mean and a unstable stratification according to the LI. The highest skill is achieved for a threshold of  $LI \leq -1$  K and the HSS attains a maximum value of 0.252, which is already high for rare events like hailstorms. This value is even higher than the maximum HSS of 0.162 achieved for the weather type SWCAW from the original classification method.

According to this method several MoWLKs are designed that have a higher HSS for specific WTs compared to those from the original method. The highest HSS of 0.342 was achieved for the MoWLK considering humidity (PW), stability (LI) and VA, for the weather type WLP. This WT indicates a high water content, unstable stratification (according to a low LI value) and positive VA (lifting). However, this MoWLK only includes eight different WTs in total, as each parameter holds two classification choices. This low total number of WTs within the MoWLK also affects the HSS and, hence, the value of the HSS needs to be evaluated relative to the absolute number of WTs (8 for the MoWLK and 40 for the oWLK).

A decrease in the number of WTs leads to an increase in the number of days where each individual WT occurs. This implies that the probability of hail occurrence during the WT increases when the hail events are equally distributed over the 8 WTs. Hence, a higher HSS does not necessarily mean that the new MoWLK improves the relationship between hail damage occurrence and WT occurrence. To clarify this argumentation, a simple example is used: Assume there are two WTs that are combined to a single one. The result is an increased HSS, but only due to the reduction of

Table 4.4: Parameters that are combined resulting in different MoWLKs that are good predictors of damage causing hailstorms (SV insurance data). The advection, cyclonality and humidity are the same as for the oWLK. Parameter 1 is an additional stability index (S = stable, L = unstable). Parameter 2 contains processes that force thunderstorm development depending on the chosen threshold. VA = vorticity advection (P = positive, N = negative), EPT = equivalent-potential temperature in 1000 hPa (H = high, L = low).

Weather type	Parameter 1	Parameter 1 Threshold	Parameter 2	Parameter 2 Threshold	HSS
SWCAW	-	-	-	-	0.162
CAWL	LI	-1 K	-	-	0.252
WLP	LI	-1 K	VA	$0 \text{ s}^{-2}$	0.342
CAWL P	LI	-1 K	VA	$-0.5 \text{ s}^{-2}$	0.252
CAWLH	LI	-1 K	EPT	315 K	0.266

WTs. Similarly does an increase in the number of WTs not necessarily leads to a decrease in the HSS. Conversely, assume that one WT is split into two, with both occurring equally as often and also equally as often accompanied by hail. The result would be a decreased HSS of zero. Now assume that one WT favors the development of hailstorms. Due to the splitting it would still occur less often, but is relatively more often accompanied by damage causing hailstorms. Consequently, the HSS would increase even though the total number of WTs is higher.

To account for the potential misinterpretation of the HSS, the VA was tested separately to determine whether this parameter leads to an increase of the prediction skill. If the VA is added to another modified WT, it can be studied how the HSS changes when the absolute number of WTs increases. An increase in the HSS, when increasing the absolute number of weather types, would indicate a better prediction skill for this WT and, thus, imply that the VA has a positive effect on the hailstorm-WT relationship. To test this the VA was added to the weather type CAWL (HSS = 0.252; Table 4.4). Adding the VA as additional parameter (CAWLP: HSS = 0.252) did not increase the prediction skill for hail significantly. Hence, VA does not increase the performance of the MoWLK.

Considering all possible combinations and regarding the increase/decrease in the absolute number of WTs within the MoWLK, the best result of the HSS are obtained with a combination of the five parameters: cyclonality in 1000 and 500 hPa, humidity (PW), LI and EPT at 1000 hPa. The resulting classification scheme is a five character identifier:

$$C_{1000}C_{500}HSE$$

with  $C_{1000}$  and  $C_{500}$  for the cyclonality (relative vorticity  $\zeta$ ) in 1000 and 500 hPa,  $H$  for the humidity,  $S$  for the Stability according to LI (S = stable, L = unstable) and  $E$  for EPT (H = high, L = Low). This MoWLK, comprising 32 different WTs, is used for further analyses. An entire list of the weather types of this MoWLK can be found in Appendix A.3.

### Validation of MoWLK

Several WTs of the MoWLK do not occur in the C20 period from 1971 to 2000 based on the CCLM-ERA40 and ERA40 data (Fig. 4.18). It is evident that WTs with a high value of LI ( $LI > -1$  K) and those with a low EPT ( $\theta_e < 315$  K) occur more often. This is plausible as the parameters characterizing this classification method are chosen with regard to a better forecast skill of hailstorms. Hence, thresholds are chosen at the tail of the distributions of the parameters causing a disproportionate occurrence of hail-related WTs to be expected.

Large deviations in the absolute fraction of the WTs derived from CCLM-ERA40 and ERA40 are evident in Fig. 4.18 (right). Some deviations are far more than 100% for some WTs (AAWLH and AAWSL) and some WTs, particularly those with a high EPT and a low LI, show large deviations between CCLM-ERA40 and ERA40. Thus, this method seems not to be applicable to

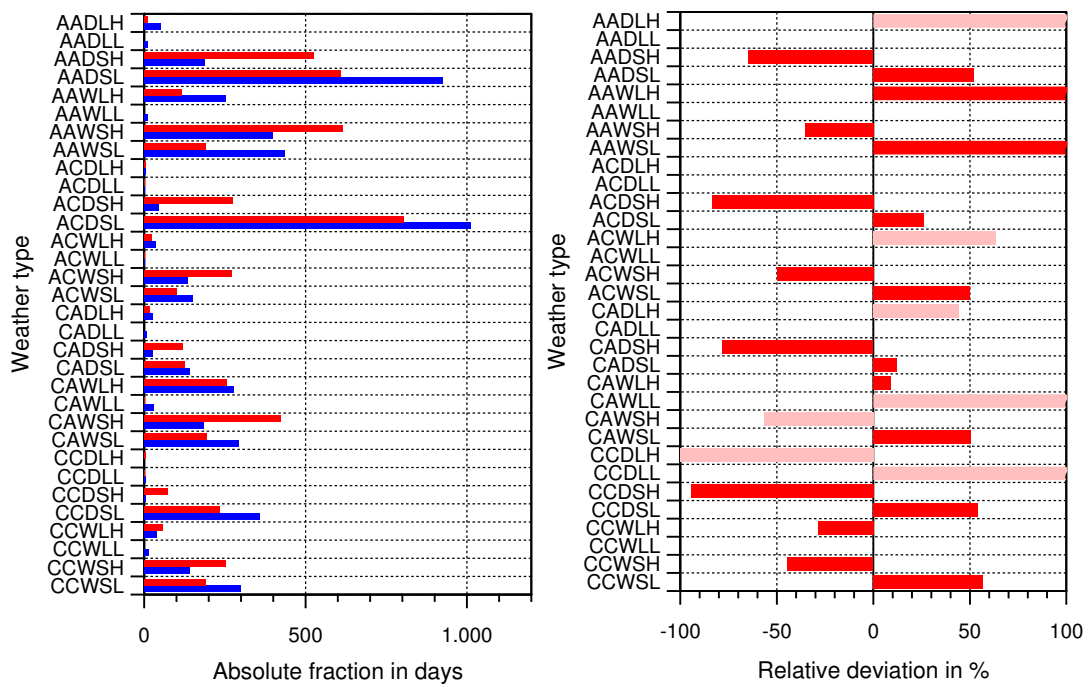


Figure 4.18: Same as Fig. 4.1 but for MoWLK. Light red colors mark WTs that occurred less than 100 times between 1971 and 2000 (summer).

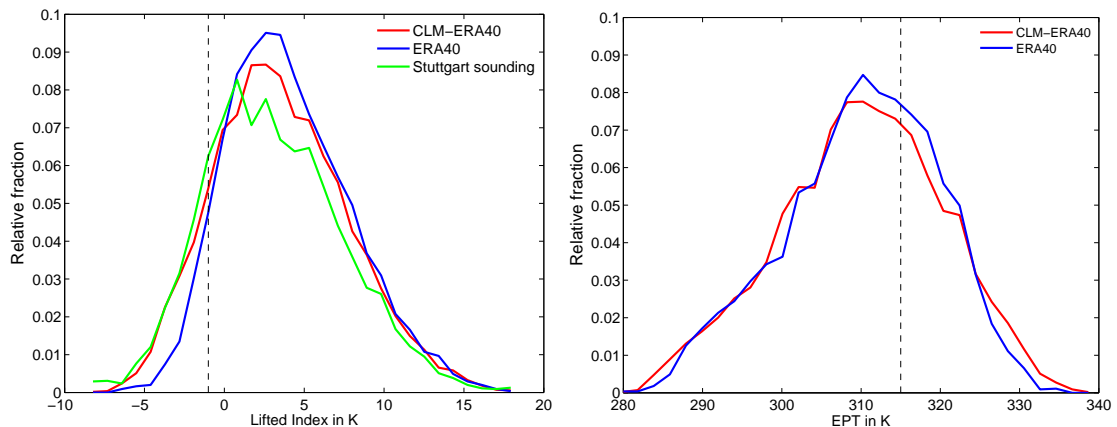


Figure 4.19: Distributions of LI and EPT in 1000 hPa derived by ERA40 (red), CCLM-ERA40 (blue) and by radiosonde measurements in Stuttgart (green). Dotted lines indicate the chosen thresholds.

different models. But what causes those differences? In order to evaluate the reasons behind these differences, the distributions of LI and EPT obtained from both reanalysis data and radiosonde data are shown in Fig. 4.19. The distributions of the LI (left) generally appear to conform well. However, there are larger deviations for values in the range between -8 K and 1 K, the region that separates unstable from stable WTs. The CLM-ERA40 data hold more days with an unstable atmosphere compared to those of the ERA40. Hence, there is a higher potential for hail-related WTs to occur in the CCLM-ERA40 data set compared to the ERA40 data, because an unstable atmosphere supports thunderstorm and hailstorm development. To estimate the relationship of

the distributions, they are compared with LI derived from the radiosonde data taken in Stuttgart (Par. 3.1.3).

The radiosonde station in Stuttgart is the only one in Baden-Württemberg and thus, the entire region is limited to being represented by a single point measurement. However, Brombach (2010) showed that LI and SI derived from reanalyses are almost homogeneously distributed over Baden-Württemberg. Additionally, the pressure level used to derive LI is the 1000 hPa level, which is less dependent on the surface layer. The ERA40 reanalyses have only a coarse spatial horizontal resolution. Hence, complex orography is not resolved and does not affect the value of LI. This allows the use of LI derived from the Stuttgart sounding as representative for the Baden-Württemberg region. This is confirmed by the fact that even if the LI distributions, derived from the reanalysis and CCLM-ERA40 are determined from average values for Baden-Württemberg, they are unexpected conform with the distribution of the LI in Stuttgart. However, especially in the range of instability of the distributions, the LI from the CLM-ERA40 data conforms much better with the observations than that from the ERA40 reanalyses. As such, it can be expected that the LI, derived from the CLM-ERA40 model data, is more reliable, but it also indicates that the LI is a source of error in the MoWLK and reduces its applicability when considering different model realizations. Similar results are also evident in the histograms of EPT (Fig. 4.18, right). Values of EPT derived from CLM-ERA40 and ERA40 show larger deviations in the relative frequency, especially in the range around the chosen threshold (315 K). Hence, the potential for deviations between the resulting WTs is higher.

In summary, the introduced method leads to higher forecast skill of specific WTs describing the occurrence of hail, but the applicability to different data sets is problematic, in particular due to the thresholds defined for the convective parameters. The hail-related WTs (CAWLH, AAWLH, CCWLH and AAWSL; Appendix C) are especially overestimated in their frequency by CCLM-ERA40 in comparison to ERA40, implying that especially those types cannot be reproduced well by different models or realizations. Additionally, some of the hail-unrelated WTs (AAWSL, AADSL, ACDSL, CCDSL) are also significantly overestimated by CCLM-ERA40 (Fig. 4.18).

Due to these large deviations, the respective hail-related and hail-unrelated WTs are only analyzed for the CCLM-ERA40 data set, as the modification of the weather type classification scheme is adjusted to this data set. However, with more investigations regarding the validation of this method (e.g., bias corrections or exchange of some parameters), the method could be improved to provide more robust results when applied to different climate models.

### **Temporal variability of hail-related weather types**

To determine the temporal variability of hail-related WTs and, thus, the changes in the occurrence of hail damage, linear trends over variable periods were calculated. The trends were calculated for periods of at least 10 years and visualized by trend-matrices. The trend matrices are structured as follows: The entire time series of hail-related WTs is split into many subsequences. The start year of those subsequences is given on the abscissa, while the end year is assigned on the ordinate. The

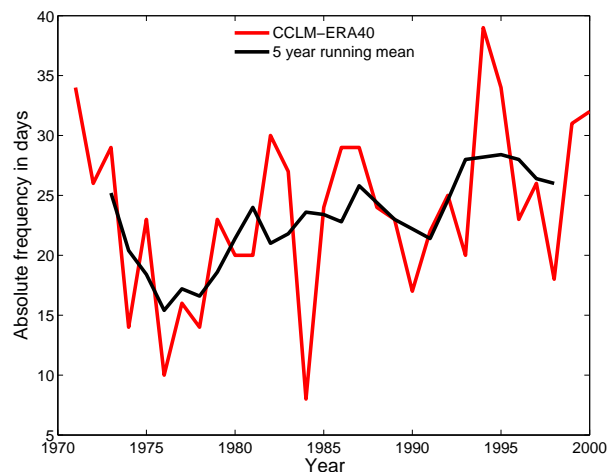


Figure 4.20: Absolute frequency of hail-related WTs derived from CCLM-ERA40 and obtained with the modified classification method. The black line shows the 5-year running mean.

linear trend of the number of hail-related WTs is computed for each subsequence and displayed as colored box. Those boxes indicate an increase or decrease in the number of hail-related WTs per year (red/yellow: positive, blue/green: negative). Furthermore, consideration of  $n \geq 10$  years allows the use of the Mann-Kendall significance test (Par. 3.3.2) to detect significant changes. Accordingly, insignificant changes are plotted as white boxes.

Figure 4.20 shows the time series of the hail-related WTs derived from CCLM-ERA40. The mean number of these WTs according to the MoWLK is 24 days. Large deviations from this mean are evident in the time series ( $24 \pm 7$  days), with a minimum number of only eight days and a maximum of up to 39 days. Between 1970 and 1976, a significant decrease in the number of days can be observed in the time series, which is also evident in the trend matrices for an period of 10 years (Fig. 4.21). After this decrease, the number of hail-related WTs increases significantly by 9 days between 1972 and 2000. However, no significant trends can be observed with the start year later than 1978. This is interesting as the observations (SV data) indicate a significant increase (Chap. 1; Fig. 1.1). However, the time series of WTs indicate that the trends are probably not significant due to the large inter-annual variations, especially in 1984 and 1994.

As the time series is very short, no proper statistical analyses of periodic behavior, such as the application of an FFT, can be applied. To get an estimation of certain periodicity, the 5-year running mean is plotted in Fig. 4.20. Interestingly, this mean indicates a continuous increase in the number of hail-related WTs, beginning in the year 1975. An increase of approximately 10 days can be observed. Disregarding the trend, the 5-year running mean implies a vague periodic behavior of approximately 15 years, recognizable by the two minimums in 1975 and 1990 and three maximums (1973, 1984 and 1994).

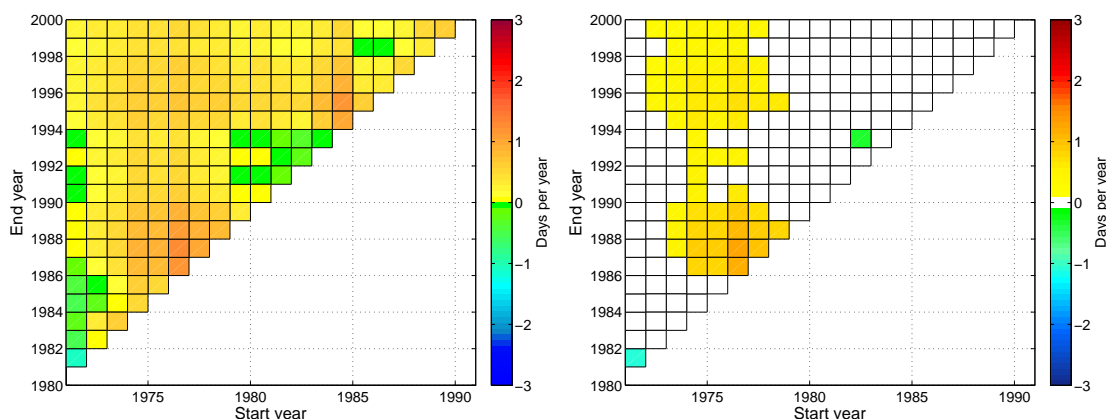


Figure 4.21: Linear trend matrices of hail-related weather types determined from CCLM-ERA40 between 1971 and 2048. In the right panel only trends are displayed that have a statistical significance of more than 80% according to the MK trend test.

### Temporal variability of hail-unrelated weather types

An increasing number in hail-related WTs may lead to a more frequent occurrence of damage-causing hailstorms. Likewise would a decrease in the number of hail-unrelated WTs likely affect the thunderstorm frequency. To investigate this further, a time series for hail-unrelated WTs is analyzed to determine the changes in the thunderstorm potential.

The number of days with prevailing hail-unrelated WTs is much higher (91 days, Fig. 4.22) compared to the number of hail-related WTs. This is because the classification method is adjusted towards a good correlation between hail damage days and WTs. Thus, as hail damage days are relatively rare (15 days per summer half-year according to SV loss data), the number of hail-unrelated WTs is higher. Large inter-annual variability can be seen ranging from 71 days in the year 2000 to 110 days in the year 1974, which also indicates a higher standard deviation ( $91 \pm 12$  days). However, a remarkable negative trend between the 1970s and 2000 can be recognized, which is statistically significant (Fig. 4.23). The trend amounts to nearly one day per year, a total decrease of 24 days (1976-2000) which is larger compared to the positive trends for hail-related WTs. This indicates that the potential for the occurrence of damage causing hailstorms is not just increasing due to a more frequent number of hail-related WTs, but also due to an even more pronounced decrease in the number of days that do not favor the development of thunderstorms. Even if the probability is smaller for thunderstorms to occur during the prevailing 'remaining' WTs (those that are classified neither as hail-related nor as hail-unrelated), it has to be taken into account when estimating the number of hail damage days.

Investigations of the periodicity by analyzing the 5-year running mean (Fig. 4.22) yields results similar to those derived for the hail-related WTs. Some harmonic behavior of eight years is indicated, but is not as pronounced as in the other time series. Additionally to this long-term periodicity derived from the 5-year running mean, there are shorter periodicities noticeable in the

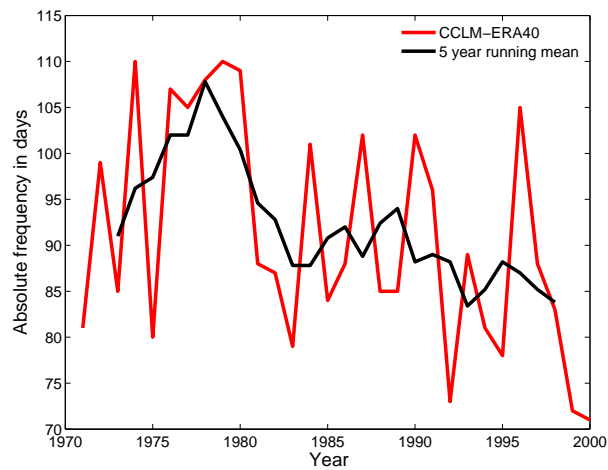


Figure 4.22: Same as Fig. 4.20 but for hail-unrelated weather types.

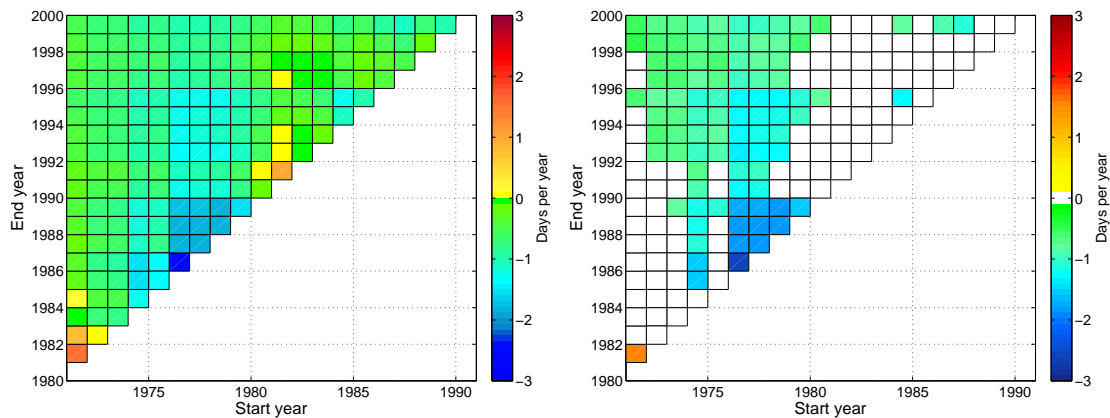


Figure 4.23: Same as Fig. 4.21 but for hail-unrelated weather types.

original signal. Regular maximum peaks in the years 1984, 1987, 1990, 1993 and 1996 indicate some shorter periodicity between the years 1983 and 2000. However, this analysis is only an estimation and would need to be verified by statistical methods.

In summary, an increase in the frequency of hail-related WTs and a decrease in the number of hail-unrelated WTs imply a significant increase for the potential of damage causing hailstorm occurrence in the past. This conforms well with the trends derived by observations of the SV and indicates an adequate relationship between WTs and hailstorm occurrence. Thus, the method seems to be a good estimate for the climatological analyses of hailstorms, although it needs to be improved with regard to its applicability to different data sets.



# 5. Temporal variability of hail-related weather types

This chapter will focus on long-term variability of hail-related and hail-unrelated WTs, including the detection of possible linear trends and periodicities. As the RCMs are not able to reproduce the course and development of real synoptic systems, it is important to analyze the different models with regard to their individual epistemic uncertainty.

To assess epistemic uncertainty, eight different RCM realizations are considered comprising different initialization times and initial conditions (Run 1, 2 and 3 of the GCM), emission scenarios (A1B, B1), RCM realizations (CCLM versions 4.8 and 3.1) and forcing global models (ECHAM5, CGCM3). Unfortunately, a comparison between the CCLM and other RCMs was not possible due to limited availability of model data on different levels, which are necessary in the WT classification routine. Note that this is important regarding the interpretation of the results, as variability might be caused by the model physics.

## 5.1 Temporal variability of hail-related weather types

To determine the temporal variability of hail-related WTs according to the oWLK, linear trends over variable periods were calculated and displayed in trend matrices explained in Section 4.3.

### 5.1.1 Detection of linear trends

The upper panel of Fig. 5.1 shows the trend matrix from 1971 to 2048 (left) and the corresponding significance (right) at the 80% confidence level according to the MK significance test for CKLA1BR1. Over the whole time period displayed, a positive linear trend of hail-related WTs can be noticed, but this trend is not significant. A significant linear trend is evident until the early 2010s, with an increase of less than one day per year or approximately 9 days for the period 1971 to 2002. This positive trend possibly already affects past hailstorm occurrence, as the fraction of hail damage days on the hail-related WTs was around 20% in the past (1986-2000). Larger significant linear trends of more than three days per year can be identified only for shorter time periods of approximately 12 years, for example from 1975 to 1987 or from 1988 to 2000. Those positive trends persist for approximately 5-6 years (1971-1978, 1988-1992, etc.) until the trend changes

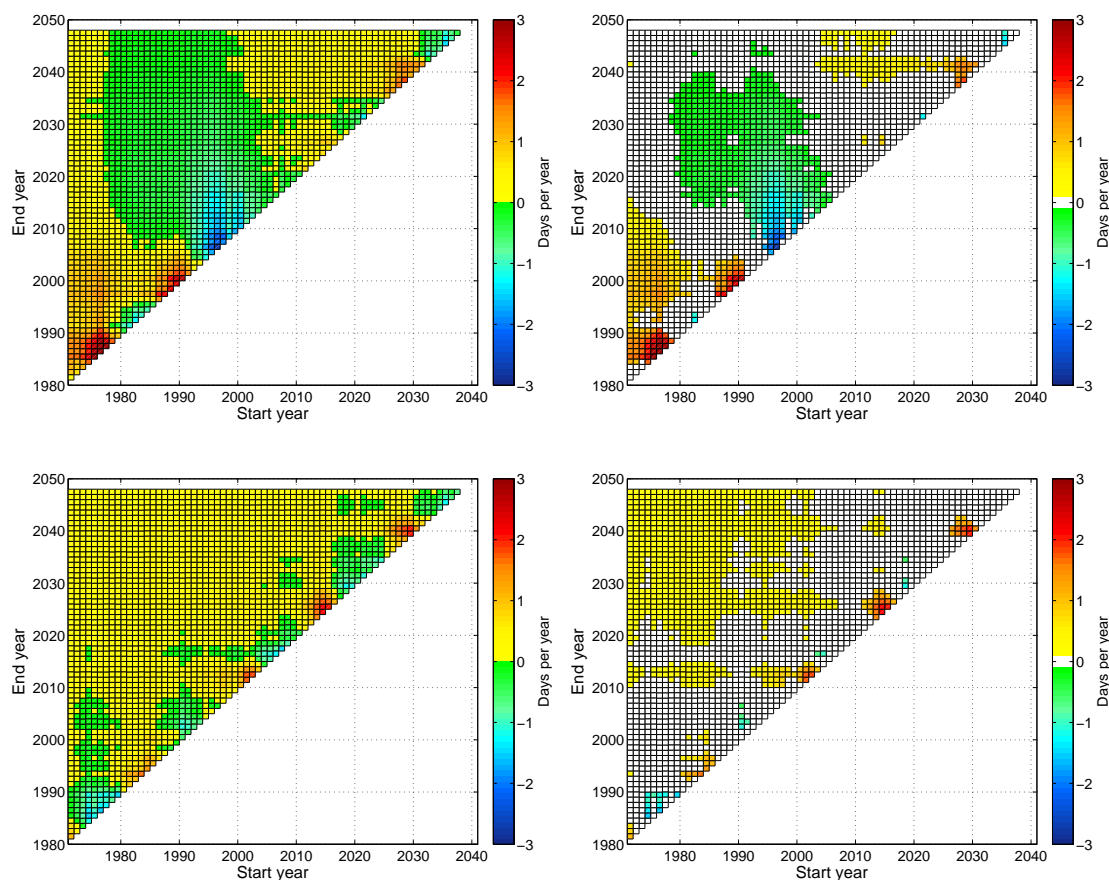


Figure 5.1: Linear trend matrices of hail-related WTs determined from CKLC20R1/CKLA1BR1 (top) and CKLC20R2/CKLA1BR2 (bottom) between 1971 and 2048. In the right panel, only trends are displayed that have a statistical significance of more than 80% according to the MK trend test.

its algebraic sign and becomes negative. These periodic changes of the trends are indicated by several peaks in the time series which cause also significant negative trends between 1980 and the late 2030s, as evident in the matrices for CKLA1BR1 and CKLB1R1 (Fig. 5.1 and Fig. 5.2, top panels). The decrease in the number of hail-related WTs sums up to a total of approximately 9 days (1982 to 2039). Furthermore, another positive significant trend is evident in the CKLA1BR1, beginning in 2005.

Those 'time blocks' of trends with a statistical significance of  $> 80\%$  lead to the question of whether a kind of periodicity in the occurrence of hail-related WTs can be detected. To answer this question, it is important to determine if those potential periodicity patterns are also evident in the other models. By considering several RCM results, epistemic uncertainty can be assessed.

The trends of the time series of hail-related WTs derived from Run 2 of CKLA1B and CKLB1 (Fig. 5.1 and Fig. 5.2, bottom) indicate similar significant short-term trends in the future projections, similar to those of Run 1. These positive significant trends of more than three days again occur for approximately 5 to 6 years in the time series. This implied periodicity in the time series

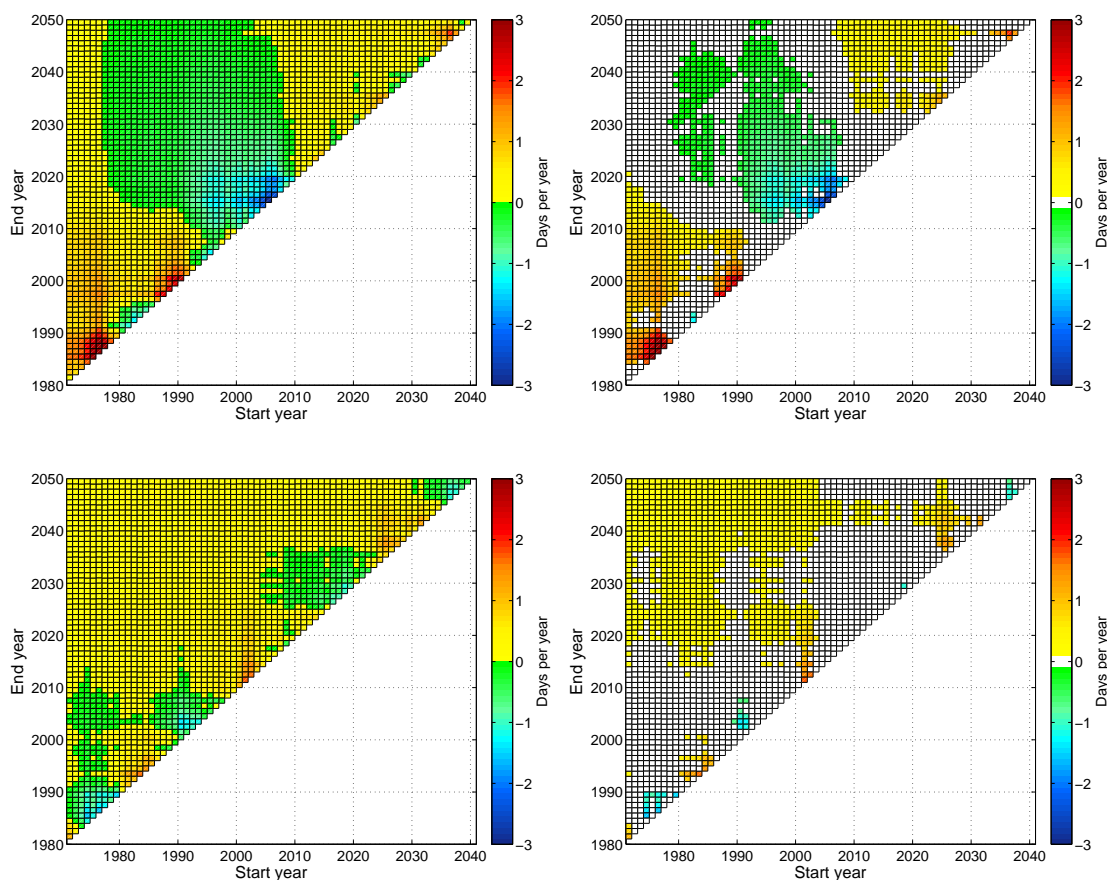


Figure 5.2: Same as Fig. 5.1 but for CKLC20R1/CKLB1R1 (top) and CKLC20R2/CKLB1R2 (bottom).

will be analyzed in Paragraph 5.1.2. The long-term trends of Run 2 differ between CKLA1B and CKLB1. Except for negative trends over shorter periods (e.g., 1971 to 1991, 2018 to 2038), which are not significant, most of the long-term trends are positive by less than one day per year. Over the whole period from 1971 to 2048, the trend is positive with a total increase of approximately 11 days. Interestingly, the trends before 2010 are not significant (1971 to 2010) as well as those after 2010 (2010 to 2048). This indicates that there is a difference in the characteristics of hail-related WTs between 1971 to 2010 and 2011 to 2048. To find the reasons for this abrupt gradient in the significance of the positive trends, the time series is split into two sequences at the year 2010 (the year with the largest gradient). Figure 5.3 shows the time series with the mean of the number of hail-related WTs for the two separated time periods. A 'step' structure of the mean can be detected, which causes those gradients in the trend matrices. Whether this 'step' structure is due to natural variability or climate model characteristics can be clarified by analyzing the whole ensemble of climate models (Par. 5.1.3); this emphasizes the importance of the use of an ensemble of RCM (even if the used ensemble is a mini-ensemble comprising only a limited number of eight possible realizations).

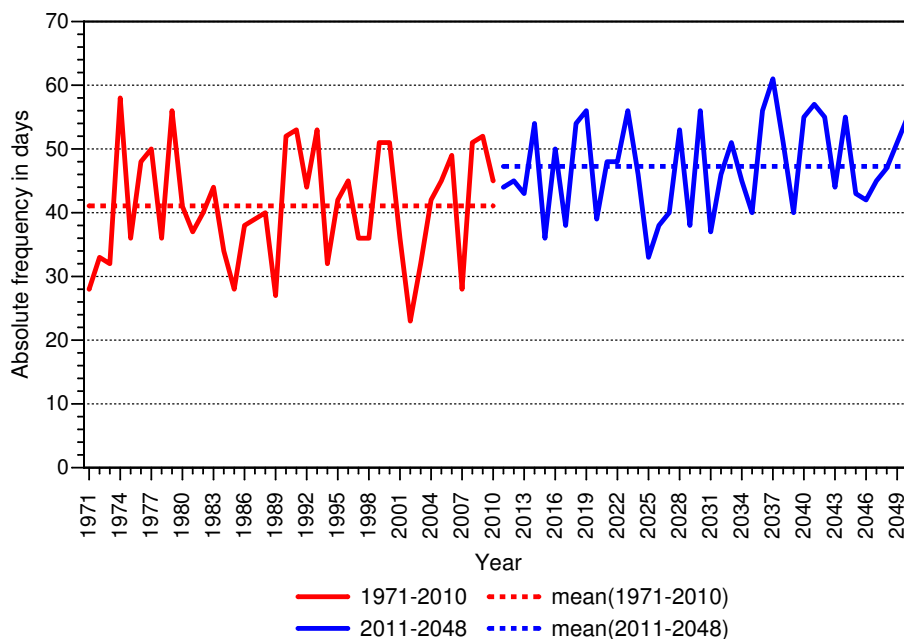


Figure 5.3: Absolute frequency of hail-related WTs, derived from CKLC20R2/CKLB1R2 and the mean values (dashed) of the two time periods 1971-2010 and 2011-2048.

The results of the CKLA1BR1/R2 and CKLB1R1/R2 (cf. Table 3.1) show substantial differences in the trends of the number of hail-related WTs between Run 1 and Run 2. By contrast, differences between the emission scenarios A1B and B1 are not evident (Fig. 5.1 and Fig. 5.2). This indicates that the year, where the GCM was initialized is of major importance for the hail-related WT climatology, while the emission scenarios have no strong influence on the weather patterns over Germany at least for the nearer future until 2050.

As the CCLM-ECHAM5 runs are only available for the time periods 1971 to 2000 and 2011 to 2050, the trends were calculated separately for the control period and future projections. These two investigation periods are compared with the CCLM-KL model runs to derive uncertainties induced by the use of different RCMs. Both models are driven by the same global climate model ECHAM5, but use different RCM versions of the CCLM. By comparing the results obtained from these two RCM runs, the impact of the RCM on the linear trends is evaluated. Figure 5.4 shows the trend matrices of CE5A1BR1 for the control period C20 (top) and the future projection (bottom). The positive trends of the control periods until 1994 are similar compared to CKLA1BR1, while those determined from the CCLM-ECHAM5 are not significant for most of the sequences. Likewise, trends for the series beginning in 1980 are negative in both models, while most of them are not significant as well. However, the long-term trends derived from CKLC20R1 and CE5C20R1 show several differences. For time series of hail-related WTs that begin in 1971-1979 and end in 2000 the trends determined from CKLC20R1 are positive and those from CE5C20R1 are negative. This can be explained by the difference of the relative frequency of hail-related WTs of those models (Fig. 5.1.1) in the mid to end of the 1990s. Even if the number of hail-related

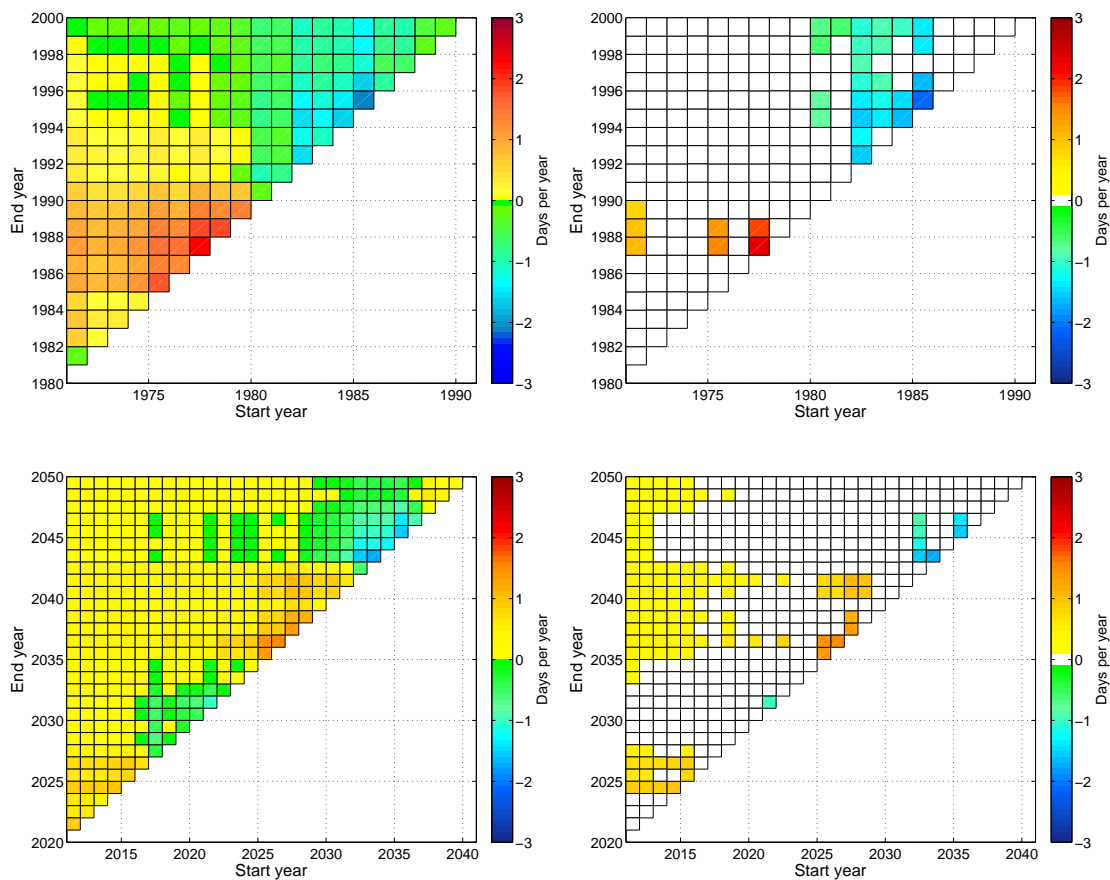


Figure 5.4: Same as Fig. 5.1 but for the control period C20 (top) and the A1B scenario (bottom) of the model CLM-ECHAM5.

WTs conforms well between the two model versions, the corresponding linear trend is affected by some peaks in the time series. Therefore, these trends are statistically not significant. Moreover, the trends of the future projections conform well between both models, as do the linear trends of the second model runs (cf. Appendix D).

The results obtained by using another driving GCM (CCLM-CCCma3) show similar characteristics of the linear trends. But they also feature some differences in comparison to the CCLM-KL (Fig. 5.6 and Fig. 5.2). The trends at the beginning of the control period (until 1998) are almost positive, but very small and not significant. Considering a longer period from 1971/1990 to 2006 yields significant positive trends with an increase of maximal two days per year. From 1990 or 2000 until 2028, the trends are significantly negative by less than one day per year. This variability and the magnitude of the trends are similar to CCLM-KL, but the time period of significance is much shorter. Additionally, the mentioned block-wise significant trends are similar to the CCLM-KL (Fig. 5.6) but less distinctive.

The analysis of the trend matrices show that there are differences in the linear trends due to the RCM versions and different forcing GCMs. These differences are investigated in the following.

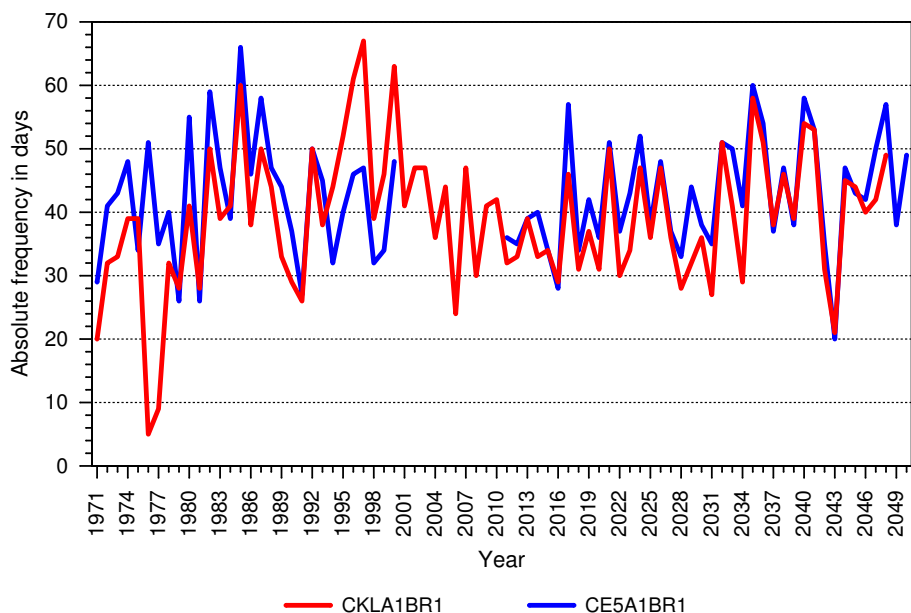


Figure 5.5: Absolute frequency of hail-related WTs per summer half-year according to CKLC20R1/CKLA1BR1 (red) and CE5C20R1/CE5A1BR1 (blue) for the years 1971 to 2050.

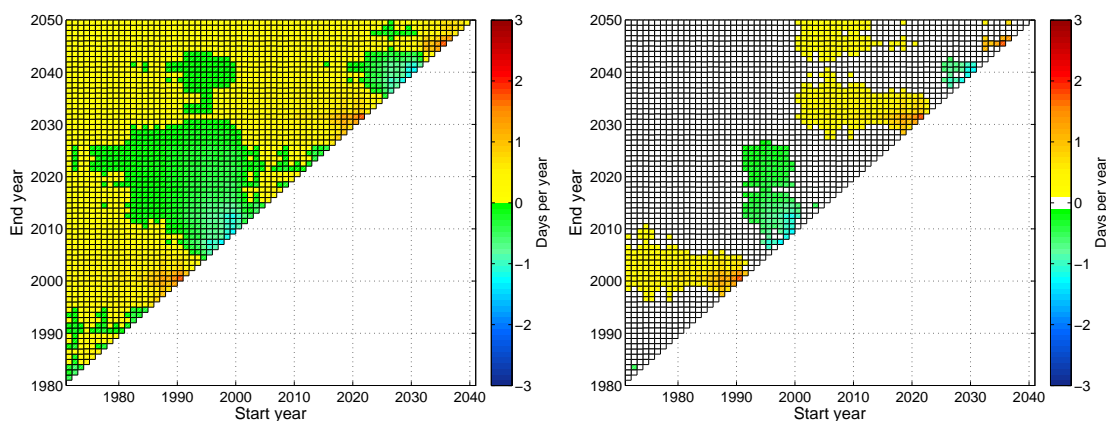


Figure 5.6: Same as Fig. 5.1 but for the hail-related WTs derived from CC3C20R1/CC3A1BR1.

As a comparison between the RCMs is difficult because of the different time periods of CCLM-KL and CCLM-ECHAM5, the absolute fraction of the WTs derived from from CKLA1BR1/R2 and CE5A1BR1/R2 for a 30 year time period within the future projections is analyzed for the period 2019-2048 (Fig. 5.7). The time period is chosen according to other studies using ensembles of climate models (e.g., Mayer et al., 2010) but, due to the data availability of the CCLM-KL data sets, the period is shifted by two years. The absolute fraction of hail-related WTs for the second model run differs just slightly between the different RCM model versions. The maximum difference is 51 days or 11% for the WT SWAAW. Similar results can be drawn from the absolute frequency of hail-related WTs for the first model run, but the relative deviations are higher (41 days or 18% for SWCCW). Concluding, the different versions of the RCM have only a marginal influence on the frequency and linear trends of hail-related WTs. Especially the absolute fre-

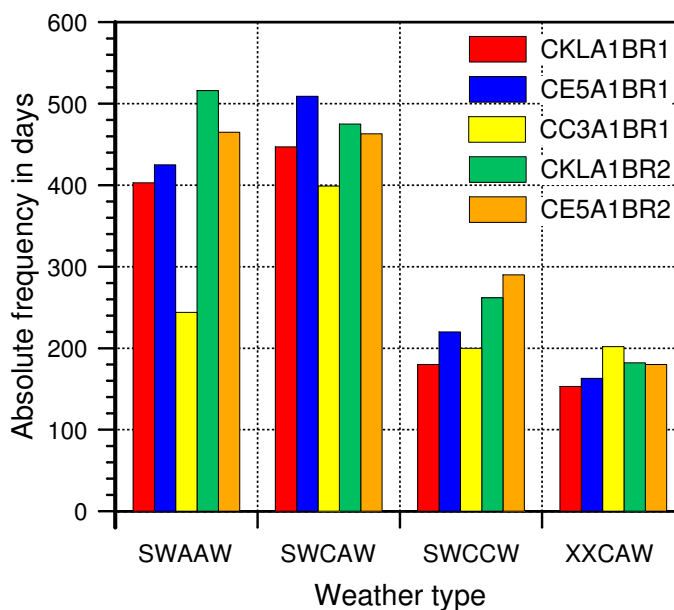


Figure 5.7: Absolute frequency of hail-related WTs per summer half-year derived from CKLA1BR1 (red), CKLA1BR2 (green), CE5A1BR1 (blue), CE5A1BR2 (orange) and CC3A1BR1 (yellow) for the years 2019 to 2048.

requencies from CKLA1BR1 and CE5A1BR2 conform well. This implies that the different model resolutions ( $0.167^\circ$  for CCLM-KL and  $0.44^\circ$  for CCCLM-ECHAM5) play only a minor role for the determination of hail-related WTs.

The influences of the different GCMs on the trends can be confirmed by the distribution of the absolute frequency of hail-related WTs from CC3A1BR1 for the period 2019-2048 (cf. Fig. 5.7). Maximum deviations of nearly 40% for the WT SWAAW are evident, indicating a major influence of the GCM on the frequency of hail-related WTs.

In summary, the largest difference between the linear trends of hail-related WTs are found for different realizations of the GCM (ECHAM5) in terms of different initial conditions. This indicates that the model climate with regard to the WTs is highly dependent on the initialization time and the initial conditions of the GCM. Furthermore, differences are also caused by the individual GCMs. Trend patterns of CCLM-KL, driven by ECHAM5, are also evident in the CCCma3, but are less pronounced in the CCLM-KL. Differences due to the RCMs are difficult to examine, since the period of 2001 to 2010 is missing in CCLM-ECHAM5 and may result in insignificance of trends for these sequences. Disregarding the statistical significance, the results for the WTs of the C20 and the future projections obtained from the two CCLM model versions and runs conform well, even though the resolution differs. In all cases, the trends are only marginally affected by the underlying emission scenarios.

### 5.1.2 Detection of periodicities

As discussed in the previous paragraph, most of the models indicate short-term variability in the trends of the time series, which may be due to a certain harmonic behavior in the time series. To analyze possible periodicities the results obtained from the RCMs with an adequate length and without gaps, e.g. CCLM-KL and CCLM-CCma3, were transformed to the frequency space by applying an FFT algorithm to the autocorrelation function (ACF; see Chapter 3, Par. 3.3.3). Figure 5.8 (top) shows the relative variance of CKLA1BR1 vs. frequency (left) and the corresponding time axis (right).

As expected and discussed earlier, some peaks in the relative variance indicate that the mentioned short-term trends can be related to periodic behavior of hail-related WTs. The spectra indicate some shorter periodicity of approximately 2 to 4.5 years in the time series of hail-related WTs derived by CKLA1BR1, CKLB1R1 and CC3A1BR1. Furthermore, the WTs follow a periodicity of 12 to 16 years.

A periodicity of approximately 14 to 18 years is detected also in the second runs of CCLM-KL (Appendix D.3). The relative variance of CKLA1BR2 shows an additional peak at approximately 7 years. Whether this maximum is due to periodicity or caused by a convolution through the transformation into the frequency space cannot be determined. According to the fact that all maxima of the variance occur at a multiple of the same frequency, convolution caused by spectral 'leakage' is most likely and the results of this spectrum should be handled with care. However, the power spectra determined from the results of the second GCM runs show similar results for the variability of the hail-related WTs in comparison to the first runs with only an offset of approximately three years towards a longer periodicity. This indicates that the differences between the first and second GCM/RCM runs impact the magnitude and direction of the linear trends, but not the periodicity of hail-related WTs.

### 5.1.3 Variability of hail-related weather types in an ensemble of regional climate models

The differences between the model realizations illustrate why it is important to consider not only one RCM run, but to use an ensemble of different model realizations and scenarios to determine temporal variability of hail-related weather patterns. Since it is not possible to determine the 'best' model run, each model needs to be taken into account with the same probability to predict the future climate. Hence, a mini-ensemble of eight members with the RCM of CCLM-ECHAM5, CCLM-KL and CCLM-CC3ma, different initialization times (R1,R2,R3) and emission scenarios (A1B, B1) is created for the time periods 1971 to 2000 and 2011 to 2048. An examination of periodicity is not possible due to the short length of CCLM-ECHAM5 runs, which are integrated in the mini-ensemble.

Figure 5.9 shows the frequency of the hail-related WTs from the ensemble in terms of mean and standard deviation. The mean of WTs for C20 amounts to 41 days, with a maximum of 54 days

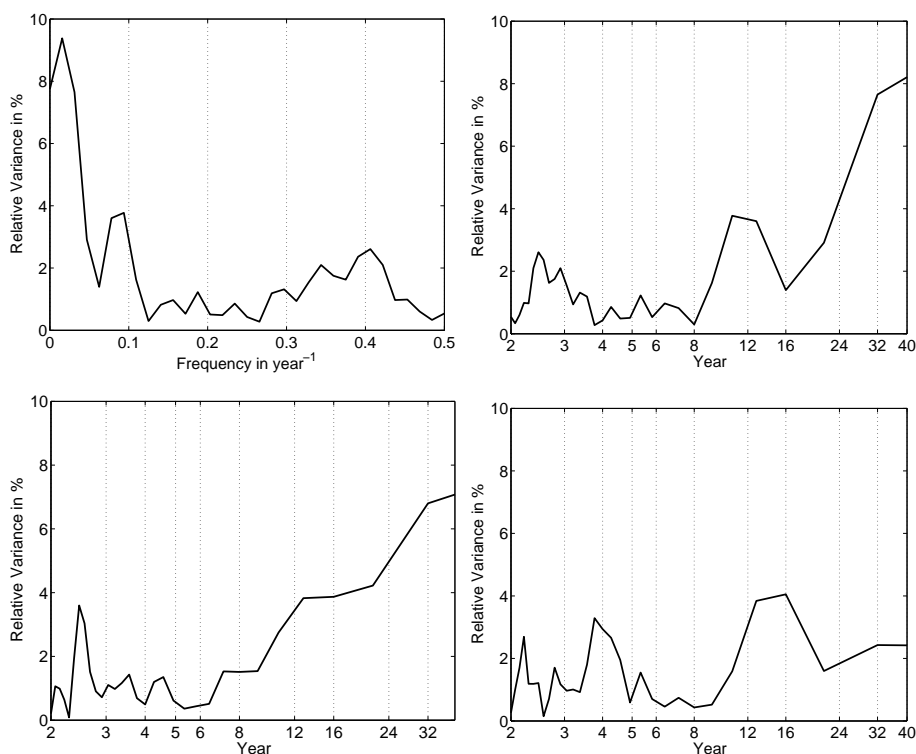


Figure 5.8: Frequency spectra of the autocorrelation function of hail-related WTs. Top: CKLC20R1/CKLB1R1; Bottom: CKLC20R1/CKLA1BR1 (left), CC3C20R1/CC3A1bR1 (right).

and a minimum of 26 days. Those large fluctuations lead to statistically insignificant trends for many of the sequences within the time series between 1979 and 2000, which are also obvious in the trend matrices (Fig. 5.10, top). Furthermore, large standard deviations of up to 25 days indicate that there are large differences in the number of hail-related WTs derived by the different RCMs, implying a large uncertainty. However, significant trends are evident for the entire time series, as well as in the first part of C20 (Fig. 5.10). The number of days with occurring hail-related WTs increases by 12 days between 1971 and 2000 from approximately 35 to 47 days. This leads to a higher potential for the occurrence of damage causing hailstorms.

In the year 2011, the number of hail-related WTs is lower than in the late 1990s. Either a decrease of hail-related WTs cannot be identified due to the missing period between 2001 and 2010, or the models indicate a different WT climatology of those WTs which are related to hail. However, the mean number of hail-related WTs for the future projection is just about 3 days higher than the mean for C20. The annual fluctuations are similar to C20 with a range of 27 days and indicate high uncertainties between single years. The standard deviation resulting from the differences between the model realizations is lower for the future projection period ( $\sigma_{max} = 26$ ) compared to this of C20 ( $\sigma_{max} = 17$ ). This indicates that the emission scenarios have no influence on the frequency of hail-related WTs until 2048. However, positive trends are evident in the future projections of hail-related WTs derived from the ensemble. While there are no trends for the

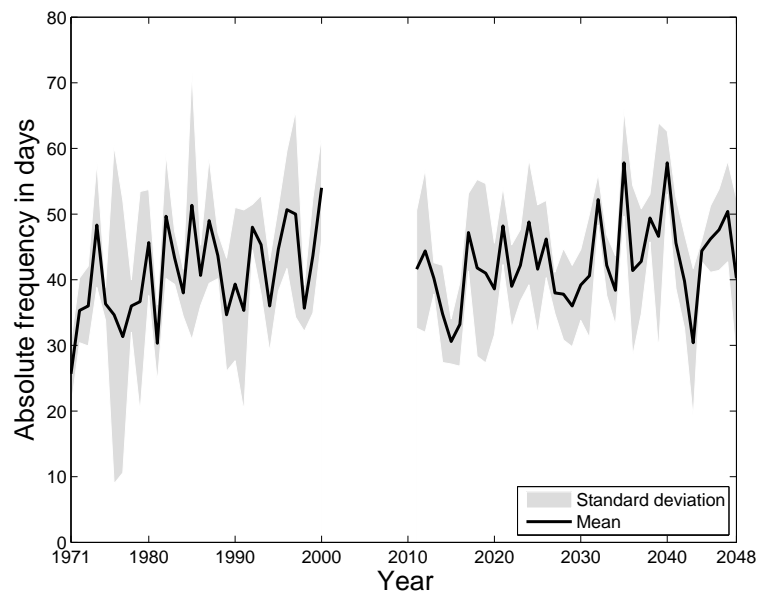


Figure 5.9: Number of hail-related WTs for the control period C20 and the future projection period derived from CCLM-ECHAM5, CCLM-KL and CCLM-CC3ma with mean values (black line) and standard deviation (gray).

first 20 years, a significant trend for time series longer than approximately 30 years can be seen (Fig. 5.10). According to the linear regression the number of hail-related WTs increases from 39 days in 2011 to 46 days in 2048. Note that the analysis is limited to the mean values and that the mentioned uncertainty caused by the standard deviations between the different RCM realizations is not considered.

## 5.2 Variability of hail-unrelated weather types

### 5.2.1 Detection of linear trends

As a decrease in the number of hail-unrelated WTs may probably affect the overall thunderstorm probability, the time series for these WTs are analyzed with respect to trends and periodicity. The trend analysis of the time series, derived from CCLM-ECHAM5 shows significant trends only for very short subsequences of the control period (Appendix D.4). This is due to the higher annual variability compared to the number of hail-related WTs (Fig. 5.11). In 1977, for example, 85 days with hail-unrelated WTs occurred according to Run 1, while in 1978 those WTs prevailed just for 42 days.

Some significant negative trends for subsequences between 2012 and 2031 (Run 1) or 2026 (Run 2) are evident in the future projection (Appendix D.4), mainly due to a very small number of hail-unrelated WTs in 2039. Run 3 does not show any significant trends during this period at all, indicating that initial conditions are decisive for the variability of hail-unrelated WTs.

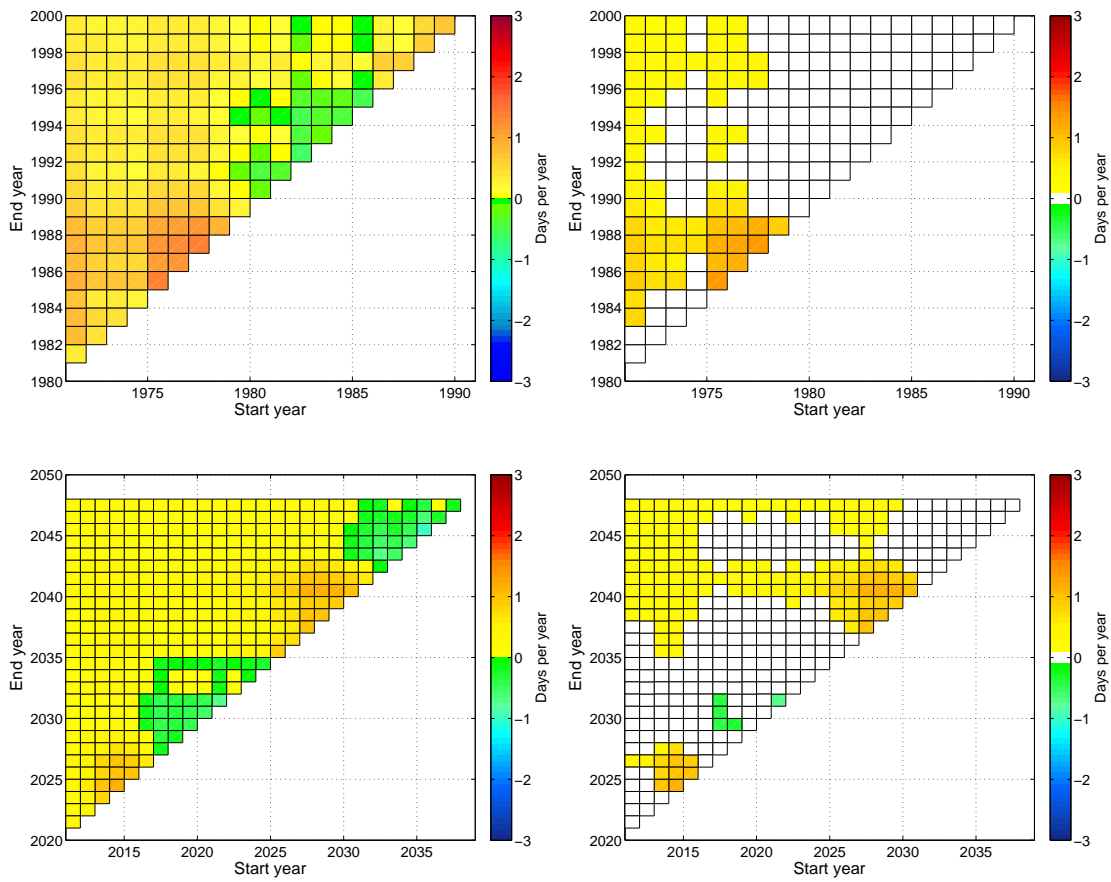


Figure 5.10: Trend matrices and significance of the ensemble for C20 (top) and the future projections (bottom).

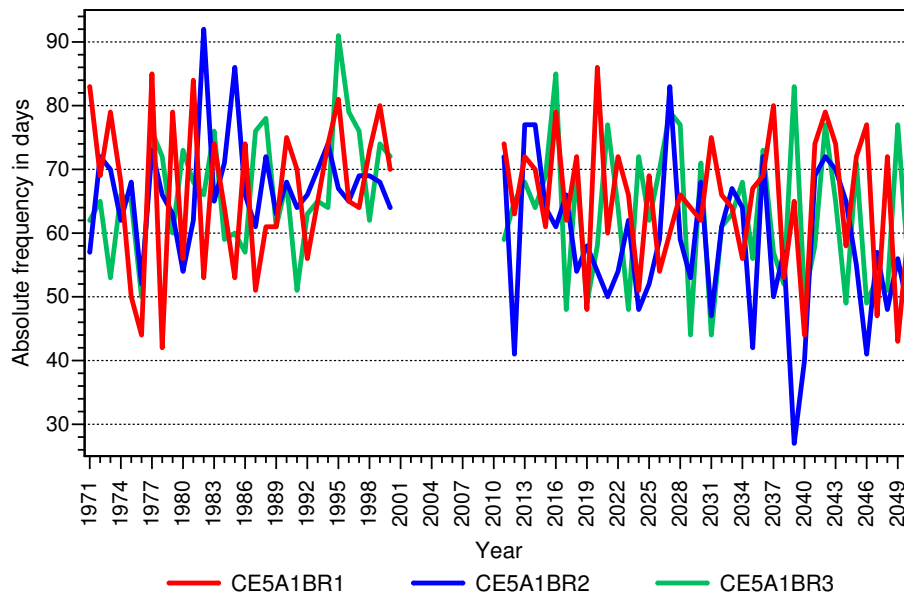


Figure 5.11: Absolute frequency of hail-unrelated WTs derived from CE5C20R1/CE5A1BR1 (red), CE5C20R2/CE5A1BR2 (blue) and CE5C20R3/CE5A1BR3 (green).

Trends of hail-unrelated WTs, derived from the CCLM-KL data, are similar to those of the hail-related WTs, but are reverse and more distinct, especially for the first run (Fig. 5.12; Appendix D.6). Positive trends in the subsequences of the time series from 1971/2000 until 2050 remain significant throughout the entire time period and the subsequences. But those trends are probably misleading as they are due to an abrupt decrease of hail-unrelated WTs between 1993 and 2001 from approximately 70 days to roughly 35 days (Fig. 5.13). None of the CCLM-ECHAM5 runs indicate such a decrease in hail-unrelated days. To determine which of the parameters in the oWLK leads to this decreased number of WTs between 1993 and 2001, the distributions of the vorticity (not shown) as well as the PW values are compared (Fig. 5.14). Time blocks of 8 years within the control period are chosen to compare the distributions of the values of the CCLM-KL runs, but also to evaluate what differences appear in one of the other model realizations (CCLM-ECHAM5 or CCLM-CCma3). The green line in Fig. 5.14 represents a period with the minimum of hail-unrelated WTs in CKLC20R1, while the other two periods 1977-1984 (blue) and 1985-1992 (red) represent an average occurrence of these WTs. As evident, the PW is much higher for the years 1993 to 2000 by up to 30% of the median compared to the other periods (1977-1984: 18.8 mm; 1993-2000: 26.6 mm). This increase of the PW is not evident in WTs from CKLC20R2. The reasons for this large discrepancy in the CCLM-KL model run are not clear, as the model physics and the forcing GCM are the same for all three time periods. Additionally, an overproportionate amount of water in the CCLM-KL cannot be confirmed by other studies, for example, in the precipitation study over Baden-Württemberg by Feldmann et al. (2010).

The second run of the CCLM-KL (Fig. 5.12) shows negative trends of hail-unrelated WTs for the same periods, where positive trends for the hail-related WTs were detected. The linear trend for the entire period from 1971 to 2048 amounts to 14 days for WTs derived from CKLA1BR2 and 11 days for those from CKLB1R2. These trends are very similar, but reverse, in comparison to the trends analyzed for the hail-related WTs. This is interesting as it reveals that hail-related WTs and hail-unrelated WTs depend on each other, at least statistically over longer periods. Even if there are 31 remaining types that were considered neither as hail-related nor as hail-unrelated, there seems to be a direct relationship between the occurrence of hail-related and -unrelated WTs. This is supported by the trend matrices of the remaining 31 WTs, where no significant trends are evident in the entire time periods (Appendix D.7). Hail-unrelated WTs derived from CCLM-CC3ma do not show noticeable significant trends.

In summary, almost the same conclusions as for the hail-related WTs can be drawn here. The largest differences in the trends are evident for the different model runs of the RCMs due to different initialization times and conditions. Second, the forcing global models cause differences, while for the CKLC20R1 the largest deviations are due to the unusual high PW values between 1993 and 2001. The emission scenarios have little influence on the sign of the trend but small influence on the overall number of hail-unrelated WTs per time period.

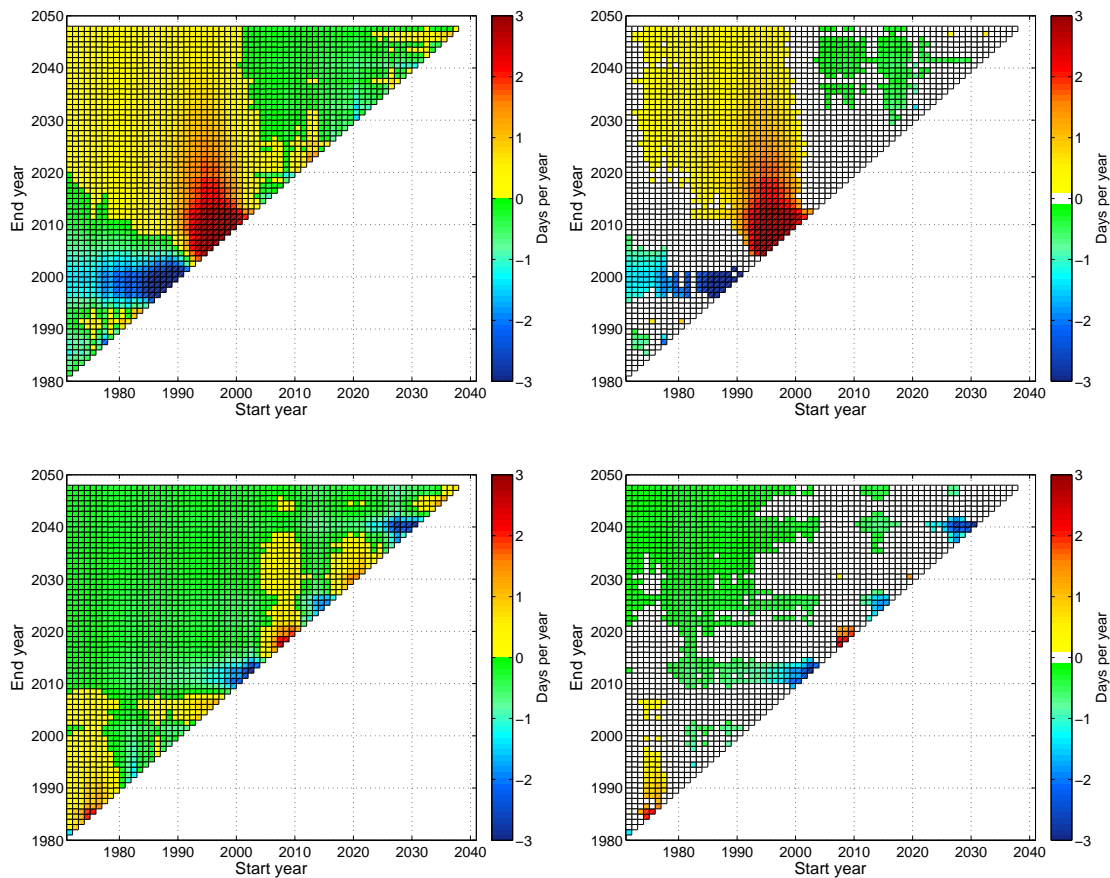


Figure 5.12: Trend matrices of hail-unrelated WTs from CKLC20R1/CKLA1BR1 (top) and CKLC20R2/CKLA1BR2 (bottom) from 1971 to 2048. Right panels show the corresponding significant trends.

### 5.2.2 Detection of periodicities

As discussed for the hail-related WTs, short-term variability of hail-unrelated WTs are apparent in the trend matrices as well, but less pronounced but statistically significant over several periods. Similar to the hail-related WTs, also those with infrequent hail occurrence were analyzed for periodicity (Fig. 5.15). Especially the spectrum for WTs derived from CC3A1BR1 (Fig. 5.12, bottom, right) shows that no harmonic behavior with a period of approximately 12 to 16 years is evident. However, there is an increased variance for shorter periods between 2.5 and 3 years, which was not detectable for the hail-related WTs by CC3A1BR1. Thus, the statement about the direct relationship between hail-related and hail-unrelated WTs needs to be softened, as this would imply that they hold the same harmonic behavior. Thus, this hypothesis is apparently not valid for the CC3A1BR1.

Nearly all other model realizations show an enhanced variance for the same periods as found for hail-related WTs, but the variance is less pronounced (Fig. 5.15). This result was expected as it was already visible in the trend matrices. It indicates that there is some periodic behavior in the

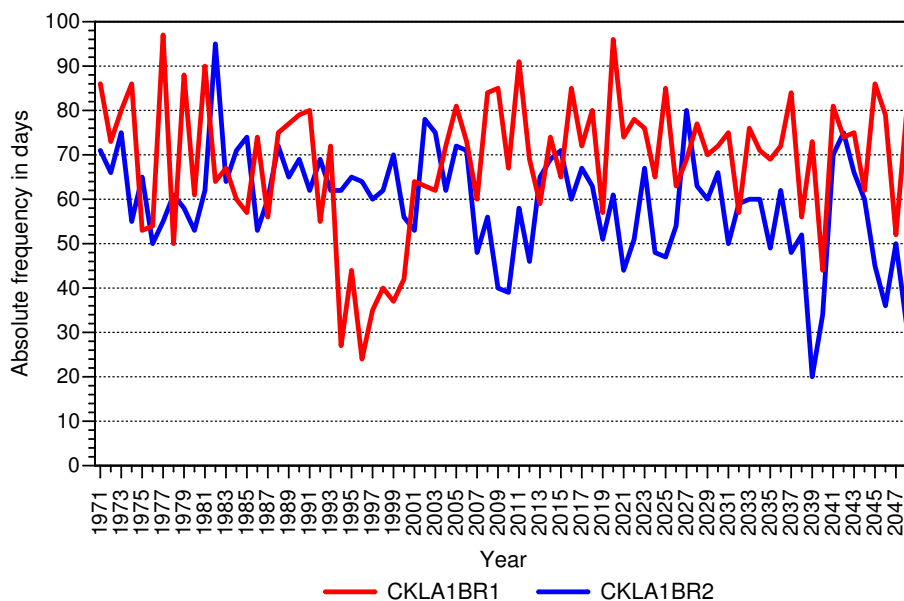


Figure 5.13: Absolute frequency of hail-unrelated WTs per summer half-year according to CKLC20R1/CKLA1BR1 (red) and CKLC20R2/CKLA1BR2 (blue) from 1971 to 2048.

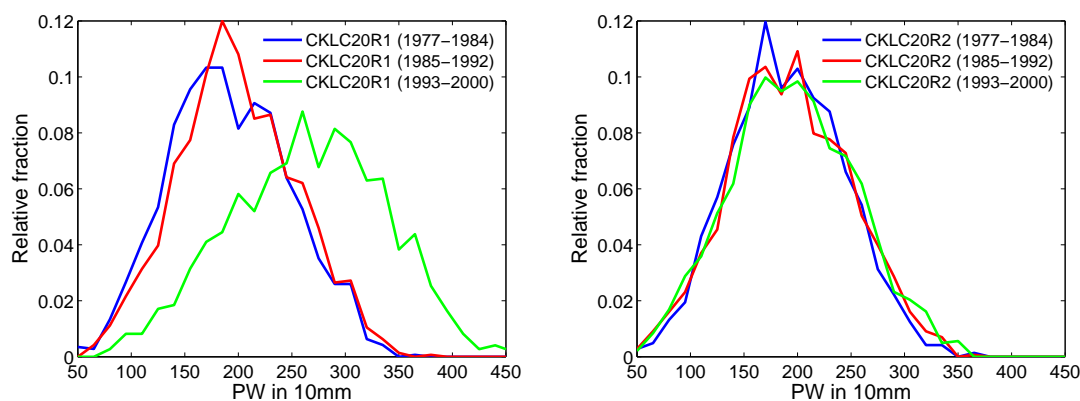


Figure 5.14: Distributions of PW for three sequenced time periods of 8 years from CKLC20R1 (left) and CKLC20R2 (right). Blue: 1977-1984; Red: 1985-1992; Green: 1993-2000.

time series of hail-unrelated WTs, but it probably interferes more with non-harmonic oscillations. For the CCLM-KL realizations the direct relationship between hail-related and hail-unrelated WTs can be confirmed. In years with less hail-related WTs, the number of hail-unrelated WTs increases, instead of the number of remaining 31 WTs.

### 5.2.3 Variability of hail-unrelated weather types in an ensemble of regional climate models

Finally, to account for epistemic uncertainty, the ensemble mean of the different RCM realizations is analyzed for the hail-unrelated WTs in accordance to the hail-related WTs (Par. 5.1.3). The average number for hail-unrelated WTs in the control period is  $66 \pm 9$  days, while a minimum

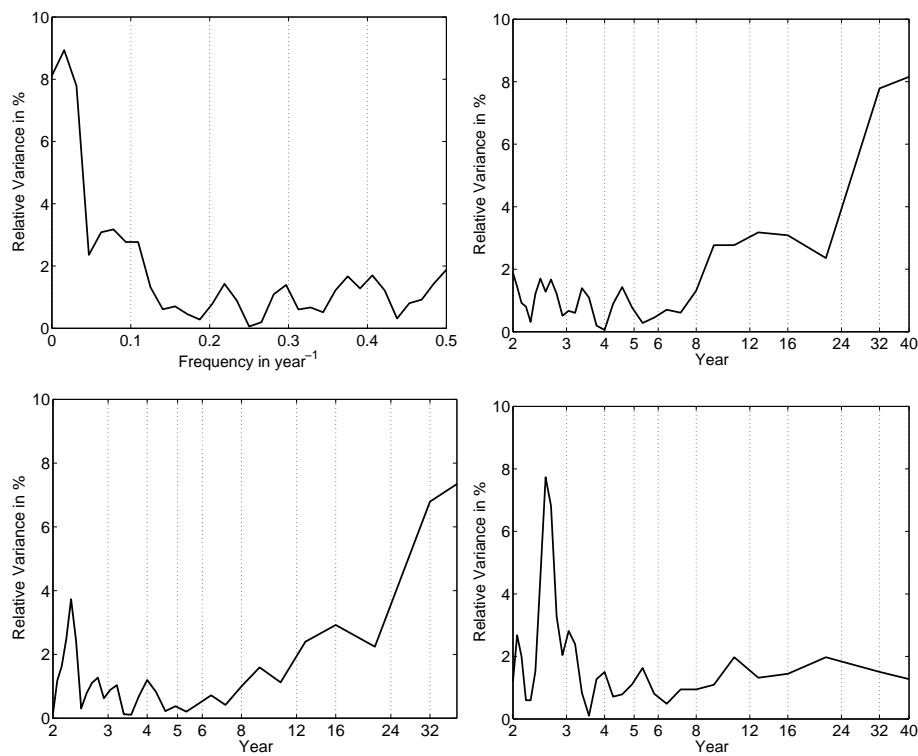


Figure 5.15: Frequency spectra of the autocorrelation function of hail-unrelated WTs. Top: CKLB1R1 as a function of frequency (left) and year (right); Bottom: CKLA1BR1 (left) and CC3A1BR1 (right) over time.

of 49 days is reached in 1976 and a maximum of 80 days in 1971 (Fig. 5.16). This indicates that the number of hail-unrelated WTs fluctuates a lot for the control period, especially in the 1970s (Fig. 5.16). From the year 1980 a decreasing number of days until the year 2000 is evident (Fig. 5.17, top). The large standard deviation (up to 45%) in the late 1990s is due to the minimum number of hail-unrelated WTs according to CKLA1BR1, as discussed at the beginning of this section.

The future projection period starts with a higher number of days, where these WTs prevail. An increase is visible until 2040, where the number of hail-unrelated WTs achieves its minimum of  $48 \pm 16$  days. A standard deviation of more than 30% indicates large differences between the RCM realizations and, thus, a high uncertainty. The trend matrices (Fig. 5.17) confirm these characteristics. The control period holds significant negative trends for the entire time period, but not for periods ending prior to 1994, where large fluctuations occur. The trends amount between -0.4 days (1971-2000) and -2.2 days (1989-1999) per year. A decrease of 12 days is observed for the years 1971 to 2000. A decrease of the hail-unrelated WTs implies that there is more potential for the occurrence of more days with severe thunderstorms. Due to the large number of remaining WTs where hail occurrence might be possible and due to the high uncertainty, no quantitative statement can be made about an increase in the number of hail damage days.

For the future projections, statistically significant trends are very rare (Fig. 5.17, bottom). This can be ascribed to the high annual variability, particularly to the high number of hail-unrelated WTs in 2041 and 2042. Even though the values seem abnormally high ( $\approx 5$  days), the very small standard deviations of roughly 5% indicate a low uncertainty since all models considered show almost the same results. Considering this finding, the trends are significant for either the entire time series or mainly periods that do not include those two years. For example, a decrease of 7 days is evident from 2011 to 2048 and 11 days for 2011 to 2040.

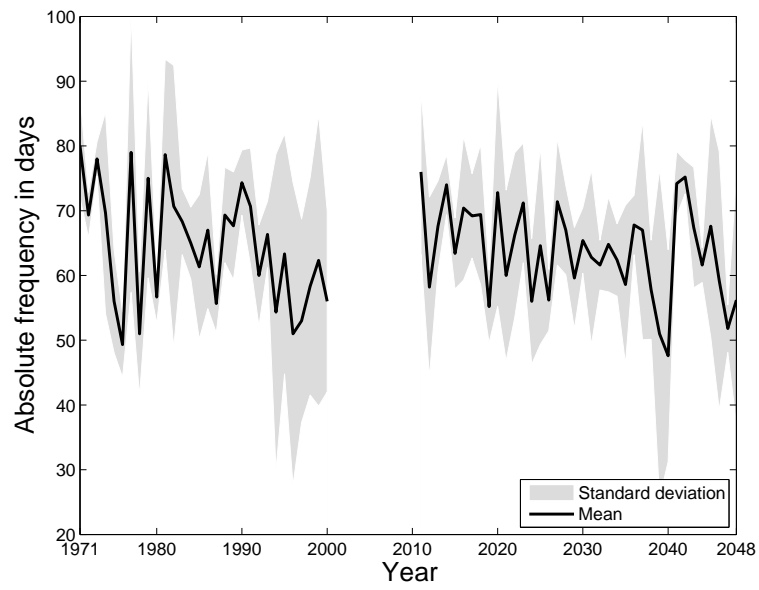


Figure 5.16: Same as Fig. 5.9 but for hail-unrelated WTs.

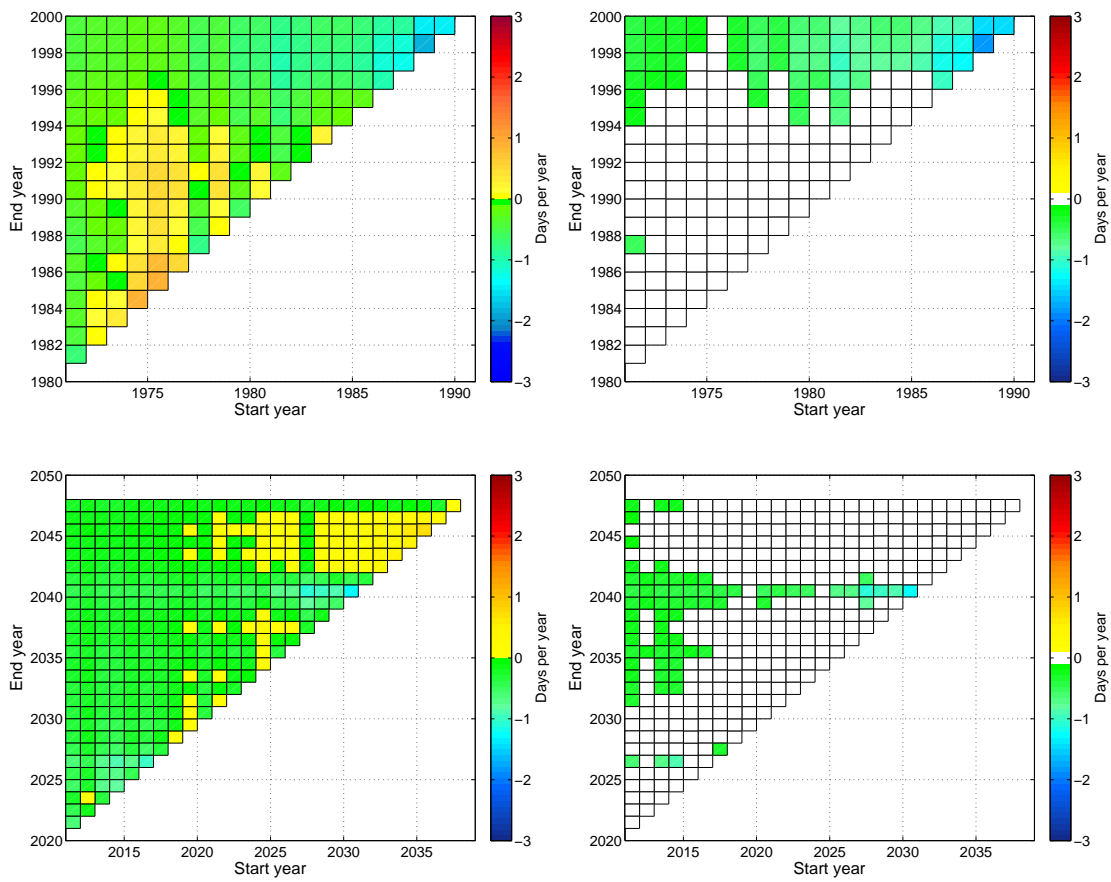


Figure 5.17: Same as Fig. 5.10 but for hail-unrelated WTs.



# 6. Statistical modeling of hail damage days

The statistical probability model, introduced in Paragraph 3.3.4, is used on the one hand to verify the results of categorical verification, in terms of the HSS, and on the other hand, it is used as a predictor for the number of hail damage days based on the derived WT from different climate models. One advantage of the model is that all WTs are considered and not just the four hail-related WTs discussed in previous chapters. Furthermore, the uncertainty in the predictions of hail damage days is properly accounted for. In this section, the potential for hail damage day occurrence will be discussed, according to all 40 WTs of oWLK.

## 6.1 Determination of hail damage day probabilities

To derive the number of hail damage days, the probabilities of damage causing hailstorms occurrence during a certain WT have to be derived first. For this, the statistical model is used. The output of the statistical model is a distribution for each probability  $p_i$  of hail damage occurrence during the  $i$ -th WT. A summary of these distributions and their 95% prediction intervals are shown in Figure 6.1. Red markers show the fraction of hail damage days according to the SV insurance data during each WT (further referred to as empirical values) derived from CCLM-ERA40 (1986-2000; see Fig. 4.3). Black markers indicate the point estimates for the probabilities  $p_i$  derived from the statistical model, and the brackets show the corresponding 95% prediction intervals. This diagram illustrates that the model gives very good estimates for the probabilities  $p_i$  as all empirical values are within the 95% prediction interval. Note that just 38 WTs are displayed, as two WTs never occurred in the past, according to CCLM-ERA40. The model confirms the results of the categorical verification and indicates that the four WTs SWCAW, SWCCW, SWAAW and XXCAW are most likely accompanied by damage causing hailstorms with a probability between 10% and 25%. Furthermore, the statistical model seems to confirm that not considering the WT SECAD (cf. Sec. 4.1) as hail-related WT is justified. The WT occurs only 11 times in total and is accompanied twice by hail and, thus, the absolute fraction of hail damage occurrence is  $\approx 18\%$ . However, this rare occurrence of the WT implies a high statistical uncertainty, which is well described by the model. The point value for  $p_i$  is statistically smaller than the empirical value and afflicted with high uncertainty according to the 95% prediction interval.

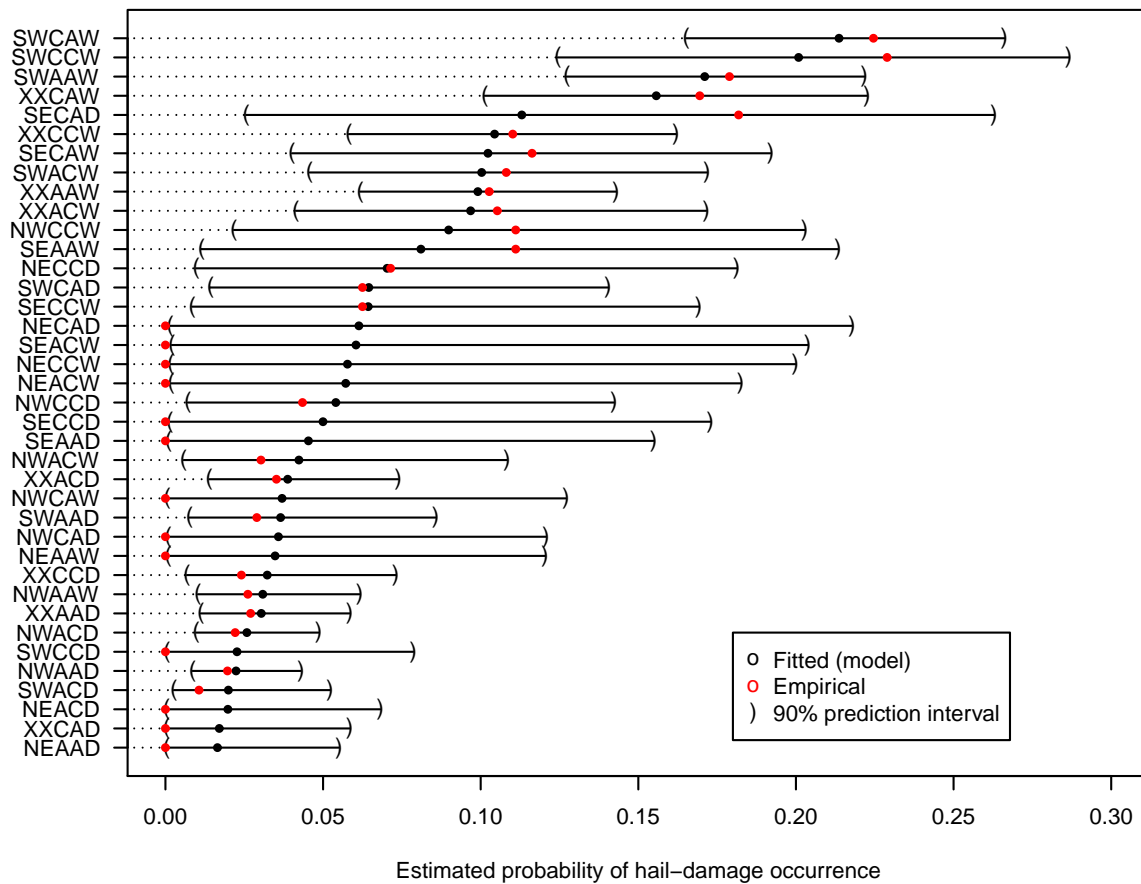


Figure 6.1: Point estimates (black dots) and 95% prediction intervals for the probabilities  $p_i$  of having hail during days with the  $i$ -th WT. The estimates are computed from WTs derived from CCLM-ERA40 and hail damage days of the SV data. Red points indicate empirical probabilities, derived from the same data sets.

But the model also has some problems. Especially those WTs with an empirically large  $p_i$  are under-predicted, meaning that the point estimates for the probabilities are lower for the model predictions than they are for the empirical values. Similarly, WTs that are not accompanied by hail and have an empirical  $p_i$  of zero are over-predicted.

## 6.2 Prediction of hail damage days

A great advantage of the statistical model is that it is possible to statistically predict the number of hail damage days from it by using the time series of all WTs. For predicting the WTs derived from the reference model CCLM-ERA40, reanalysis and climate models (cf. Table 3.1) are used to count the number of days where each WT prevailed ( $N_i$ ). Second, for each  $i$ , one sample for  $p_i$  is drawn and  $K = 200$  values from the binomial distribution  $B(N_i, p_i)$  are sampled. These processes are repeated  $S = 200$  times, which gives a good approximation for the predictive distribution of the number of hail damage days  $H$  for each WT. The sampling of the  $p_i$  ( $S$ ) in-

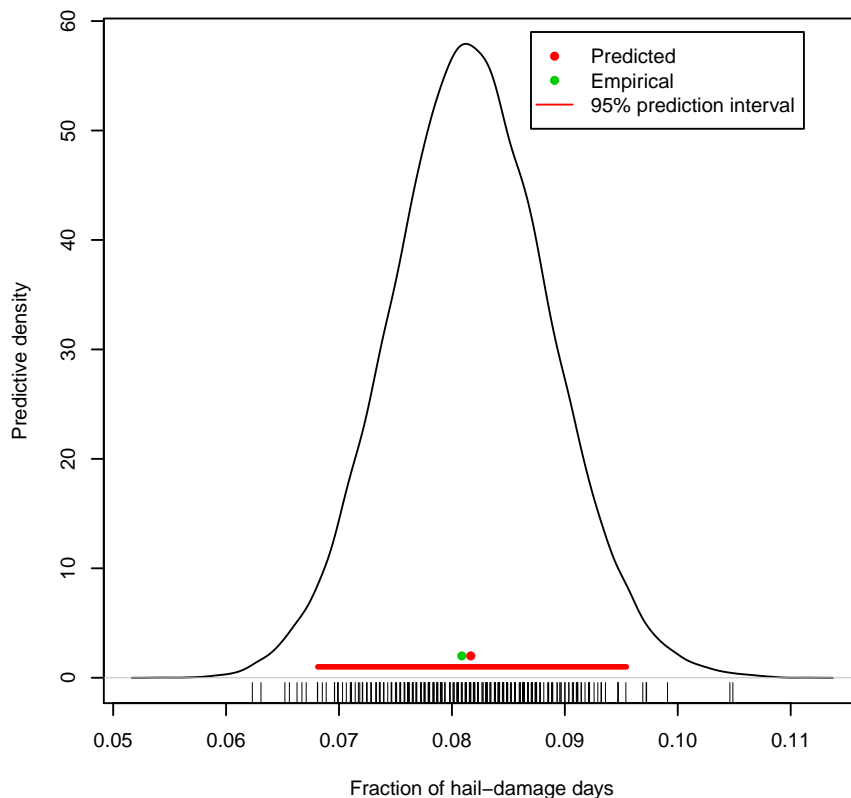


Figure 6.2: Predictive distribution for the fraction of hail damage days derived from CCLM-ERA40 during the observed record of the SV loss data (1986-2000). The 95% prediction interval is shown in red and the point estimate and the empirical value are shown as red and green dots, respectively (Vitolo and Economou, 2011, not published).

incorporates the epistemic uncertainty in the estimation of  $p_i$ , while the sampling of the distribution ( $K$ ) represents the aleatory uncertainty of hail-generating processes.

### Validation of the statistical model

To determine how well the model fits with observations, the predictive distribution of hail damage days derived from CCLM-ERA40 is compared with the empirically observed values. For this, all 38 samples with the number of hail damage days for each WT  $H_i$  are incorporated to one predictive distribution. Dividing this by the total number of days results in a distribution of the frequency of hail damage days as shown in Fig. 6.2. The frequency of hail damage days between the statistical model and the empirically derived frequency conform very well. Hence, statistically there is a chance between approximately 7% to 9% that damage causing hailstorms occur during a summer day in the federal state of Baden-Württemberg, which is on average approximately 15 days per summer half-year.

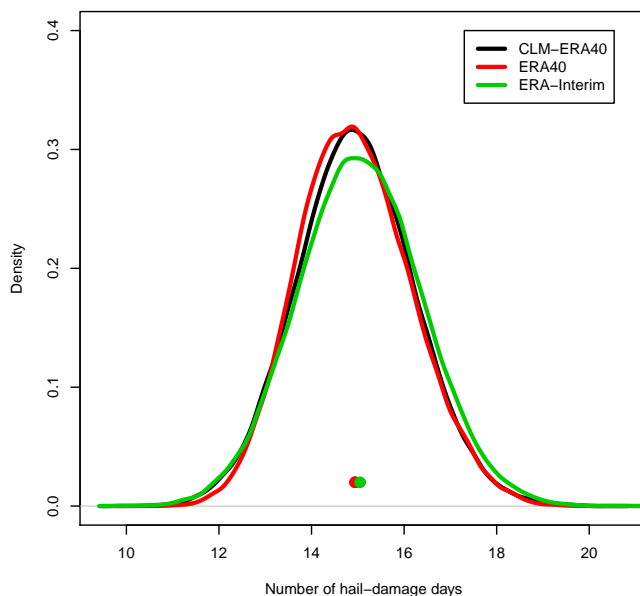


Figure 6.3: Number of hail damage days per year (1986 to 2000) according to the statistical model. Black: hail damage days derived by WTs of CCLM-ERA40; Red: ERA40; Green: ERA-Interim.

### Validation of CCLM-ERA40 derived hail damage days

For prediction of the number of hail damage days, a consideration of the WTs that never occurred in the CCLM-ERA40 (SEACD, NECAW) is necessary, as those could occur in the ERA40/ERA-Interim reanalyses or in the different climate models (see below). Thus, their probabilities are sampled from the overall, unconditional distribution of the hail damage days (cf. Fig. 6.2). To derive the number of hail damage days, the probabilities  $p_i$  and the occurrence of each WT  $N_i$  are used as input for the model. Finally, the probabilities are used to derive the number of hail damage days per summer half-year. Figure 6.3 shows the predictive distributions of the hail damage days per year for the period 1986 to 2000 derived by WTs from the ERA40 and ERA-Interim reanalysis and the CCLM-ERA40. The accordance of the hail damage days is remarkable and confirms that the CCLM-ERA40 is an appropriate model, when considering WTs applied to the frequency of hailstorms. All data sets give an approximate number of 15 hail damage days per year, which is in very good agreement to the number of hail days according to the SV data (15 days). All models indicate that there is a high probability (>90%) of having more than 13 hail damage days and less than 17 days per year.

### Prediction of hail damage days in climate models

To evaluate whether the climate models (Table 3.1) are capable to reproduce the WTs and hence, the same number of hail damage days for the past decades, the distributions of the number of hail damage days are computed for the model realizations CKLC20R1, CKLC20R2 and CC3C20R1

Table 6.1: Values used for the bias correction of the predictive distributions of the number of hail damage days shown in Fig. 6.4 (and in the Appendix E.2).

Model realization	Number of hail damage days
CKLC20R1	-0.7
CKLC20R2	+0.4
CC3C20R1	+1.4
CE5C20R1	+0.7
CE5C20R2	+0.9
CE5C20R3	+0.9

as well as for CCLM-ECHAM5 (Appendix E.2). According to Table 6.1 (top), largest deviations to the CCLM-ERA40 results are evident for CC3C20R1, while the deviations between the different model runs are again largest for the forcing global model (CC3C20R1 vs. CKLC20R1) and the initial conditions (CKLC20R1 vs. CKLC20R2). The reasons of the differences in the distributions are due to both epistemic and aleatory uncertainty. Unfortunately, due to the gap in the time series of the other RCM realization, no statement can be made in respect to the regional models. To predict the number of hail damage days that can be expected in the future, a bias correction for the three different model realization towards the CCLM-ERA40 distribution is accomplished. For this, the distributions of the RCM realizations are shifted by the amounts in Table 6.1. After applying this correction, it is possible to evaluate future changes in the probability of hail damage days and to consider the bias of the statistical model in regards to the bias of the climate model realizations.

The computation of the distributions of hail damage days for the entire future projection period (2001 to 2048) indicates that the CKLA1BR2, CC3A1BR1 (Fig. 6.4), CKLB1R2 (not shown) and CE5A1BR1-R3 (Appendix E.2) show an increase in the number of days, while the CKLA1BR1 (and CKLB1R1; not shown) indicates a decrease. This is very interesting as a positive trend for the hail-related WTs was also observed in the trend matrices (Fig. 5.1 in Sec. 5.1). This raises the question why there is an expected decrease in the number of hail damage days when considering all WTs of the CKLA1BR1.

In Figure 6.4, the distributions for CKLA1BR1, CKLA1BR2 and CC3A1BR1 are split into three different time periods with a length of 15 years each, which was chosen according to the 15 year observation period of the SV data. For the years 2001-2015, the distribution of CKLA1BR1 indicates a significant smaller number of hail damage days compared to the other model realizations and to the number of days in the past (1986-2000). This reveals that the future projection of this model realization seems to have a different distribution of those WTs that are mainly forcing hail development, while this difference is not reflected within the control period. The differences are also not visible in the trend matrices, because a positive trend in the number of hail damage days is also obvious in the distributions for the periods 2016-2030 and 2031-2045. Those shifts towards a decreased number of hail damage days are probably induced by an increased number of

hail-related WTs in the late 1990s (Fig. 5.1.1), which have significant influences on the trends. Similar shifts are evident for CE5C20R2 and CE5C20R3 (Appendix E.2), but due to the lack of data between 2001 and 2010 there is a potential for misinterpretation. However, those realizations show a tendency to a higher number of hail damage days in the projections for the future.

For the time period from 2001-2015, CKLA1BR2 and CC3A1BR1 indicate a probability of more than 90% that the number of hail damage days per summer half-year exceeds 13 days, which conforms to CCLM-ERA40 in the control period (1986-2000). As mentioned already, the probability of having more than 13 days according to CKLA1BR1 is much smaller and amounts to values of approximately 20%. For the next period of 15 years (2016-2030; Fig. 6.4 bottom, left) all means of the distributions indicate an increase in the number of days from at least 13 hail damage days (1986-2000; 2001-2015) up to a minimum of 15 days. The probability of having more than 14 hail damage days according to CKLA1BR2 is still more than 90%. This rapid increase is probably caused by the 'step' in the time series of hail-related WTs, as explained in Section 5.1. Note that only the minimum number of hail damage days according to the 90% probability of hail occurrence is discussed. The variance of the distribution is much larger and amounts to values of approximately 7 days. Thus, a larger number of hail damage days can also be expected to a certain probability.

In the period from 2031 to 2045 (Fig. 6.4, bottom right) positive trends in the number of hail damage days are evident again in all model realizations. According to CC3A1BR1, CKLA1BR2 and CE5A1BR1-R3, the probability of having more than 14 damage days per summer half-year is more than 90%. For the CKLB1R1 and CKLB1R2 model realizations similar results are achieved, but not shown. Table 6.2 summarizes the findings.

Table 6.2: Minimum number of days during which hail damage can be expected with a 90% probability derived from the statistical model and different climate model realizations. All values are corrected for a systematic bias according data of CCLM-ERA40 and for the control period 1986-2000.

Model realization	1986-2000	2001-2015	2016-2030	2031-2045
CKLA1BR1	13	10	10	11
CKLA1BR2	13	13	13	15
CC3A1BR1	13	13	14	14
CE5A1BR1	13	-	13	14
CE5A1BR2	13	-	14	15
CE5A1BR3	13	-	14	14

The results of the statistical modeling of hail damage days confirm that the analysis of the four selected hail-related WTs already gives a good estimate about the variability of hail damage events. However, the use of this method has some advantages. The analysis shows that even if the control periods (1986 to 2000) conform well to both reanalysis and climate models, there are remarkable differences in the future projections of the climate models (CKLA1BR1, CE5A1BR2,

CE5A1BR2) that affect the number of hail-related WTs per year and, hence, the number of hail damage days. Those can be attributed to aleatory uncertainty, as differences are mainly due to the different initialization times and initial conditions of the forcing global climate model. However, with an increase of approximately one to two days in the number of hail damage days, the results are similar to those of the analysis of hail-related WTs. This indicates that the periodicity and temporal variability of the four chosen hail-related WTs is probably a good estimate for the actual occurrence of hail damage days.

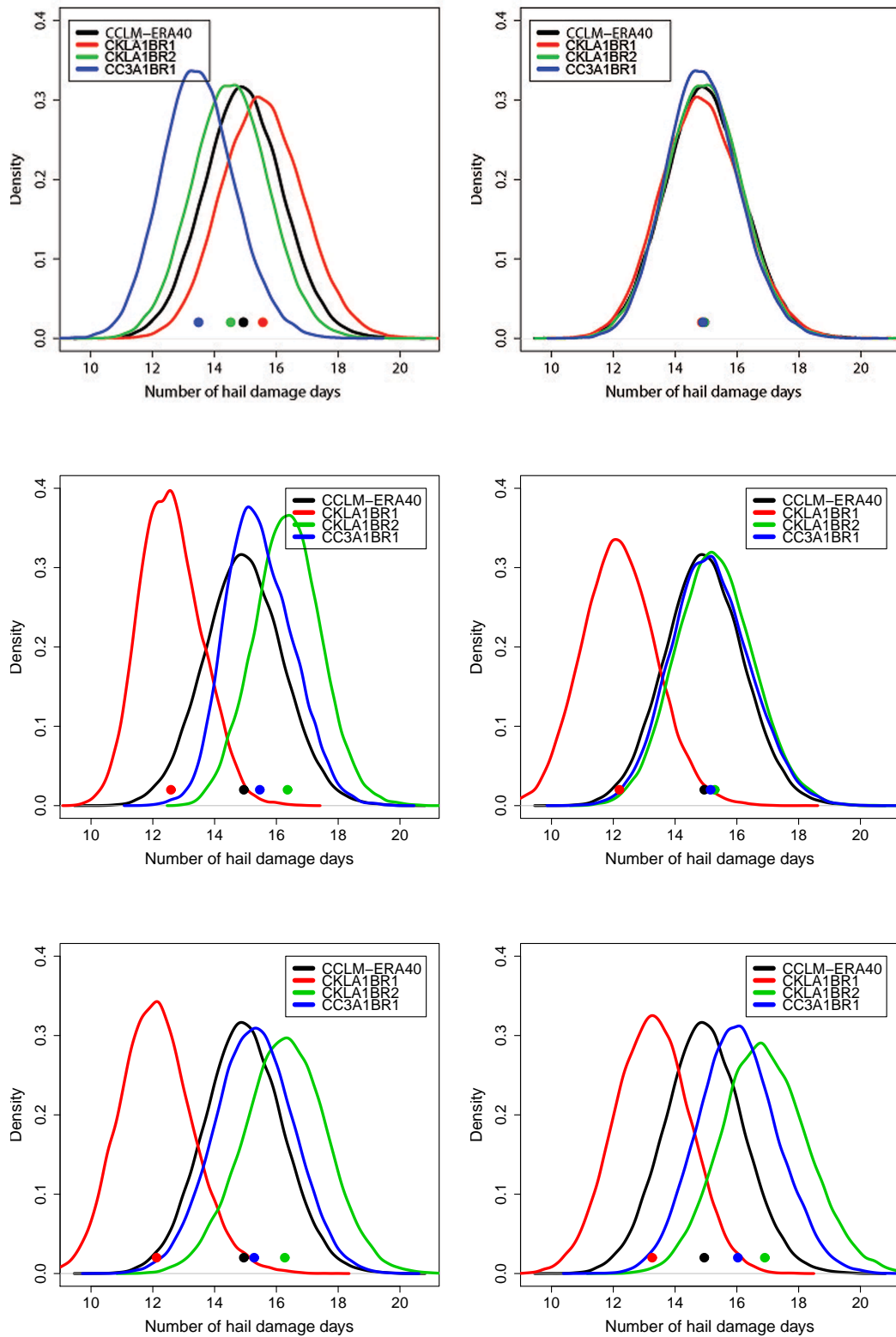


Figure 6.4: Predictive distributions of the number of hail damage days derived from CCLM-ERA40 for the time period from 1986 to 2000 (black) and CCLM-KL for 1986-2000 (top), 2001-2048 (middle, left), 2001-2015 (middle, right), 2016-2030 (bottom, left) and 2031-2045 (bottom, right). A bias correction is applied to all RCM realizations during the control runs (top, right).

## 7. Summary and conclusion

In this thesis the long-term variability of weather patterns which are frequently accompanied by damage causing hailstorms is analyzed. In order to accomplish this, the first step is to examine the applicability of the weather type classification method (oWLK) of Deutscher Wetterdienst (DWD) to different climate model data. The second step is to verify whether the climate models are able to reproduce weather types (WTs) properly. These steps are essential to analyze the variability of WTs over the longest possible time period.

To clarify these questions, reanalysis data of the ECMWF (ERA40 and ERA-Interim) and dynamically downscaled data of the regional climate model (RCM) CCLM-ERA40 for the control period C20 (1971 to 2000) were available. The CCLM-ERA40 data were driven by initial and boundary conditions of ERA40. Furthermore, data of eight different realizations of the regional climate model COSMO-CLM were used. They were available for C20 and different future projection periods (2001-2048/2050 and 2011-2050). The RCM realizations differ by the version of COSMO-CLM (3.1 and 4.8), the driving global climate model (ECHAM5-MPI/OM, CCCma3), the initialization time and initial conditions of the global climate model (Run 1 to 3) and the emission scenarios (A1B and B1). The oWLK are applied to all of these data sets for the investigation area of Germany (4°E to 16°E and 45°N and 57°E) and WTs are derived.

Using categorical verification allowed to link loss data from the SV SparkassenVersicherung AG, which include claims of hail damage on buildings in Baden-Württemberg, and derived WTs. In doing so, it is possible to differentiate between weather patterns that are frequently accompanied by damaging hailstorms (hail-related WTs) and those that are only rarely accompanied by hail (hail-unrelated WTs), which are the basis for the analysis of variability.

The applicability of the classification method is examined by comparing the distributions of the absolute frequency of WTs derived from ERA40, ERA-Interim and CCLM-ERA40 for C20. The deviations between the distributions are only minor, indicating that the application of the oWLK to similar data sets (all contain observations) leads to similar results. Hence, different model resolutions of ERA40 ( $\approx 125$  km), ERA-Interim ( $\approx 80$  km) and CCLM-ERA40 ( $\approx 50$  km) do not have much influence on the resulting WTs. However, the main reason for differences in the WT distributions is the flow direction ( $< 8\%$ ) as shown by comparing the distributions of the individual parameters in the oWLK (flow direction, relative vorticity and humidity). Furthermore it is found that the classification method is found to reach its limits when classifying indifferent weather conditions, e.g., an accumulated relative vorticity that is close to zero. These indifferent WTs

might also impact the results of the oWLK, but are probably equally distributed in all models and, hence, the effects are relatively small.

According to the evaluation, the WTs derived from CCLM-ERA40 were considered as reference to categorize into hail-related and hail-unrelated WTs. Using the Heidke Skill Score (HSS) allowed to define four WTs that have a high probability to be accompanied by damaging hailstorms and five WTs where hailstorms are very rare. Interestingly, three of the hail-related WTs turned out to be referable to the same meteorological process: warm and moist air advected from the Atlantic and Mediterranean leading to a frequent occurrence of thunderstorms as the advected air mass stores a lot of energy ("Spanish plume"). The fact that three WTs can be related to the same process indicates that the oWLK cannot differ between different meteorological processes. But it clarifies that the WTs that favor the development of damaging hailstorm determined from the HSS are realistic. These findings are in agreement to the analyses by Bissolli et al. (2007), who found a relationship between three of the detected WTs and the occurrence of tornadoes in Germany.

To examine whether the annual variability of hail-related WTs is independent of the model and the model resolution, the absolute frequency of hail-related WTs derived by ERA-40, ERA-Interim, CCLM-ERA40 and WTs derived by the DWD is compared. Deviations of the annual frequency of WTs for C20 in general remain small (<5%) except for a few particular years. Deviations for hail-unrelated WTs are slightly larger (<10%). This indicates that the model resolution also has a minor influence on the variability of hail-related WTs.

As the applicability of the classification method to different data sets is confirmed, the method is applied to the mini-ensemble of climate model realizations. Since the RCMs are not driven by observations, they cannot be compared for the temporal succession of the synoptic fields. Thus, only the statistical distribution of WTs over an adequate long time-period of the 30 years in the C20 is compared with WTs derived from CCLM-ERA40. The overall distributions of WTs derived from climate models are approximately identical to those of the reference model. Deviations are mainly due to the classification of the flow direction and the cyclonality in 500 hPa, which is sensitive for indifferent WTs as discussed above. However, it is interesting that mainly the cyclonality in 500 hPa causes differences as it is not as influenced by the lower boundary conditions as the cyclonality in 1000 hPa and would, thus, be assumed to be less erroneous. However, the good correspondence between climate models and reanalysis emphasizes that the oWLK is applicable to a various type of data sets. This indicates that the oWLK is a good basis for the analysis of the natural variability of the hailstorm occurrence and allows to consider long time periods that are not available for hail observations.

Linear trends in the time-series of hail-related WTs are examined by using trend matrices where both the start and end year of the series are successively varied. The significance (80% significance level) of linear trends is tested using Mann-Kendall test statistics. Significant positive trends for C20 of approximately 9 days are found in the hail-related WTs derived from CKLA1BR1 and

CKLB1R1, while trends are not significant for the remaining model realizations. For the future projections three of the eight model realizations show significant positive trends of approximately 11 days (2001-2048/50) and 8 days for CE5A1BR1 (2011-2050). Furthermore, the periodic behavior of hail-related WTs is determined by the application of a Fast Fourier Transformation to those time series with an adequate length (not CCLM-ECHAM5). Nearly all hail-related WTs derived from the model realizations show a periodic behavior of 12-16 and 2-5 years. This indicates that the potential for hail follows a certain harmonic behavior. The derived trends are highly dependent on the initialization time and the initial conditions of the driving GCM, which caused the largest differences of the WTs. Second largest differences are due to the forcing GCM (ECHAM5 and CCCma3). The RCM model versions (3.1 and 4.8) and emission scenarios (A1B and B1) are just of minor importance. The differences between these model realizations indicate a large uncertainty of the climate scenarios. Furthermore, it explains why the eight climate projections should not be considered as climate prediction, but more as an estimate of the potential development of the climate with regard to hail-related WTs.

To summarize the potential development of hail-related WTs and to account for epistemic uncertainty, the time series of hail-related WTs derived from the different model realizations are combined to one ensemble with mean and standard deviation. The trend matrices show that short-term trends are mostly not statistically significant, due to large inter-annual variability of hail-related WTs. However, significant long-term trends are found in the past and future. A significant increase of 12 days (from 35 to 47 days) is observed between 1971 and 2000 and an increase of 9 days (39 to 46 days) for the years 2011-2048. These could partially explain the increase of damage days observed by the SV insurance company ( $\approx$  15 days). This would indicate that the results are representable, even though thunderstorms cannot be resolved.

However, the detected changes should be interpreted with care as they are only derived from one RCM. Due to the lack of three-dimensional data from different RCMs the changes cannot be traced back to natural variability. Additionally, different initialization times for CCLM-CCCma3 and scenarios for CCLM-CCCma3 and CCLM-ECHAM5 would increase the number of ensemble members and, thus, would make the analysis of linear trends more stable against a shift in the initialization time.

To verify the results, the number of hail damage days is computed with a statistic probability model based on the WTs from the climate models. This is the first time that hail damage days are derived from time series of WTs using such a model. The comparison of the statistically derived number of hail damage days on basis of WTs derived from CCLM-ERA40, ERA40 and ERA-Interim conformed very well with the empirical derived number of days according to the SV loss data. An approximate number of 15 hail damage days was found within the period from 1986 to 2000, while the distributions allow to quantify that there is a probability of more than 90% to have between 13 and 17 hail damage days. The application of the probability model to different RCM realizations allows to make statements of significant changes in the number of hail damage days in the future. To reduce epistemic uncertainty in the RCM simulations, the number of hail damage days is corrected for bias. The future projections show that an increase in the number of

hail damage days can be expected. For three of the model realizations there is a probability of 90% that at least 15 hail damage days per summer-half year occur between 2031-2045 and for three others that at least 14 hail damage days occur. Surprisingly, some of the model realizations indicate a shift in the probability distribution of the hail damage days between 1986-2000 and 2001-2015 towards a decreasing number of days, even if the data are bias corrected. This can be related to peaks in the time series that significantly influence the trends. It should be further analyzed if these deviations are caused by a certain periodicity or just due to peaks.

The analyses shows that it is possible to apply the oWLK to different data sets and that the RCM realizations reproduce the overall number of hail-related WTs surprisingly good. Applying different statistical methods makes it possible to investigate likely future changes of damaging hailstorms. Hence, the methods could be applied to study WTs that are in some way related to other meteorological phenomena, e.g. tornadoes (Bissolli et al., 2007) or flooding (Bardossy and Filiz, 2005). This would allow to estimate the probability of such extreme events in future decades. However, the analysis also shows that nearly all statements are afflicted with high uncertainty. Hence, further investigations should include a larger ensemble of RCMs to reduce the epistemic uncertainty. This assures that natural variability is analyzed and not only the model physics. An ensemble should preferably include a large number of RCMs that are driven by different global climate models, as most uncertainties were found to originate from those.

# A. Weather types

Table A.1: List of Hess-Brezowksy Major types (GWT) and types (GWL; Hess and Brezowsky, 1952; Gerstengarbe and Werner, 2005)

Major type (GWT)	Abbrev.	Type (GWL)	Abbrev.
<b>A. Zonal circulation</b>			
West	W	West cyclonic	WZ
		West anticyclonic	WA
		West angular	WW
		Southern West	WS
<b>B. Mixed circulation</b>			
Central Europe high	HM	Central European high	HM
		Central European ridge	BM
Central European low	TM	Central European low	TM
Southwest	SW	Southwest anticyclonic	SWA
		Southwest cyclonic	SWZ
Northwest	NW	Northwest anticyclonic	NWA
		Northwest cyclonic	NWZ
<b>C. Meridional circulation</b>			
East	E	Fennoscadian high anticyclone	HFA
		Norwegian Sea/Fennoscadian high anticyclone	HNFA
		Fennoscadian high cyclonic	HFZ
		Norwegian Sea/Fennoscadian high cyclonic	HNFZ
South	S	South anticyclone	SA
		South cyclonic	SZ
		British Isles low	TB
		Western Europe trough	TRW
Southeast	SE	Southeast anticyclone	NA
		Southeast cyclonic	SEZ
North	N	North anticyclone	NA
		North cyclonic	NZ
		North, Iceland high, anticyclonic	HNA
		North, Iceland high, cyclonic	HNZ
		British Isles high	HB
		Central European trough	TRM
Northeast	NE	Northeast anticyclone	NEA
		Northeast cyclone	NEZ

Table A.2: List of objective weather types by the DWD

<b>Abbrev.</b>	<b>Advection</b>	<b>Cyclonality in 925 hPa</b>	<b>Cyclonality in 500 hPa</b>	<b>Humidity</b>
NEAAD	Northeast	anticyclonic	anticyclonic	dry
NEAAW	Northeast	anticyclonic	anticyclonic	wet
NEACD	Northeast	anticyclonic	cyclonic	dry
NEACW	Northeast	anticyclonic	cyclonic	wet
NECAD	Northeast	cyclonic	anticyclonic	dry
NECAW	Northeast	cyclonic	anticyclonic	wet
NECCD	Northeast	cyclonic	cyclonic	dry
NECCW	Northeast	cyclonic	cyclonic	wet
SEAAD	Southeast	anticyclonic	anticyclonic	dry
SEAAW	Southeast	anticyclonic	anticyclonic	wet
SEACD	Southeast	anticyclonic	cyclonic	dry
SEACW	Southeast	anticyclonic	cyclonic	wet
SECAD	Southeast	cyclonic	anticyclonic	dry
SECAW	Southeast	cyclonic	anticyclonic	wet
SECCD	Southeast	cyclonic	cyclonic	dry
SECCW	Southeast	cyclonic	cyclonic	wet
SWAAD	Southwest	anticyclonic	anticyclonic	dry
SWAAW	Southwest	anticyclonic	anticyclonic	wet
SWACD	Southwest	anticyclonic	cyclonic	dry
SWACW	Southwest	anticyclonic	cyclonic	wet
SWCAD	Southwest	cyclonic	anticyclonic	dry
SWCAW	Southwest	cyclonic	anticyclonic	wet
SWCCD	Southwest	cyclonic	cyclonic	dry
SWCCW	Southwest	cyclonic	cyclonic	wet
NWAAD	Northwest	anticyclonic	anticyclonic	dry
NWAAW	Northwest	anticyclonic	anticyclonic	wet
NWACD	Northwest	anticyclonic	cyclonic	dry
NWACW	Northwest	anticyclonic	cyclonic	wet
NWCAD	Northwest	cyclonic	anticyclonic	dry
NWCAW	Northwest	cyclonic	anticyclonic	wet
NWCCD	Northwest	cyclonic	cyclonic	dry
NWCCW	Northwest	cyclonic	cyclonic	wet
XXAAD	not defined	anticyclonic	anticyclonic	dry
XXAAW	not defined	anticyclonic	anticyclonic	wet
XXACD	not defined	anticyclonic	cyclonic	dry
XXACW	not defined	anticyclonic	cyclonic	wet
XXCAD	not defined	cyclonic	anticyclonic	dry
XXCAW	not defined	cyclonic	anticyclonic	wet
XXCCD	not defined	cyclonic	cyclonic	dry
XXCCW	not defined	cyclonic	cyclonic	wet

Table A.3: List of objective weather types by the modified weather type classification

<b>Abbrev.</b>	<b>Cyclonality in 925 hPa</b>	<b>Cyclonality in 500 hPa</b>	<b>Humid.</b>	<b>Stability</b>	<b>Equivalent potential temp.</b>
AADSH	anticyclonic	anticyclonic	dry	stable	high EPT (large scale lifting)
AADSL	anticyclonic	anticyclonic	dry	stable	low EPT (no lifting)
AADLH	anticyclonic	anticyclonic	dry	instable	high EPT
AADLL	anticyclonic	anticyclonic	dry	instable	low EPT
AAWSH	anticyclonic	anticyclonic	wet	stable	high EPT
AAWSL	anticyclonic	anticyclonic	wet	stable	low EPT
AAWLH	anticyclonic	anticyclonic.	wet	instable	high EPT
AAWLL	anticyclonic	anticyclonic	wet	instable	low EPT
ACDSH	anticyclonic	cyclonic	dry	stable	high EPT
ACDSL	anticyclonic	cyclonic	dry	stable	low EPT
ACDLH	anticyclonic	cyclonic	dry	instable	high EPT
ACDLL	anticyclonic	cyclonic	dry	instable	low EPT
ACWSH	anticyclonic	cyclonic	wet	stable	high EPT
ACWSL	anticyclonic	cyclonic	wet	stable	low EPT
ACWLH	anticyclonic	cyclonic	wet	instable	high EPT
ACWLL	anticyclonic	cyclonic	wet	instable	low EPT
CCDSH	cyclonic	cyclonic	dry	stable	high EPT
CCDSL	cyclonic	cyclonic	dry	stable	low EPT
CCDLH	cyclonic	cyclonic	dry	instable	high EPT
CCDLL	cyclonic	cyclonic	dry	instable	low EPT
CCWSH	cyclonic	cyclonic	wet	stable	high EPT
CCWSL	cyclonic	cyclonic	wet	stable	low EPT
CCWLH	cyclonic	cyclonic	wet	instable	high EPT
CCWLL	cyclonic	cyclonic	wet	instable	low EPT
CADSH	cyclonic	anticyclonic	dry	stable	high EPT
CADSL	cyclonic	anticyclonic	dry	stable	low EPT
CADLH	cyclonic	anticyclonic	dry	instable	high EPT
CADLL	cyclonic	anticyclonic	dry	instable	low EPT
CAWSH	cyclonic	anticyclonic	wet	stable	high EPT
CAWSL	cyclonic	anticyclonic	wet	stable	low EPT
CAWLH	cyclonic	anticyclonic	wet	instable	high EPT
CAWLL	cyclonic	anticyclonic	wet	instable	low EPT



## B. Skill Scores

### Hit Rate

The hit rate counts all correct forecasts and is defined as

$$H = \frac{a + d}{n}. \quad (\text{B.1})$$

The best possible hit rate is one, while the worst is zero. It considers all correct "Yes" and "No" forecasts but is not an adequate measure when observational events occur only rarely (see Wilks, 1995).

### Threat Score

The threat score (TS), also called critical success index (CSI), is equivalent to the number of correct "Yes" forecasts divided by the occasions on which the event was forecast and/or observed (Wilks, 1995):

$$TS = CSI = \frac{a}{a + b + c}. \quad (\text{B.2})$$

It can be interpreted as the quantity being forecast after removing correct "No" forecasts. It is used particularly when an event occurs less frequently than the nonoccurrence.

### Probability of detection

To include information about the likelihood, that the event would be forecasted relative to its occurrence, the probability of detection (POD) can be used as accuracy measure:

$$POD = \frac{a}{a + c}. \quad (\text{B.3})$$

For a perfect forecast its value achieves one and for the worst  $POD = 0$ .

### False Alarm Rate

The false-alarm rate (FAR) is the number of "Yes" forecasts of the event that fail and it is calculated as

$$FAR = \frac{b}{a + b}. \quad (\text{B.4})$$

In contrast to the other measures the best possible FAR is zero and the worst is one.

**Bias**

The bias (B) is not an accuracy measure but indicates whether an event was forecasted more frequently than it was observed. The B is the ratio of the number of "Yes" forecasts to the number of "Yes" observations:

$$B = \frac{a + b}{a + c}. \quad (\text{B.5})$$

If B is equal to one, the event was forecast the same number of times than it was observed. If it is greater than one, the event was forecast more often than observed (overforecast), while it was underforecast when B is less than zero.

## C. Modified weather type classification

Table C.1: Skill scores of hail-related and hail-unrelated WTs derived from CCLM-ERA40 with MoWLK.

	Weather type	POD	FAR	CSI	HSS	a	b	c	d
Hailstorm-related	CAWLH	0.257	0.601	0.185	0.266	57	86	165	2437
	AAWLH	0.207	0.681	0.144	0.2	46	98	176	2425
	CCWLH	0.041	0.625	0.038	0.058	9	15	213	2508
	CCWSH	0.054	0.844	0.042	0.04	12	65	210	2458
Hailstorm-unrelated	AAWSL	0.018	0.983	0.009	-0.073	4	235	218	2288
	AADSL	0.036	0.981	0.012	-0.092	8	423	214	2100
	ACDSL	0.045	0.979	0.015	-0.092	10	464	212	2059
	CCDSL	0.009	0.987	0.005	-0.06	2	152	220	2371



# D. Analysis of hail-related weather types

## D.1 Hail-related weather types

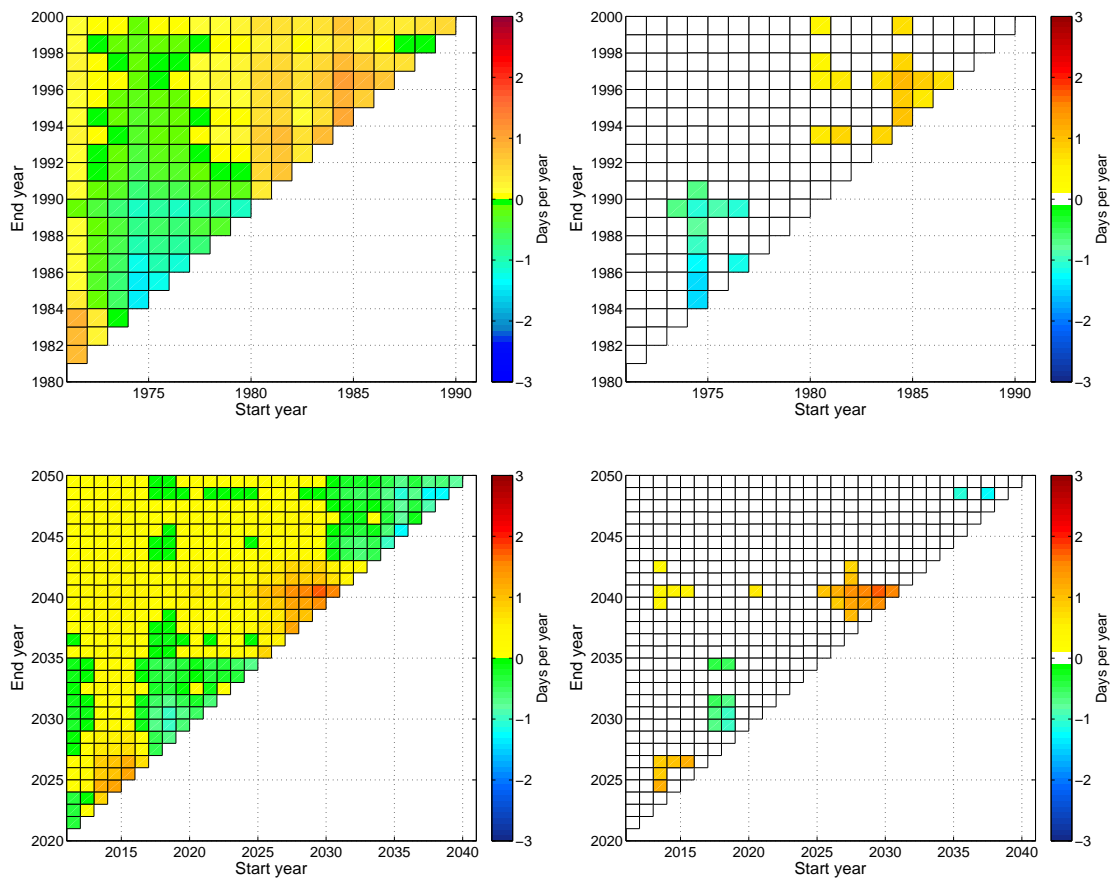


Figure D.1: Same as Fig. 5.2 but for CE5C20R2 (top) and CE5A1BR2 (bottom).

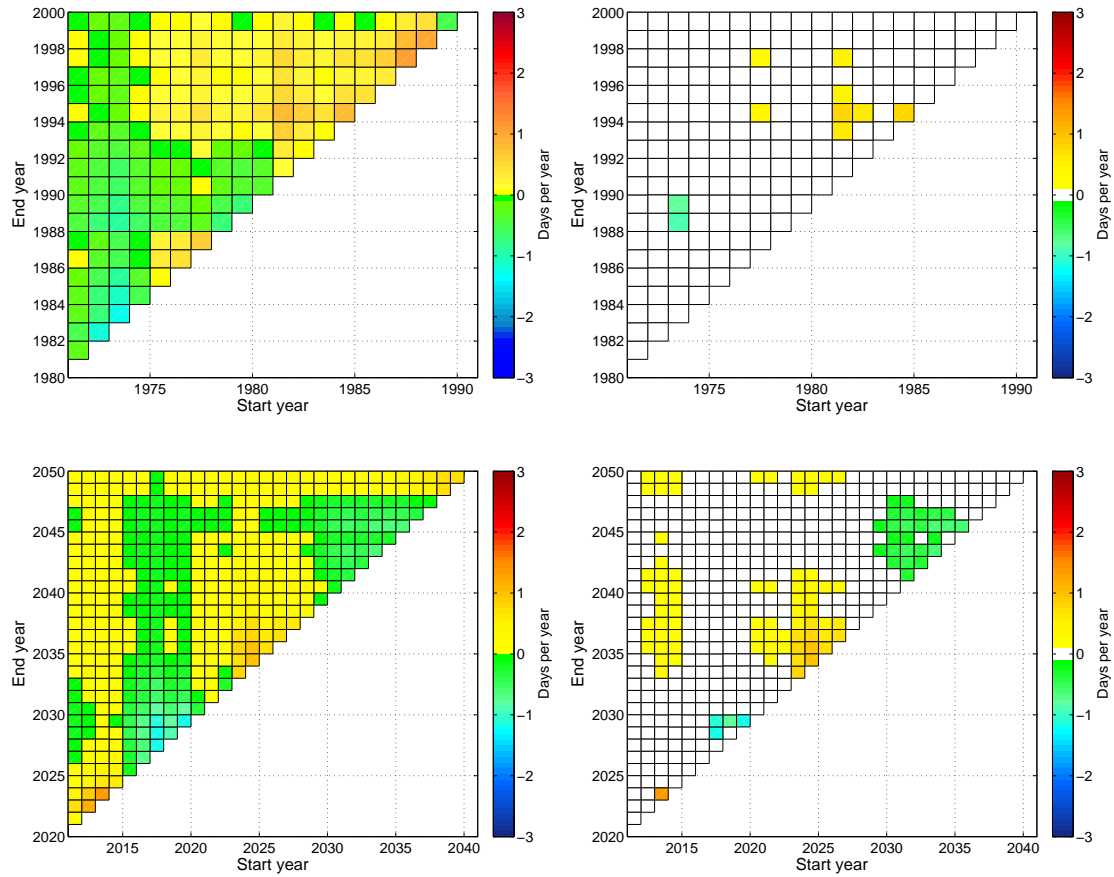


Figure D.2: Same as Fig. 5.2 but for CE5C20R3 (top) and CE5A1BR3 (bottom).

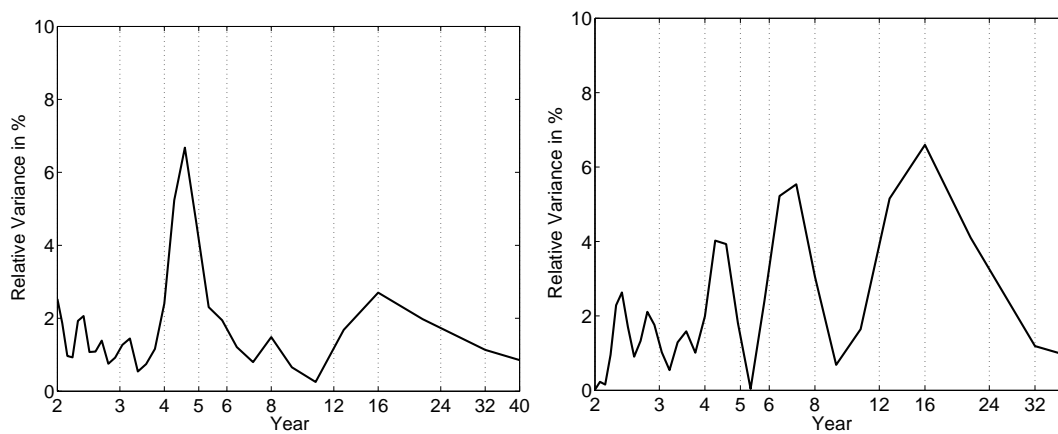


Figure D.3: Same as Fig. 5.8 but for CKLC20R2/CKLB1R2 (left) and CKLC20R2/CKLA1BR2 (right).

## D.2 Hail-unrelated weather types

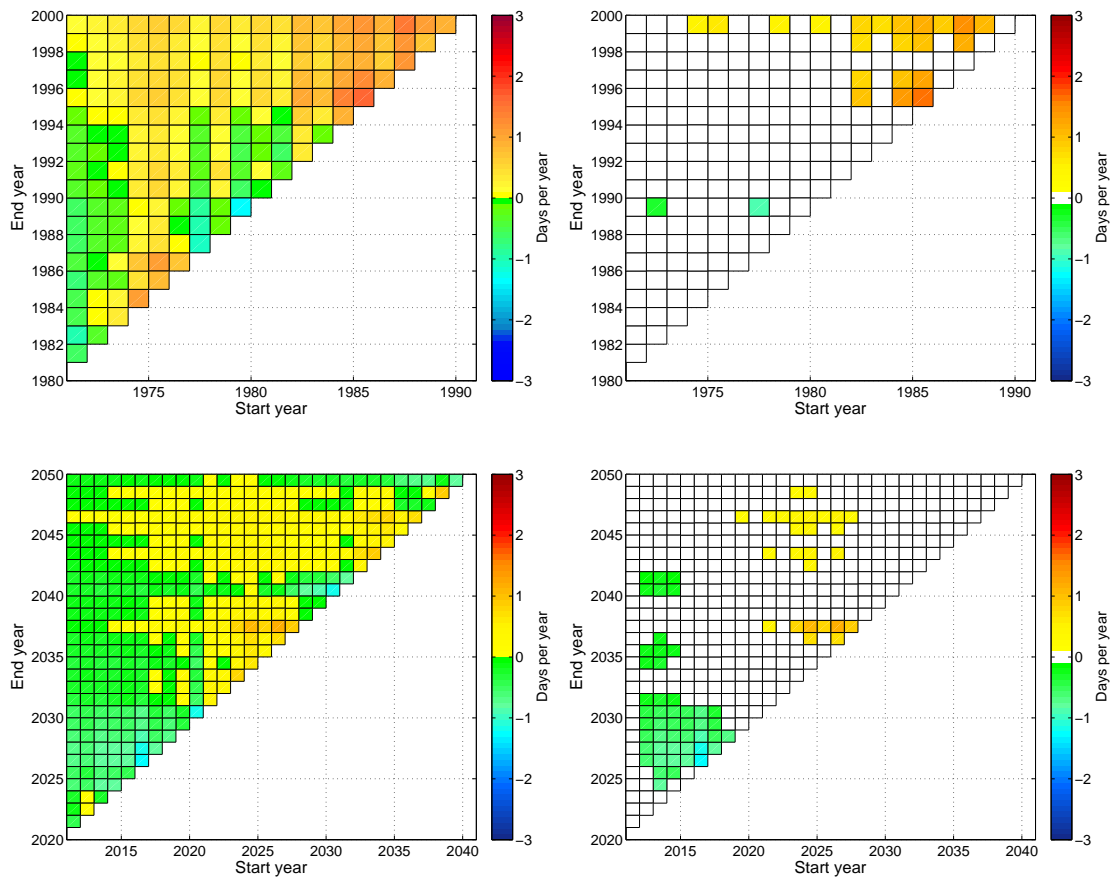


Figure D.4: Same as Fig. 5.2 but for CE5C20R1 (top) and CE5A1BR1 (bottom) and hail-unrelated WTs.

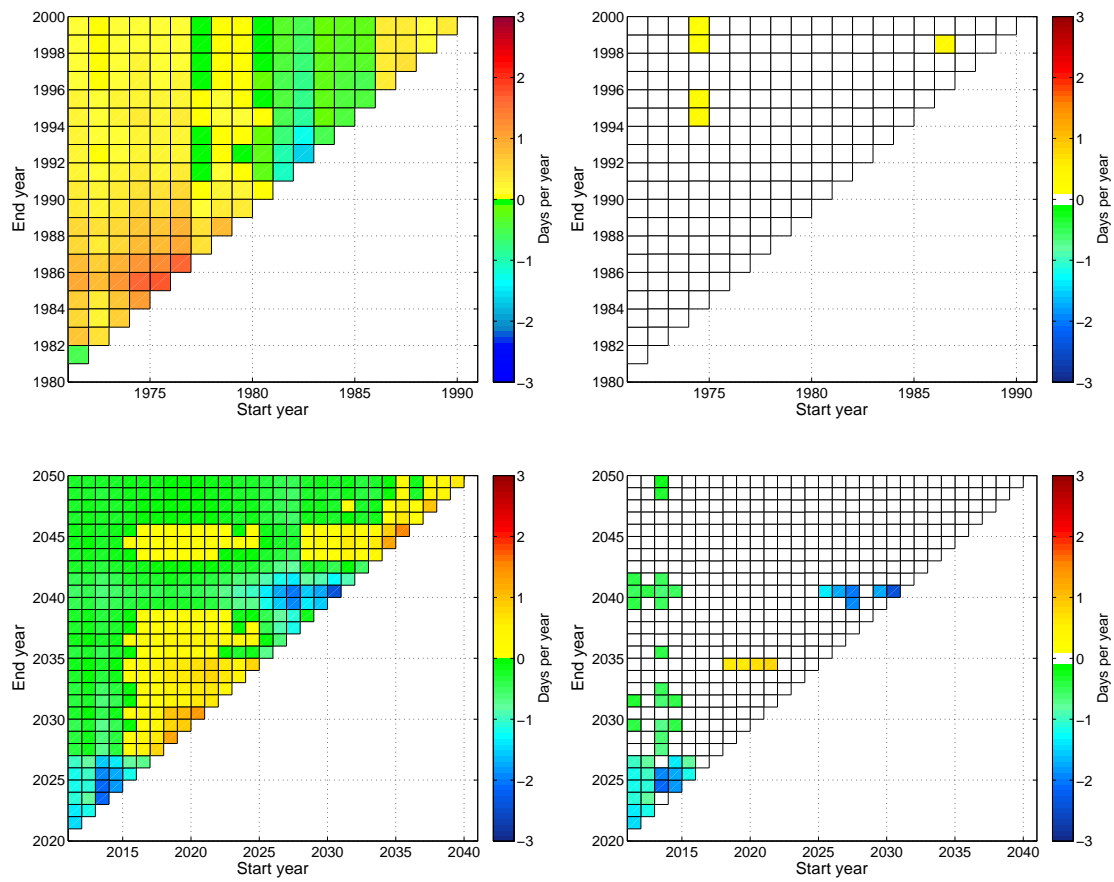


Figure D.5: Same as Fig. 5.2 but for CE5C20R2 (top) and CE5A1BR2 (bottom) and hail-unrelated WTs.

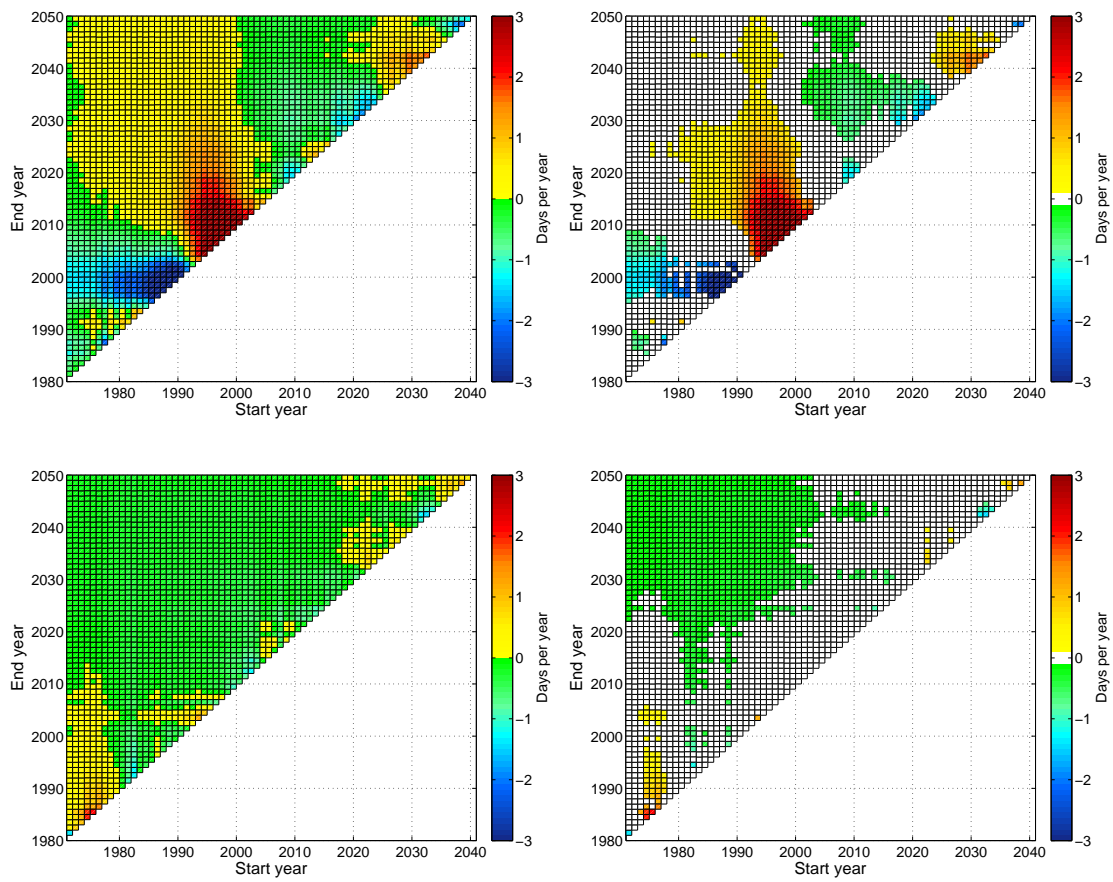


Figure D.6: Same as Fig. 5.2 but for CKLC20R1/CKLB1R1 (top) and CKLC20R2/CKLB1R2 (bottom) and hail-unrelated WTs.

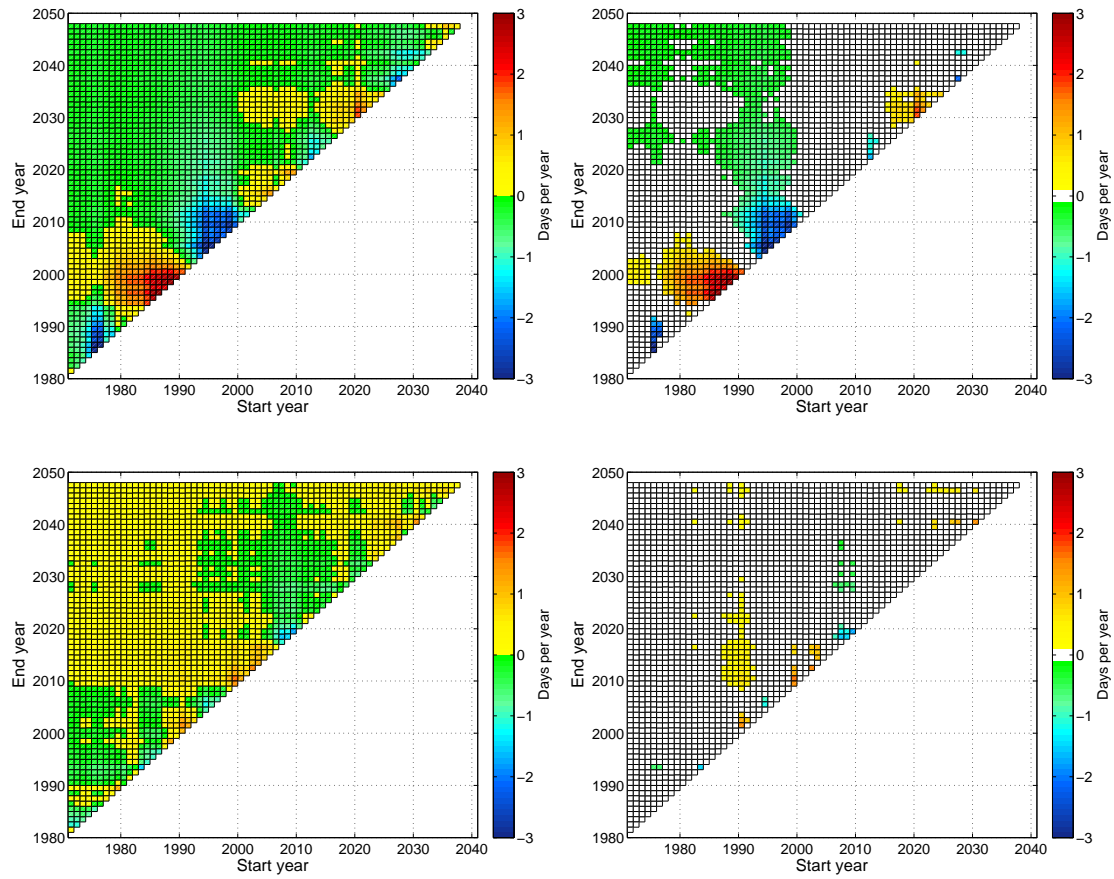


Figure D.7: Same as Fig. 5.2 but for CKLC20R1/CKLA1BR1 (top) and CKLC20R2/CKLA1BR2 (bottom) and remaining WTs.

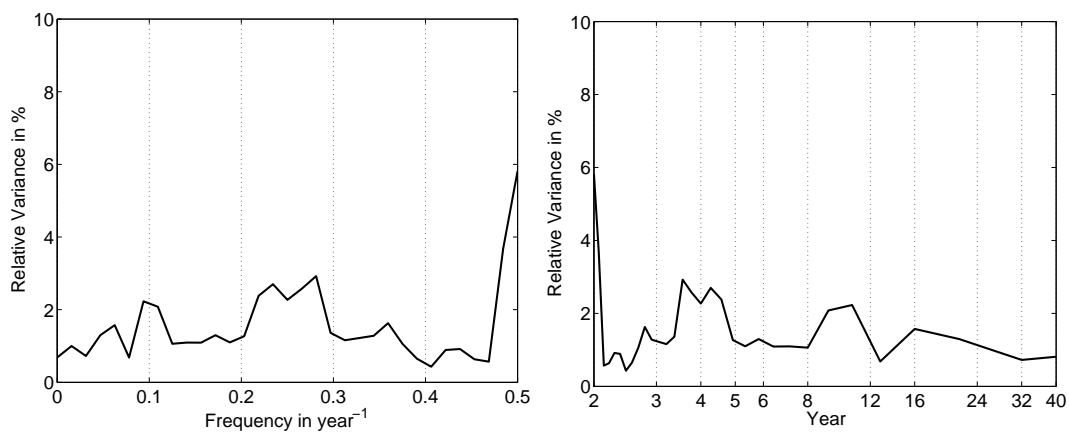


Figure D.8: Same as Fig. 5.15 but from CKLC20R2/CKLB1R2.

## E. Prediction of hail damage days

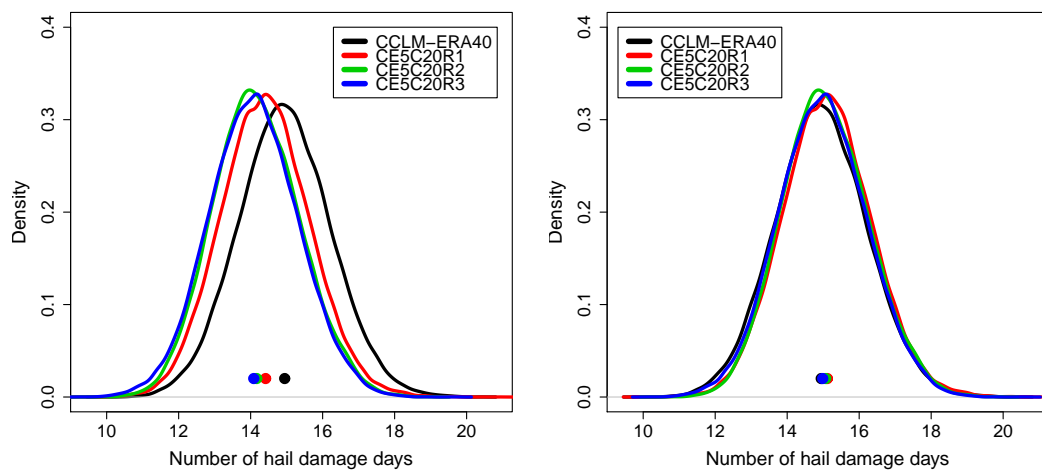


Figure E.1: Same as Fig. 6.4 but for the CCLM-ECHAM5 model runs and only for the control period 1986 to 2000 without (left) and with (right) bias correction.

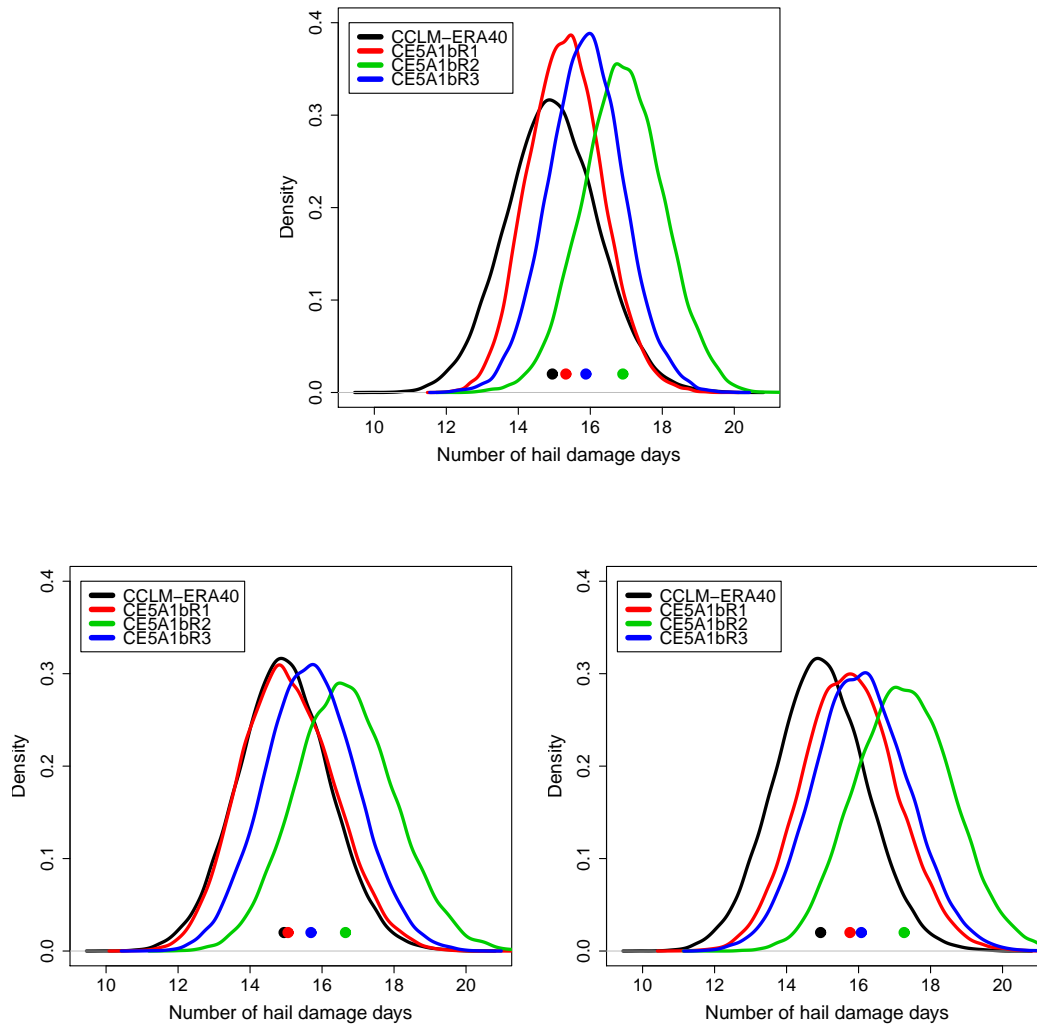


Figure E.2: Same as Fig. 6.4 but for the CCLM-ECHAM5 model runs and for the future projections 2011-2048 (top), due to the lag of data between 2001 and 2010.

# References

- Adrian, G. and D. Frühwald, 2002: Design der neuen Modellkette GME/LM. *Promet*, **27**, 3/4, 106–110.
- Bardossy, A. and F. Filiz, 2005: Identification of flood producing atmospheric circulation patterns. *J. Hydrol.*, **313**, 48–57.
- Barlow, W., 1993: A new index for the prediction of deep convection. *Preprints, 17th Conference on Severe Local Storms, 4-8 Oct. 1982, St. Louis, MO*, 129–132.
- Baur, F., 1947: *Musterbeispiele Europäischer Grosswetterlagen*. Dieterische Verlagsbuchhandlung.
- Bayazit, M. and B. Önöz, 2007: To prewhiten or not to prewhiten in trend analysis? *Hydrol. Sci. J.*, **52**, 611–624.
- Beheng, K., 2007: *Dynamik der Atmosphäre*. Skript zur Vorlesung WS 2007/2008 und SS 2008. Institut für Meteorologie und Klimaforschung, Universität Karlsruhe (TH). 221 pp.
- Bissolli, P. and E. Dittmann, 2001: The objective weather type classification of the German Weather Service and its possibilities of application to environmental and meteorological investigations. *Meteorol. Z.*, **10**, 253–260.
- Bissolli, P., J. Grieser, N. Dotzek, and M. Welsch, 2007: Tornadoes in Germany 1950–2003 and their relation to particular weather conditions. *Global Planet. Change*, **57**, 124–138.
- Bluestein, H. B. and C. R. Parks, 1983: A synoptic and photographic climatology of low-precipitation severe thunderstorms in the Southern Plains. *Mon. Weather Rev.*, **111**, 2034–2046.
- Brombach, J., 2010: *Analyse der räumlichen Variabilität der Konvektionsbedingungen aus hochaufgelösten Reanalysedaten*. Seminar thesis, Karlsruhe Institute of Technology. 25–32 pp.
- Cooley, J. W. and J. W. Tukey, 1965: An algorithm for the machine calculation of complex Fourier series. *Math. Comput.*, **19**, 297–301.
- Crook, N., 1996: Sensitivity of moist convection forced by boundary layer processes to low-level thermodynamic fields. *Mon. Weather Rev.*, **124**, 1767–1785.

- Doswell, C. I., R. Davies-Jones, and D. Keller, 1990: On summary measure of skill in rare event forecasting based on contingency tables. *Weat. Forecast.*, **5**, 576–585.
- Dutton, J. A., 1986: *The Ceaseless Wind: An Introduction to the Theory of Atmospheric Motion*. Dover Publications Inc., Dover.
- Ehmann, C., 2009: Analyse der vorherrschenden Großwetterlagen während Hagelereignissen in Baden-Württemberg. Seminar thesis, Karlsruhe Institute of Technology. 44-56 pp.
- Feldmann, H., B. Früh, C. Kottmeier, H.-J. Panitz, and G. Schädler, 2010: Hochauflösende regionale Simulationen künftiger Starkniederschläge in Baden-Württemberg (ReSiPrec). Final report, Karlsruhe Institute of Technology. 28-43 pp.
- Flato, G., G. Boer, W. Lee, N. McFarlane, D. Ramsden, M. Reader, and A. Weaver, 2000: The Canadian centre for climate modelling and analysis global coupled model and its climate. *Climate Dynam.*, **16**, 451–467.
- Galway, J., 1956: The lifted index as a predictor of latent instability. *Bull. Am. Meteorol. Soc.*, **37**, 528–529.
- Gerstengarbe, F. and P. Werner, 2005: Katalog der Großwetterlagen Europas (1881-2004) nach Paul Hess und Helmuth Brezowsky, 6. verbesserte und ergänzte Auflage. Report, Potsdam Institute for Climate Impact Research. 7-17 pp.
- Haklander, A. J. and A. V. Delden, 2003: Thunderstorm predictors and their forecast skill for the Netherlands. *Atmos. Res.*, **67-68**, 273–299.
- Heidke, P., 1926: Berechnung des Erfolgs und der Güte der Windstärkevorhersage im Sturmwarnungsdienst. *Ann. Geophys.*, **8**, 301–349.
- Hess, P. and H. Brezowsky, 1952: Katalog der Großwetterlagen Europas. *Ber. Dtsch. Wetterd. in der U.S.-Zone*, **33**, 39.
- Holton, J. R., 1972: *An Introduction to Dynamic Meteorology*. Academic Press, INC, 112 pp pp.
- Houze, R. A. J., 1993: *Cloud Dynamics*. Academic Press, INC, 570 pp pp.
- IPCC, 2007: *Climate Change 2007: The Physical Science Basis. Contribution of Working Group I to the Fourth Assessment Report of the Intergovernmental Panel on Climate Change [Solomon, S., Qin, D., Manning, M., Chen, Z., Marquis, M., Averyt, K. B., Tignor, M., and Miller, H. L. (eds.)]*. Cambridge University Press, Cambridge, United Kingdom and New York, NY, USA, 996 pp.
- Kendall, M., 1975: *Rank Correlation Methods*. Griffin, London.
- Kraus, H., 2004: *Die Atmosphäre der Erde. Eine Einführung in die Meteorologie*. Springer-Verlag, Berlin.

- Kunz, M., 2007a: The skill of convective parameters and indices to predict isolated and severe thunderstorms. *Nat. Hazard Earth Syst. Sci.*, **7**, 327–342.
- Kunz, M., C. Hauck, and C. Kottmeier, 2006: Meteorologische Naturgefahren. Skript zur Vorlesung. 53-99 pp.
- Kunz, M. and M. Puskeiler, 2010: High-resolution assessment of the hail hazard over complex terrain from radar and insurance data. *Meteorol. Z.*, **19**, 427–439.
- Kunz, M., J. Sander, and C. Kottmeier, 2009: Recent trends of thunderstorm and hailstorm frequency and their relation to atmospheric characteristics in southwest Germany. *Int. J. Climatol.*, **29**, 2283–2297.
- List, R., 1958a: Kennzeichen atmosphärischer Eisparkel, 1. Teil. *Angew. math. Phys.*, **9a**, 180–192.
- List, R., 1958b: Kennzeichen atmosphärischer Eisparkel, 2. Teil. *Angew. math. Phys.*, **9a**, 217–234.
- Maddox, R. A., 1980: Mesoscale Convective Complexes. *Bull. Am. Meteorol. Soc.*, **61**, 1374–1387.
- Mann, H. B., 1945: Nonparametric tests against trend. *Econometrica*, **13**, 245–259.
- Mayer, H., D. Schindler, M. Kunz, and B. Ruck, 2010: Strategien zur Reduzierung des Sturm-schadenrisikos für Wälder (Abschlussbericht Verbungsprojekt RESTER). 17-57 pp.
- McFarlane, N., J. Scinocca, M. Lazare, R. Harvey, D. Versegny, and J. Li, 2005: The CCCma third generation atmospheric general circulation model. Tech. rep., CCCma Internal Rep., 25 pp.
- Miller, R., 1972: Notes on analysis and severe storm forecasting procedures of the Air Force Global Weather Central. Tech. rep., AWA, U. S. Air Force (Headquarters, AWS, Scott AFB, IL 62225), 102 pp.
- Moncrieff, M. and M. Miller, 1976: The dynamics and simulation of tropical cumulonimbus and squall lines. *Q. J. Roy. Meteorol. Soc.*, **102**, 373–394.
- Morris, R. M., 1986: The spanish plume - testing the forecaster's nerve. *Meteorol. Mag.*, **115**, 349–357.
- Oppenheim, A. and R. Schafer, 1989: *Discrete-Time Signal Processing*. Prentice-Hall, 447 pp.
- Pruppacher, H. R. and J. D. Klett, 1997: *Microphysics of Clouds and Precipitation*. Kluwer Academic Publisher, Dordrecht.
- Puskeiler, M., 2009: Analyse der Hagelgefährdung durch Kombination von Radardaten und Schadendaten für Südwestdeutschland. Diploma thesis, Universität Karlsruhe.

- Roeckner, E., et al., 2003: The atmospheric general circulation model ECHAM 5. Part I: Model description. *MPI-Report*, **349**.
- Sauvageot, H., 1992: *Radar Meteorology*. Artech House, Boston.
- Schönwiese, C.-D., 2000: *Praktische Statistik für Meteorologen und Geowissenschaftler*. Gebrüder Borntraeger, Stuttgart, 240-265 pp.
- Scinocca, J., N. McFarlane, M. Lazare, J. Li, and D. Plimmer, 2008: Technical Note: The CCCma third generation AGCM and its extension into the middle atmosphere. *Atmos. Chem. Phys.*, **8**, 7055–7074.
- Sen, P., 1968: Estimates of the regression coefficient based on Kendall's tau. *J. Amer. Stat. Assoc.*, **63**, 1379–1389.
- Showalter, A., 1953: A stability index for thunderstorm forecasting. *Bull. Am. Meteorol. Soc.*, **34**, 250–252.
- Simmons, A., S. Uppala, D. Dee, and S. Kobayashi, 2007: ERA-Interim: New ECMWF reanalysis products from 1989 onwards. *ECMWF Newsletter*, **110**, 25–35.
- Strangeways, I., 2007: *Precipitation: Theory, Measurements and Distribution*. Cambridge University Press, Cambridge.
- Stucki, M. and T. Egli, 2007: Elementarschutzregister Hagel, Untersuchungen zur Hagelgefahr und zum Widerstand der Gebäudehülle. Präventionsstiftung der kantonalen Gebäudeversicherungen, Bern.
- Theil, H., 1950: A rank-invariant method of linear and polynomial regression analysis I-III. *Nederlands Akad. Wetensch. Proc.*, **53**, 386–392; 521–525; 1397–1412.
- Uppala, S. M. and . coauthors, 2005: The ERA-40 re-analysis. *Q. J. R. Meteorol. Soc.*, **131**, 2961–3012.
- Van Delden, A., 2001: The synoptic setting of thunderstorms in Western Europe. *Atmos. Res.*, **56**, 89–110.
- Vitolo, R. and T. Economou, 2011: Report on the statistical modelling of hail days. University of Exeter.
- Von Storch, H. and F. W. Zwiers, 2003: *Statistical Analysis in Climate Research*. Cambridge University Press.
- Von Storch, V. and A. Navarra, 1995: *Analysis of climate variability: Applications of statistical techniques. Misuses of statistical analysis in climate research*. Springer-Verlag, Berlin.
- Weber, O., 2006: Analyse von Hagelereignissen in Baden-Württemberg anhand von Daten der SV-Sparkassen-Versicherung. Seminar thesis, University of Karlsruhe (TH).

- 
- Weisman, M. and J. B. Klemp, 1986: *Mesoscale Meteorology and forecasting*. Am. Meteorol. Soc, Boston.
- Wilks, D. S., 1995: *Statistical Methods in the Atmospheric Sciences*. Academic Press, San Diego.
- Wilks, S., 1938: The large-sample distribution of the likelihood ratio for testing composite hypothesis. *Ann. Math. Stat.*, **9**, 554–560.
- Xu, K. and D. Randall, 2001: Updraft and downdraft statistics of simulated tropical and midlatitude cumulus convection. *J. Atmos. Sci.*, **58**, 1673–1693.
- Yue, S., P. Pilon, B. Phinney, and G. Cavadias, 2002: The influence of autocorrelation on the ability to detect trend in hydrological series. *Hydrol. Process.*, **16**, 1807–1829.



# Acknowledgments

Finally, I want to thank everybody who made my studies and this thesis possible.

In particular I want to thank Prof. Dr. Christoph Kottmeier and Dr. Michael Kunz for giving me the opportunity to work on this interesting topic. I also want to thank Prof. Dr. Klaus Beheng for agreeing to review my thesis, for proofreading it in advance and his helpful comments.

I am very grateful to Dr. Michael Kunz for his always friendly supervision, ideas, comments, permanent motivation and his patience, especially with proofreading my thesis. I also want to thank him for contacts within the Willis Reseach Network and for making an exchange with the Exeter Climate Systems research group possible.

Many thanks go to Dr. Renato Vitolo for a great time in Exeter, his excellent ideas and hospitality. I would also like to thank Dr. Theodoros Economou for computing the statistical model and his patience for answering (many) statistical questions. Thanks to the whole XCS research group that made my short visit very fruitful. Furthermore, I would like to thank Dr. Alef Sterk for immediately making me feel at home in Exeter. I also owe gratitude to the DAAD for supporting this trip financially.

Thanks to Dr. Ulrike Gelhardt, Jürgen Lang and Ulf Riediger for providing information on the oWLK and sharing their experience of its application to climate models.

Thanks go to Susanna Mohr for her friendly provision of software and climate model data, Dr. Hans Schipper for his help with GMT, Dr. Peter Berg for his help with problems regarding the climate models and all the other members of the working group "Atmosphärische Risiken" that gave helpful tips and helped to create a pleasant working atmosphere. Furthermore, I thank Mr. Brückel for his always immediate help with computer problems and Ms. Birnmeier and Ms. Schönbein for their friendly administrative assistance. Thanks also go to the other colleagues at the IMK and my co-students that helped to delight everyday life.

I am grateful to all those people who read my thesis in advance. Thanks Jeremy, Joe and Matt for corrections of my language mistakes and suggestions. Furthermore, I would like to thank Christian B., Christian E. and Julia for their immediate help, especially at the end of my thesis. I know I can always count on you.

Last but not least I would like to thank my parents, who always supported me financially and mentally throughout my whole studies. Thanks for always being there when needed and your repeated encouragement. For latter reasons, I also want to thank my sister Julia, Plamen, Eva, the rest of my family and all my great friends.

Finally, I want to deeply apologize for everybody who was missed here.



# Erklärung

Hiermit erkläre ich, dass ich die vorliegende Arbeit selbst verfasst und nur die angegebenen Hilfsmittel verwendet habe.

Ich bin damit einverstanden, dass diese Arbeit in Bibliotheken eingestellt wird und vervielfältigt werden darf.

Karlsruhe, den 15. März 2011

Marie-Luise Kapsch